138 Image Processing and Interpretation
Sunday, May 07, 2017 3:15 PM–5:00 PM
Exhibit/Poster Hall Poster Session
Program #/Board # Range: 637–691/B0384–B0438
Organizing Section: Multidisciplinary Ophthalmic Imaging Group

Program Number: 637 **Poster Board Number:** B0384
Presentation Time: 3:15 PM–5:00 PM
Reliability Of Split-Spectrum Amplitude-Decorrelation Angiography OCTA Capillary Perfusion Density Analysis
Jason Young, Fabiana Q. Silva, Rishi P. Singh. Ophthalmology, Cleveland Clinic, Cleveland, OH.
Purpose: Optical coherence tomography angiography (OCTA) allows for the quantification of retinal capillary density. However, there has been limited evaluation of the reliability of density mapping in various retinal conditions. The aim of this study is to evaluate the factors that affect the intra-individual reliability of retinal thickness and vascular density measurements using OCTA.
Methods: A retrospective analysis was conducted to determine the intra-individual reliability of retinal thickness and vascular density measurements of split-spectrum amplitude-decorrelation angiography (SSADA) OCTA. OCTA (Avanti RTVue XR; Optovue, Fremont, CA) images were acquired by a single operator at a tertiary care center. Patients were selected based on retinal disease and three images were acquired, each being spaced 5 minutes apart. The capillary perfusion density (CPD) analysis provided CPD values and retinal thickness measurements of the superficial and deep retinal capillaries and values were recorded. Retinal thickness and CPD measurements of the perfusion density analysis were compared between time points and differences were calculated.
Results: Thirty-four eyes of individual patients were imaged. Eighteen patients were female and the mean age of the whole cohort was 71 years (SD:±9.7 years). Approximately 73.5% of eyes (n=25) were phakic. Non-proliferative diabetic retinopathy (NPDR), proliferative diabetic retinopathy (PDR), non-exudative age-related macular degeneration (AMD) and central retinal vein occlusion (CRVO) were present in 14.7%, 11.8%, 11.8% and 11.8% of patients, respectively and 14.7% of eyes had no retinal pathology. The average signal strength across all eyes was 56.6 ± 9.5. The average percent deviation in parafoveal thickness for the various retinal diseases across all time points was 1.16% in BRVO, 1.80% in CRVO, 0.11% in dry AMD, 0.40% in PDR, and 1.59% in patients without retinopathy. The average percent deviation in foveal capillary perfusion density was 5.87% in BRVO, 7.36% in CRVO, 1.61% in dry AMD, 4.02% in PDR, and 3.12% in patients without retinal disease.
Conclusions: For the majority of retinal diseases, the SSADA OCTA analysis is a reliable tool for evaluation of retinal perfusion. Deviation of results from the density analysis are most substantial in patients with vein occlusions and should be kept in mind when analyzing these images in prospective studies.
Commercial Relationships: Jason Young, None; **Fabiana Q. Silva**, None; **Rishi P. Singh**, Alcon (R), Optos (C), Genentech (R), Apellis (R), Genentech (C), Regeneron (C), Zeiss (C), Regeneron (R), Shire (C)

Program Number: 638 **Poster Board Number:** B0385
Presentation Time: 3:15 PM–5:00 PM
Hybrid OCT-OCTA Vessel Visualization for Projection-Free Display of the Intermediate and Deep Retinal Plexuses
Stefan B. Ploner[1], Eric M. Moult[2], Julia Schottenhamml[2, 1], Lennart Husvogt[1], Chen D. Lu[2], Carl B. Rebhun[3], A. Yasin Alibhai[3], Jay S. Duker[3], Nadia Waheed[3], Andreas K. Maier[1], James G. Fujimoto[2]. [1]Pattern Recognition Lab, Friedrich-Alexander-University Erlangen-Nürnberg, Erlangen, Germany; [2]Department of Electrical Engineering and Computer Science, and Research Laboratory of Electronics, Massachusetts Institute of Technology, Cambridge, MA; [3]New England Eye Center, Tufts Medical Center, Boston, MA.
Purpose: In optical coherence tomography angiography (OCTA), projection artifacts (also shadowing artifacts or decorrelation tails) cause superficial retinal vasculature to appear in the segmented OCTA images of the intermediate and deep retinal plexuses. The projections of these larger superficial vessels obfuscate the unique vascular patterning of the deeper layers. Several algorithms have been proposed to remove these shadows. However, by removing the projected vessels these approaches also decrease the contrast of, or fully eliminate, the underlying vasculature, thereby introducing discontinuities. Thus, in effect, one artifact is replaced with another. The purpose of this study is to develop a projection artifact removal scheme that overcomes this limitation and fully preserves the intermediate/deep retinal vasculature.
Methods: Amplitude decorrelation based OCTA data was collected using a 1050nm swept source OCT system. A hybrid OCT-OCTA vessel visualization scheme (described in Figure 1) was developed. The key advantage of our proposed scheme is that the OCT signal is used to adaptively remove the OCTA signal only in the intercapillary regions.
Results: The hybrid OCT-OCTA approach reduces projection artifacts to a negligible level in the intermediate and deep plexuses without introducing vessel discontinuity artifacts (Figure 2).
Conclusions: Hybrid OCT-OCTA vessel visualization is a promising approach to visualize the unique patterning of the intermediate and deep plexuses, and is likely to be particularly important in diseases such as diabetic retinopathy where it is desirable to separately analyze the retinal plexuses.

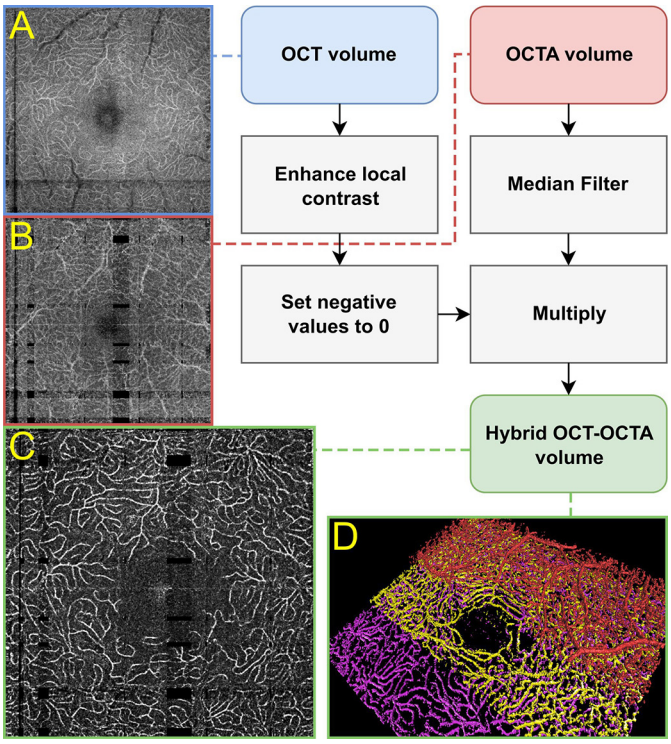

Flow chart of the hybrid OCT-OCTA vessel visualization algorithm alongside representative en face projections of the deep retinal plexus using (A) OCT, (B) OCTA, and (C) hybrid OCT-OCTA volumes. (D) Volumetric rendering showing the superficial/intermediate/deep plexus in red/yellow/purple color.

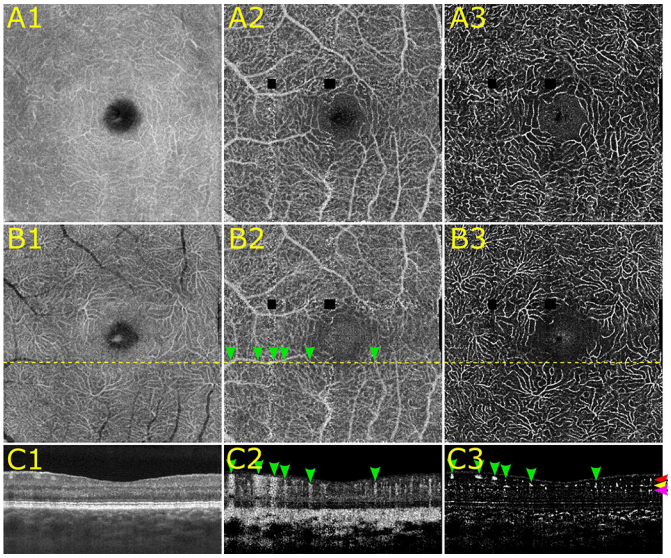

1st column: OCT; 2nd column: OCTA; 3rd column: hybrid OCT-OCTA. (A) En face projections over the intermediate retinal plexus. (B) En face projections over the deep retinal plexus. (C) B-scans extracted at the dashed lines in B. Note the decorrelation tails in C2 (green arrows). In C3, decorrelation tails are absent, and vessels perpendicular to the B-scan appear as circles. Note also that the different vascular plexuses can easily be distinguished in B-scan C3 (right arrows).

Commercial Relationships: Stefan B. Ploner; **Eric M. Moult**, None; **Julia Schottenhamml**, None; **Lennart Husvogt**, None; **Chen D. Lu**, None; **Carl B. Rebhun**, None; **A. Yasin Alibhai**, None; **Jay S. Duker**, Optovue, Inc. (F), Topcon Medical Systems, Inc. (F), Carl Zeiss Meditec, Inc. (F), Topcon Medical Systems, Inc. (C), Optovue, Inc. (C), Carl Zeiss Meditec, Inc. (C); **Nadia Waheed**, Carl Zeiss Meditec, Inc. (R), MVRF (F), Genentech (C), Janssen (C), Ocudyne (C), Optovue, Inc. (R), Regeneron (C), Nidek (R); **Andreas K. Maier**, None; **James G. Fujimoto**, Optovue, Inc. (I), Optovue, Inc. (P), Carl Zeiss Meditec, Inc. (P)

Support: 5-R01-EY011289-28, FA9550-15-1-0473, FA9550-10-1-0551

Program Number: 639 **Poster Board Number:** B0386
Presentation Time: 3:15 PM–5:00 PM

Relationship Between Computer-based Hypertensive Retinopathy Grading and Cardiovascular Disease Risk

Vinayak S. Joshi[1], Carla Agurto[1], E Simon Barriga[1], Sheila C. Nemeth[1], Ellaheh Ebrahim[2], Peter Soliz[1]. [1]Medical Image analysis, VisionQuest Biomedical LLC, Albuquerque, NM; [2]Community healthcare center, Wichita Falls, TX.

Purpose: To investigate the potential of using computer-based hypertensive retinopathy (HR) detection software as a tool in estimating the 10-year cardiovascular disease (CVD) risk.

Methods: A clinical study was performed to acquire retinal fundus images and clinical data from patients with chronic hypertension and potential risk of CVD, as determined by a primary care physician (PCP). The PCP's determination was based on evaluation of risk factors such as obesity, smoking, blood pressure, body-to-mass index, cholesterol levels, lipid panel, family history of CVD, and pre-existing conditions. The clinical data acquired from patients included demographics, health record, disease history, and metabolic panel tests based on blood and urine samples. The clinical data was utilized to calculate the 10-year risk of CVD using the ASCVD clinical calculator, developed by the American College of Cardiology and American Heart Association.

The automated HR detection software, "CARV" (Comprehensive Assessment of Retinal Vessels), was developed for the identification of HR abnormalities such as artery-venous ratio, vessel tortuosity, copper/silver wiring, and retinal emboli. A partial least square classifier combined the individual algorithms to quantify the likelihood of presence of HR. The software performance was tested against the ground truth provided by a retinal grader for presence or absence of HR, to calculate sensitivity and specificity. Pearson's correlation was calculated between the 10-year CVD risk estimation and HR likelihood results provided by the software and the retinal grader.

Results: A dataset of 25 patients was utilized, with N=10 patients with HR and N=15 controls with no retinopathy. The CARV software achieved sensitivity of 90% and specificity of 73% in detecting HR against the ground truth provided by the retinal grader. The Pearson's correlation coefficient between the 10-year ASCVD risk estimation and the likelihood of HR as determined by the software, was 0.64. The correlation between the retinal grader and the 10-year ASCVD risk estimation was 0.62.

Conclusions: Our results show significant correlation between detection of HR and estimated risk of CVD, demonstrating the potential of HR detection system, as a tool for estimating the associated risk of CVD, which may aid in improving the screening of HR as well as predicting the future complications occurring due to CVD.

Commercial Relationships: Vinayak S. Joshi; **Carla Agurto**, None; **E Simon Barriga**, VisionQuest Biomedical LLC. (I); **Sheila C. Nemeth**, VisionQuest Biomedical LLC. (E);

Ellaheh Ebrahim, Community Healthcare Center (E); **Peter Soliz**, VisionQuest Biomedical LLC. (I)
Support: NEI grant 2R44EY024169-02

Program Number: 640 **Poster Board Number:** B0387
Presentation Time: 3:15 PM–5:00 PM
Automated Montage OCT Angiography for Wide-Field Visualization of Retinal Pathologies
Roger Goldberg[1], Michael Chen[2], Conor Leahy[2], Kevin Meng[2], Mary K. Durbin[2]. [1]Bay Area Retina Associates, Walnut Creek, CA; [2]R&D, Carl Zeiss Meditec, Dublin, CA.
Purpose: To obtain automated montages of optical coherence tomography (OCT) angiography en-face images, thereby providing a wider and more complete view of the retina vasculature and perfusion status across a range of retinal diseases.
Methods: 10 subjects with retinal disease were imaged using a CIRRUS™ HD-OCT 5000 AngioPlex device (ZEISS, Dublin, CA). Multiple OCT angiography scans were acquired at differing fixation points for each subject. By controlling the position of the device's internal fixation target, the overlap between adjacent scans was maintained at approximately 30-40%. Montages were then generated using a custom automated image-stitching algorithm, which transforms and blends the images together into a single mosaic.
Results: OCT angiography montages were created for patients with diabetic retinopathy, branch retinal vein occlusion (BRVO), and age-related macular degeneration. Representative images show OCT angiography montages (superficial layer) for two patients with diabetic retinopathy. Montage images were able to consistently capture the posterior 55°.
Conclusions: Creating montage images of OCT angiography scans enables wide-field visualization of the retina. This can be done in a semi-automated fashion to capture the majority of the posterior pole. This high-quality, non-invasive imaging capability may be useful to clinicians for both the diagnosis and treatment over time of a range of retinal disease.

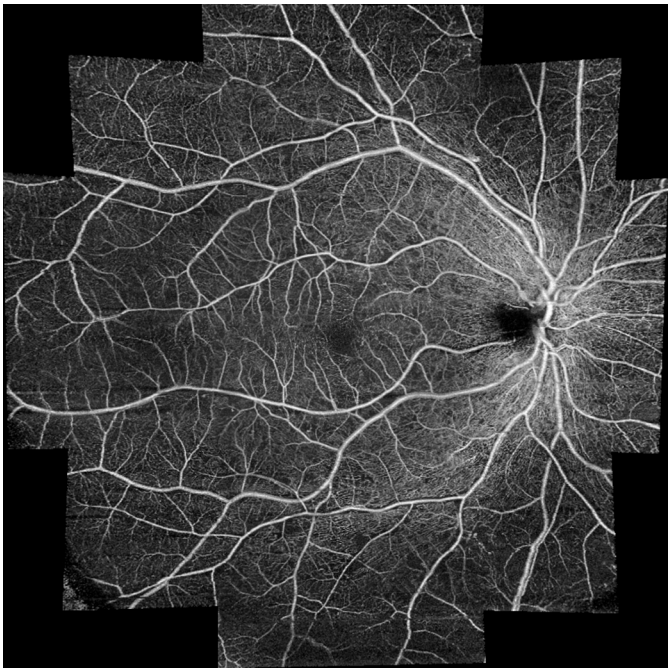

Montage OCT angiography show the vascular flow over the posterior 55 degrees in a patient with diabetic retinopathy.

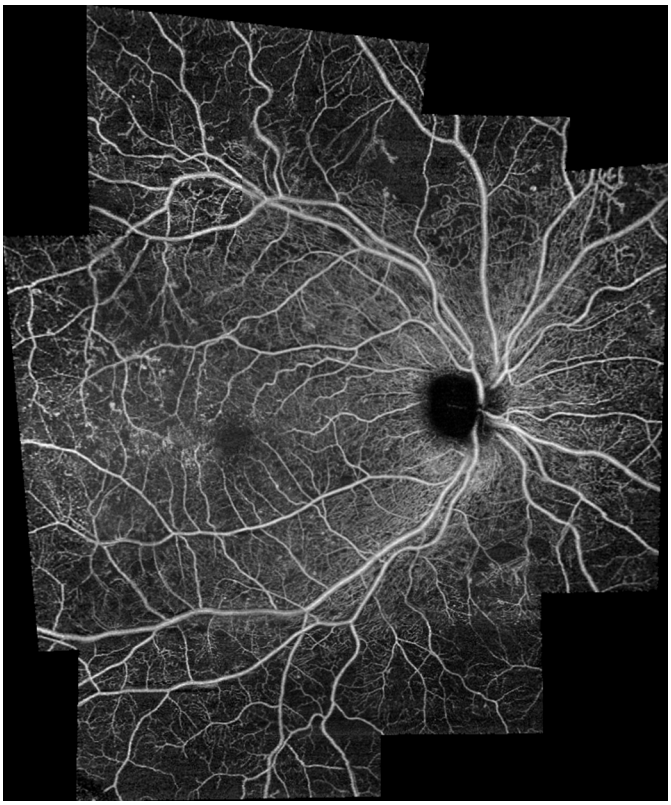

Mongtage OCT angiography shows temporal macular microaneurysms and peripheral retinal non-perfusion with capillary dropout in a patient with diabetic retinopathy.
Commercial Relationships: Roger Goldberg, Zeiss (C), Zeiss (F); **Michael Chen**, Zeiss (E); **Conor Leahy**, Zeiss (E); **Kevin Meng**, Zeiss (E); **Mary K. Durbin**, Zeiss (E)

Program Number: 641 **Poster Board Number:** B0388
Presentation Time: 3:15 PM–5:00 PM
Registration of 3D Retinal OCT Images
Lingjiao Pan[1, 2], Xinjian Chen[1]. [1]School of Electronics and Information Engineering, Soochow University, Suzhou, China; [2]School of Electricity and Information Engineering, Jiangsu University of Technology, Changzhou, China.
Purpose: Image registration has not been well-developed on 3D OCT images. The successful development of registration techniques for 3D retina OCT can greatly help us to understand the relationship between retina.
Methods: The proposed method consists of preprocessing, feature extraction and two stage registration. In preprocessing, the OCT images are segmented by ILM, NFL-GCL boundary, IPL-INL boundary, INL-OPL boundary, OPL-ONL boundary, ISL-CL boundary and BRM using multilayer graph-search approach. Then, the intensity values of layers between ISL-CL boundary and BRM are averaged to obtain the projection image. In feature extraction, edge feature is extracted from the segmented images. Edge feature takes one of eight discrete values which represents eight edge types including non-edge and seven segmented boundaries. Vessel map is extracted from the projection image using vessel enhancement filter and a mathematical morphology method. The proposed registration method is a two stage registration. The first stage is to find the displacement in x-y plane. The vessel map of subject OCT is registered to the vessel map of template OCT using SURF

algorithm. The second stage is to perform non-rigid registration along z direction. It is restricted to corresponding pairs of A-scans. The hierarchical deformation mechanism of HAMMER which is successful used in MRI of brain image is adopted for the registration. The distinct anatomy such as the edge voxels on ILM and BRM are first selected to initial the deformation. Then, other edge voxels are hierarchical added to drive the deformation.

Results: 9 retinal OCT scans acquired using Topcon DRI OCT-1 scanner with image dimension of 512x992x256 and resolution of 6mmx6mmx2.5mm were included in this study. The absolute difference map between template and subject show that the registration greatly reduced their differences. The average absolute boundary surface error compare with manual segmentation is reduced from 39.9um to 7.8 um after registration.

Conclusions: We have presented a novel image registration approach for 3D retinal OCT image. Edge, vessel and intensity features are extracted and a two stage registration mechanism was adopt to deform the OCT image. Simulation results show the accuracy of this method.

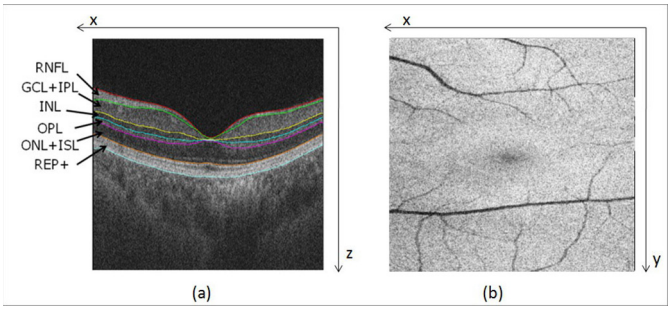

Fig.1 Illustration of the segmentation image (a) and projection image (b).

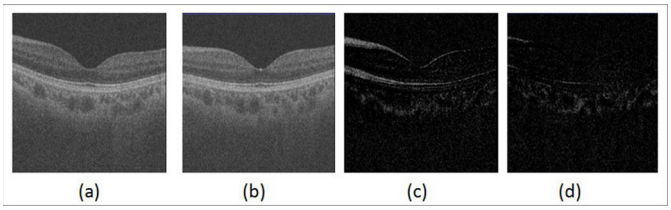

Fig.2 (a) Template, (b) Subject,(c) Absolute difference image before registration, (d) Absolute difference image after registration.

Commercial Relationships: Lingjiao Pan, None; **Xinjian Chen**, None

Support: National Basic Research Program of China (973 Program) under Grant 2014CB748600;(NSFC) under Grant 81371629;graduate student innovation Program under Grant KYZZ16_0084

Program Number: 642 **Poster Board Number:** B0389
Presentation Time: 3:15 PM–5:00 PM

Algorithm for bulk motion removal in optical coherence tomography angiography

Acner Camino, Yali Jia, Gangjun Liu, JIE WANG, David Huang. OHSU, Portland, OR.

Purpose: To remove decorrelation signal due to bulk motion (BM) while preserving true flow signal in optical coherence tomography angiography (OCTA).

Methods: Four volumetric OCTA scans of the macular region were acquired from a healthy human subject using a wide-field 200 kHz swept-source OCT system. The scan pattern consisted of 800x399 transverse pixels covering an 8x6mm^2 area. Two B-scans at each raster position were used to compute flow signal using the split-spectrum amplitude-decorrelation angiography algorithm. Each B-frame was divided into 5 segments for regression analysis. Within each segment, the first 15 percentile of A-lines (representing bulk tissue) with lowest flow signal were used for regression analysis of decorrelation (D) vs. logarithm of reflectance. The regression analysis provided a reflectance adjusted threshold for distinguishing flow from BM voxels, as well as the estimated BM velocity. The BM velocity was subtracted from the vascular voxels using a nonlinear model that related D and velocity in laboratory blood flow phantoms. The effectiveness of the algorithm was compared with an earlier method in which the median decorrelation value in each B-frame was subtracted from all voxels in the B-frame.

Results: The step of filtering out BM voxels improved the contrast between capillaries and background and the step of subtracting BM velocity from vascular voxels further removed line artifacts (Fig.1). Compared to the median subtraction algorithm (Table 1), the regression-based BM subtraction algorithm removed a larger percentage of D noise from the foveal avascular zone ($p<0.01$), achieved a greater improvement in vessel density measurement repeatability, and better signal to noise ratio for flow detection ($p<0.01$). Two methods preserved vascular continuity ($p>0.05$).

Conclusions: The regression-based BM subtraction algorithm appeared to more completely remove BM noise from OCTA compared to the median subtraction algorithm. This could improve image interpretation by reducing line artifacts and make quantification of vessel density more accurate.

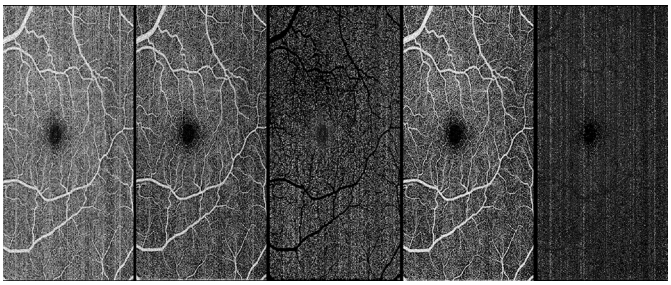

Processing to remove bulk motion signal from a macular OCTA scan. (A) Original *en face* retinal angiogram. (B) After removal of decorrelation signal from bulk motion voxels using a reflectance-adjusted threshold. (C) Difference between images A and B. (D) After subtraction of bulk motion velocity from the vascular voxels. (E) Difference between images B and D

Bulk motion algorithm	% Reduction in FAZ flow signal	Vessel density repeatability	Vascular connectivity	Flow SNR
Original (no subtraction)	N/A	1.9%	87.5% ±0.6%	13.2 ±0.8
Median subtraction	83.7% ±1.7%	1.1%	88.3% ±0.5%	23.3 ±1.8
Regression-based BM subtraction	91.9% ±0.8%	0.9%	87.3% ±0.5%	28.5 ±1.9

The values listed in the cells are mean ± standard error
Flow signal in the foveal avascular zone (FAZ) represented a pure measure of bulk motion noise.
Vessel density was the percentage of area occupied by vascular pixels within the inner retinal slab and its repeatability was calculated by the coefficient of variation.
Vascular connectivity was defined in a skeletonized version of the en face angiogram as the percentage of flow pixels connected in groups larger than five.
Flow signal-to-noise ratio (SNR) was calculated by the ratio of decorrelation (flow) signal in the parafoveal annulus (outer diameter=2.5mm, inner diameter=0.6mm) divided by decorrelation noise the FAZ.

Commercial Relationships: Acner Camino, None; **Yali Jia**, Optovue, Inc (F), Optovue, Inc. (P); **Gangjun Liu**, None; **JIE WANG**, None; **David Huang**, Optovue, Inc (I), Optovue, Inc (F), Optovue, Inc (P)

Support: National Institutes of Health (NIH) (DP3 DK104397, R01 EY024544, R01 EY023285, P30 EY010572). Unrestricted departmental funding from Research to Prevent Blindness (New York, NY)

Program Number: 643 **Poster Board Number:** B0390
Presentation Time: 3:15 PM–5:00 PM
A Fast Method to Reduce Decorrelation Tail Artifacts in OCT Angiography

Homayoun Bagherinia, Robert W. Knighton, Luis De Sisternes, Michael H. Chen, Mary K. Durbin. R&D, Carl Zeiss Meditec, Inc., Dublin, CA.

Purpose: Optical coherence tomography angiography (OCT-A) is prone to decorrelation tails, apparent flow in retinal tissue due to the blood flow within overlying vessels. Such artifacts can interfere with the interpretation of angiographic results. We present a fast practical approach for reducing these artifacts using slab images generated from two or more retinal layers.

Methods: A slab image can be generated by linearly or nonlinearly projecting the OCT-A cube data (generated using Optical Micro Angiography (OMAG^c) algorithms) within one or more layers. The artifact reduction method assumes that the observed lower slab image (I) is generated by additive mix of a signal from an upper slab (U) and a lower slab without artifacts ($\hat{I}$). The mixing problem can be formulated as $\hat{I}=I-wU$, where $w\in[0.1]$ is the fraction of U added to $\hat{I}$ to result in I. If the upper slab and the unknown lower slab with no artifacts do not have similar vessel patterns, w can be solved by minimizing the square of the normalized cross-correlation between U and $\hat{I}$ as $min_w\gamma^2(U,I-wU)$. The explicit solution is $w=Cov(U,I)/Var(U)$, which is rapidly computed.

Results: We have tested our method on 32 scans using CIRRUS HD-OCT 5000 with AngioPlex™ OCT Angiography (ZEISS, Dublin, CA), and 25 cases using PLEX™ Elite 9000 (ZEISS, Dublin, CA) with diseases such as Diabetic Retinopathy, wet and dry Age-related Macular Degeneration (AMD), Branch Retinal Vein Occlusion, Sickle Cell Disease, Central Retinal Artery Occlusion, Macular telangiectasia, and normal. Figure 1 and 2 show examples of decorrelation artifacts reduction by our method for two cases of Neovascular AMD.

Conclusions: We present a practical and fast method to reduce the decorrelation tail artifacts in OCT-A images. This artifact reduction technique also can be used to correct a whole OCT-A cube with a sliding slab that is segmentation-independent. Our approach is specifically useful for visualization and interpretation of a variety of retinal vascular diseases.

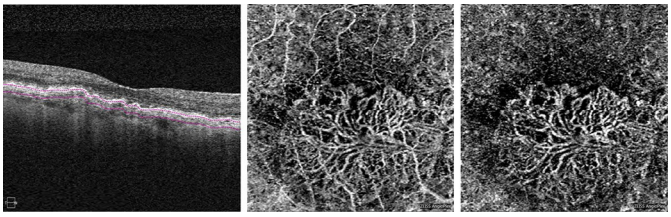

Figure 1: Neovascular AMD type 1 case from AngioPlex OCT: an intensity B-scan with two layer boundaries, corresponding slab with decorrelation tail artifacts, and with reduced artifacts. Note that choriocapillaris is not removed.

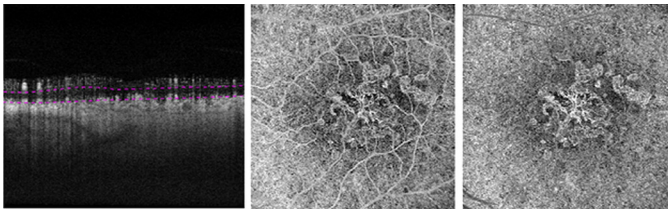

Figure 2: Neovascular AMD from PLEX Elite 9000: a flow B-scan with two layer boundaries, corresponding slab with decorrelation tail artifacts, and with reduced artifacts. Note that choriocapillaris is not removed.

Commercial Relationships: Homayoun Bagherinia, Carl Zeiss Meditec, Inc. (E); **Robert W. Knighton**, Carl Zeiss Meditec, Inc. (C); **Luis De Sisternes**, Carl Zeiss Meditec, Inc. (E); **Michael H. Chen**, Carl Zeiss Meditec, Inc. (C); **Mary K. Durbin**, Carl Zeiss Meditec, Inc. (E)

Program Number: 644 **Poster Board Number:** B0391
Presentation Time: 3:15 PM–5:00 PM
Layer-Specific Vascular Analysis of OCT Angiography in Diabetic Macular Edema

Kyungmoo Lee[1, 2], Ian C. Han[3, 4], Douglas B. Critser[3], Andreas Wahle[1, 2], Milan Sonka[1, 2], Michael D. Abramoff[3, 5]. [1]Electrical and Computer Engineering, University of Iowa, Iowa City, IA; [2]Iowa Institute for Biomedical Imaging, University of Iowa, Iowa City, IA; [3]Ophthalmology and Visual Sciences, University of Iowa, Iowa City, IA; [4]Stephen A. Wynn Institute for Vision Research, University of Iowa, Iowa City, IA; [5]Iowa City VA Health Care System, Iowa City, IA.

Purpose: OCT angiography (OCTA) is a new non-invasive imaging technique used for diagnosing and monitoring retinal vascular diseases. Quantification of layer specific capillary metrics is of high value to a better understanding and management of diabetic macular edema (DME). However, layer segmentation algorithms typically fail in DME with substantial retinal thickening, intercellular fluid and cysts. The aim of this study is to evaluate the Iowa Reference Algorithms and layer specific OCTA.

Methods: Eleven OCT and OCTA volume pairs ($350 \times 1024 \times 350$ voxels, $6.02 \times 2.00 \times 6.02$ mm^3) were obtained from 11 eyes (6 OD, 5 OS) of 11 patients (54.5 ± 11.1 years) with DME using a Cirrus 5000 HD-OCT Angioplx (Carl Zeiss Meditec Inc., Dublin, CA). Ten retinal layers were automatically segmented from the OCT volume using the Iowa Reference Algorithms (http://www.iibi.uiowa.edu/content/shared-software-download, Figs. 1ab) and defined the retinal layers in the OCTA volume (Figs. 1cd). For each layer, an OCTA density map was created by averaging voxel intensities in the depth direction to identify vasculature (Figs. 1eg). A capillary density map was generated by segmenting the smallest vessel and determining density (Figs. 1fh).

Results: Fig. 1 shows a typical example for our layer-specific vascular analysis of OCT angiography. The segmented inner retinal layers are located above the fluid-filled regions (Fig. 1b). In 10 / 11, these maps were obtained successfully.

Conclusions: Quantification and analysis of vasculature for layer specific OCTA volumes are possible using the proposed method, in most cases, and have the potential to increase our understanding and management of diabetic macular edema, an important cause of blindness.

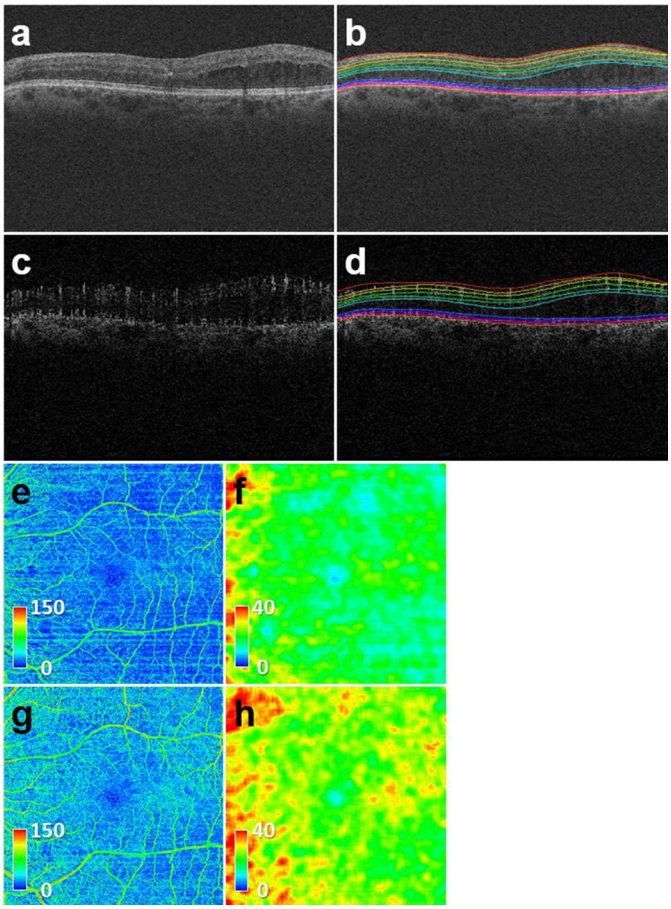

Figure 1. (a) B-scan of the OCT volume with DME. (b) Panel (a) layer segmentation. (c) B-scan of the OCTA volume. (d) Panel (c) with layer segmentation. (e, f) OCTA density map and capillary density map of retinal nerve fiber layer plus ganglion cell layer (RNFL+GCL). (g, h) OCTA density map and capillary density map of inner plexiform layer plus inner nuclear layer (IPL+INL).

Commercial Relationships: Kyungmoo Lee, None; **Ian C. Han**, None; **Douglas B. Critser**, IDx LLC (I), IDx LLC (C); **Andreas Wahle**, None; **Milan Sonka**, University of Iowa (P); **Michael D. Abramoff**, University of Iowa (P), IDx LLC (I), IDx LLC (C)

Support: NIH Grants R01 EY019112, R01 EY018853; the Department of Veterans Affairs; Alimera Inc, The Robert C. Watzke MD Professorship for Retina Research.

Program Number: 645 **Poster Board Number:** B0392
Presentation Time: 3:15 PM–5:00 PM

OCT-OCTA Segmentation: a Novel Framework and an Application to Segment Bruch's Membrane in the Presence of Drusen

Julia Schottenhamml[1, 2], Eric M. Moult[1], Eduardo A. Novais[4, 3], Martin F. Kraus[2], ByungKun Lee[1], WooJhon Choi[1], Stefan B. Ploner[2], Lennart Husvogt[2], Chen D. Lu[1], Patrick Yiu[1], Philip J. Rosenfeld[5], Jay S. Duker[3], Andreas K. Maier[2], Nadia Waheed[3], James G. Fujimoto[1]. [1]Research Laboratory of Electronics, Massachusetts Institute of Technology, Cambridge, MA; [2]Pattern Recognition Lab, Friedrich-Alexander-University Erlangen-Nuremberg, Erlangen, Germany; [3]New England Eye Center, Tufts Medical Center, Boston, MA; [4]Department of Ophthalmology, Federal University of Sao Paulo, Sao Paulo, Brazil; [5]Department of Ophthalmology, University of Miami Miller School of Medicine, Miami, FL.

Purpose: We present a novel framework for segmenting optical coherence tomography (OCT) and OCT angiography (OCTA) that jointly uses structural and angiographic information. We term this new paradigm "OCT-OCTA segmentation," and demonstrate its utility by segmenting Bruch's membrane (BM) in the presence of drusen.

Methods: We developed an automatic OCT-OCTA graph-cut algorithm for BM segmentation. Our algorithm's performance was quantitatively validated by comparing it with manual segmentation in 7 eyes (6 patients; 73.8±5.7 y/o) with drusen. The algorithm was also qualitatively assessed in healthy eyes (n=13), eyes with diabetic retinopathy (n=21), early/intermediate age-related macular degeneration (AMD) (n=14), exudative AMD (n=5), geographic atrophy (GA) (n=6), and polypoidal choroidal vasculopathy (n=7).

Results: The absolute pixel-wise error between the manual and automatic segmentations had the following values: mean: 4.5±0.89um; 1st Quartile: 1.9±1.35um; 2nd Quartile: 3.9±1.90um; and 3rd Quartile: 6.3±2.67. This corresponds to a mean absolute error smaller than the optical axial resolution of our OCT system (~8-9um). In all other tested eyes, qualitative visual inspection showed BM contours that were deemed suitably accurate for use in forming en face OCT(A) projections. The algorithm's poorest results occurred in GA patients with large areas of atrophy.

Conclusions: By leveraging both structural and angiographic information we showed that OCT-OCTA segmentation is likely to be a widely useful framework for segmenting ocular structures.

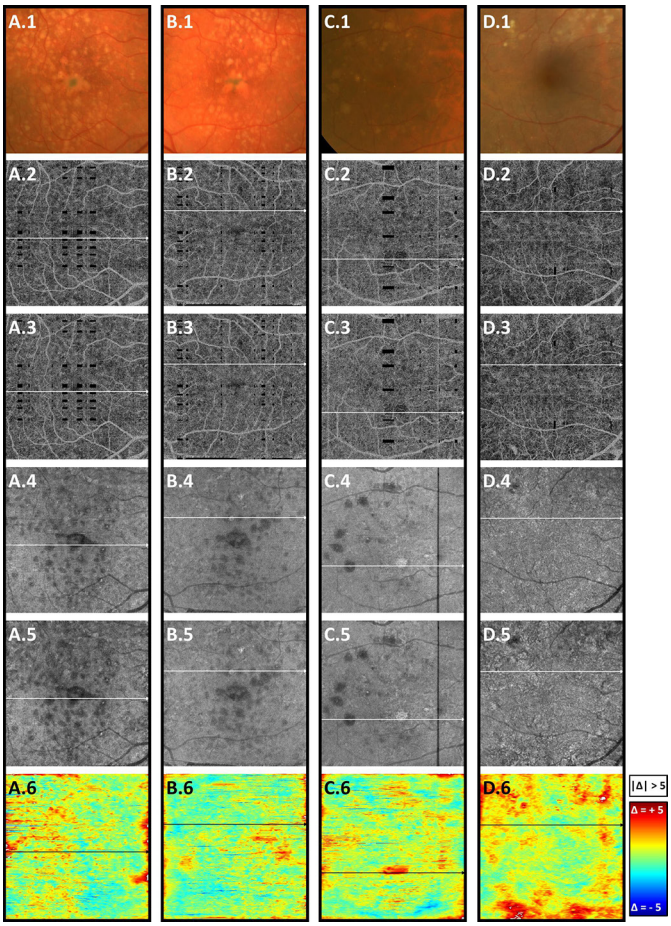

En face segmentation analysis, where each column corresponds to a different nGA/DAGA eye. 1st row: color fundus photo; 2nd, 3rd rows: en face OCTA slice taken at the manual and automatic segmentations, respectively; 4th, 5th row: en face OCT slices taken the manual and automatic segmentations, respectively. 6th row: heat map of the segmentation error (legend, bottom right; units of pixels; 1 pixel = 4.5um). All OCT(A) fields are 6x6mm.

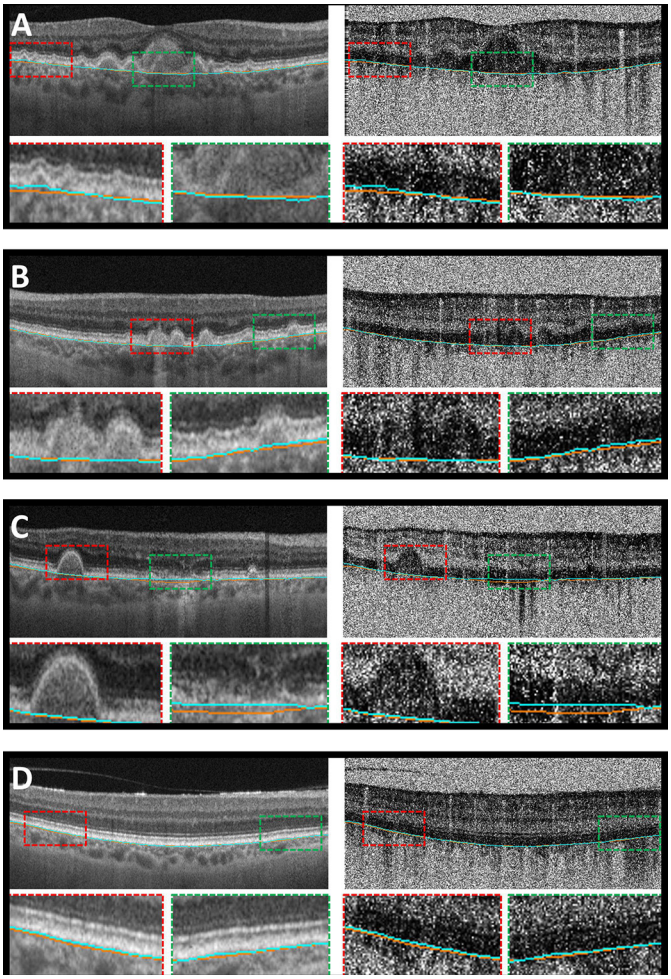

OCT(A) B-scan analysis of manual (teal) and automatic (orange) segmentations; A-D are taken from the white lines in Figure 1. Each row shows both OCT data (left) and OCTA data (right). Enlargements, indicated by red and green boxes, are also shown.

Commercial Relationships: Julia Schottenhamml; **Eric M. Moult**, None; **Eduardo A. Novais**, None; **Martin F. Kraus**, Optovue, Inc. (P), Optovue, Inc. (C); **ByungKun Lee**, None; **WooJhon Choi**, None; **Stefan B. Ploner**, None; **Lennart Husvogt**, None; **Chen D. Lu**, None; **Patrick Yiu**, None; **Philip J. Rosenfeld**, Carl Zeiss Meditec, Inc. (R), Carl Zeiss Meditec, Inc. (F), Carl Zeiss Meditec, Inc. (C); **Jay S. Duker**, Optovue, Inc. (F), Topcon Medical Systems, Inc. (F), Carl Zeiss Meditec, Inc. (F), Topcon Medical Systems, Inc. (C), Optovue, Inc. (C), Carl Zeiss Meditec, Inc. (C); **Andreas K. Maier**, None; **Nadia Waheed**, Carl Zeiss Meditec, Inc. (R), MVRF (F), Genentech (C), Janssen (C), Ocudyne (C), Optovue, Inc. (R), Regeneron (C), Nidek (R); **James G. Fujimoto**, Optovue, Inc. (I), Optovue, Inc. (P), Carl Zeiss Meditec, Inc. (P)

Support: NIH Grant 5-R01-EY011289-28, AFOSR Grant FA9550-15-1-0473, AFOSR Grant FA9550-10-1-0551

Program Number: 646 **Poster Board Number:** B0393
Presentation Time: 3:15 PM–5:00 PM

Spectral-Domain Optical Coherence Tomography Optic-Nerve-Head and Macular *En-Face* Image Registration in Cases of Papilledema

Qingyang Su[1], Jui-Kai Wang[1], Mohammad Saleh Miri[1], Victor A. Robles[1], Mona K. Garvin[2, 1]. [1]Electrical and Computer Engineering, The University of Iowa, Iowa City, IA; [2]Center for the Prevention and Treatment of Visual Loss, Iowa City VA Health System, Iowa City, IA.

Purpose: Previously, we proposed an automated method to register fundus images with its corresponding spectral-domain optical coherence tomography (SD-OCT) retinal pigment epithelium (RPE) *en-face* images in glaucoma (Miri et al. BOEx 2016). In this work, we extended the method to register two SD-OCT RPE *en-face* images from the optic-nerve-head (ONH) and macular scans in cases of papilledema. This work overcame two current challenges: 1) very limited overlap region between the two *en-face* images, and 2) frequent appearance of the massive image shadow around the ONH due to papilledema.

Methods: The proposed algorithm, first, searched for corners using the features from the accelerated segment test (FAST) approach in both ONH and macular *en-face* images. Next, the histograms of oriented gradient (HOG) for each selected corner were computed, and the proposed algorithm decided potential mapping landmarks by identifying the best matches of the feature descriptors (Fig. 1). Then, the proposed algorithm removed the incorrect landmark pairs based on the geometrical distribution of all candidates. Finally, the proposed algorithm utilized random sample consensus (RANSAC) method to estimate a similarity transformation matrix and generated the registered panorama image (Fig. 2).

Results: Fifty subjects were randomly selected from the Idiopathic Intracranial Hypertension Treatment Trial baseline dataset - where 30/20 subjects with 57/39 available OCT ONH and macular image pairs were in the training/testing set, respectively. The parameters in the proposed algorithm were empirically determined using the training set. In the testing set, two manual landmark pairs for each OCT image pair were first selected between the fixed and moving images. To evaluate the registration results, the mean distance of these landmarks shifted by the proposed algorithm in the moving image was calculated. Overall, the mean unsigned difference in the testing set was 1.97±1.00 pixels (59.1±30 μm).

Conclusions: With accurate image registration, quantitative measurements at the region between the ONH and fovea (such as retinal layer thicknesses in grids, wide-field-retina-shape measures, retinal fold quantification) are potentially clinically meaningful in papilledema.

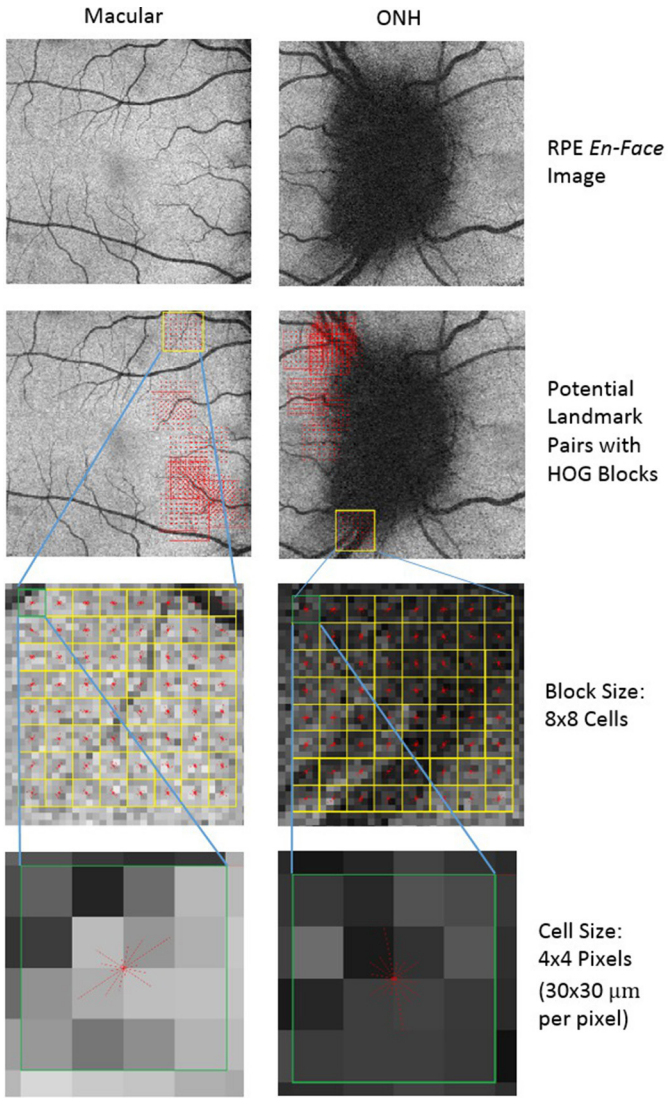

Fig. 1. Examples of HOG Descriptor Computation

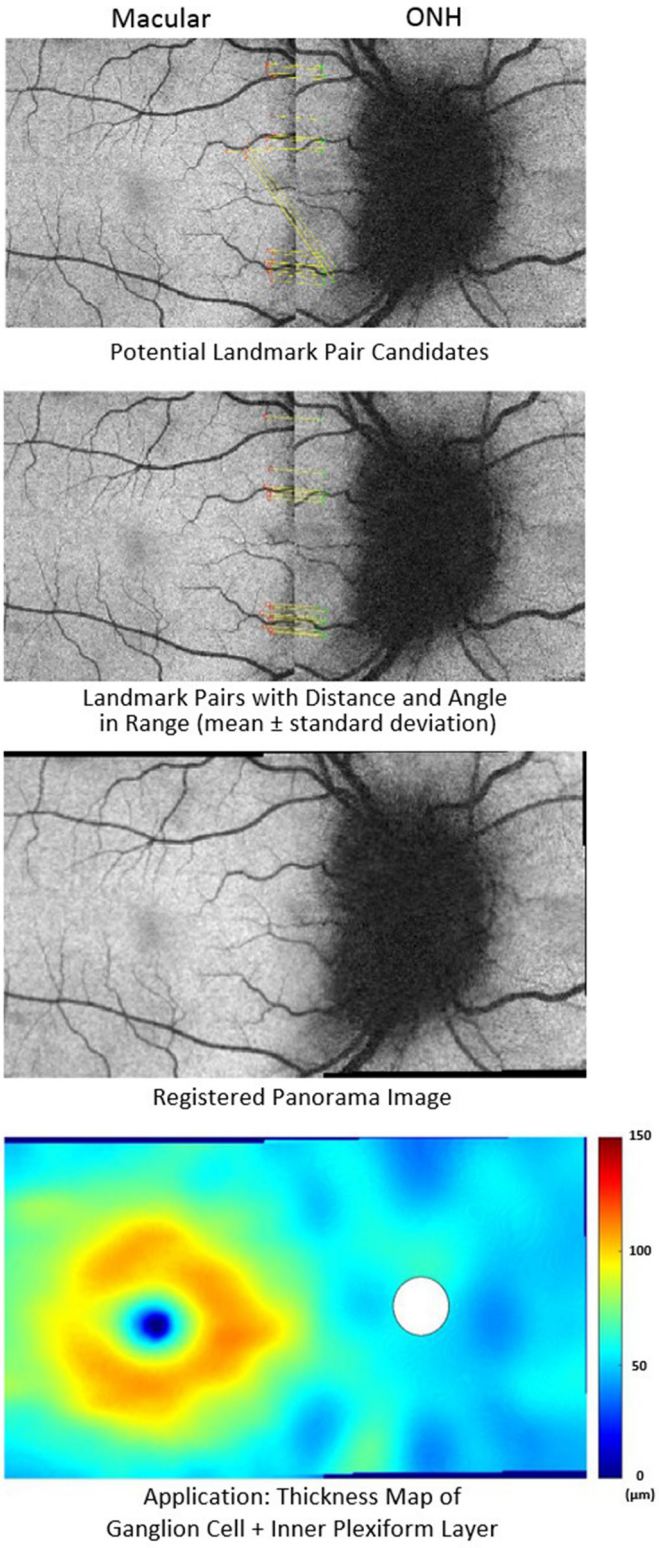

Fig. 2. Example of Landmark Selections and Registration Results
Commercial Relationships: Qingyang Su, None; **Jui-Kai Wang**, None; **Mohammad Saleh Miri**, None; **Victor A. Robles**, None; **Mona K. Garvin**, The University of Iowa (P)

Support: U10 EY01728101A1, U10 EY01738701A1, 3U10EY01728101A1S1, R01 EY023279, VA-ORD, Iowa City VA Center for The Prevention and Treatment of Visual Loss
Clinical Trial: NCT01003639

Program Number: 647 **Poster Board Number:** B0394
Presentation Time: 3:15 PM–5:00 PM

Frame averaging and automated segmentation technique for foveal avascular zone quantification with optical coherence tomography angiography

Taly G. Schmidt[1], Rachel E. Linderman[2], Margaret R. Strampe[3], Joseph Carroll[2, 4]. [1]Biomedical Engineering, Marquette University, Milwaukee, WI; [2]Ophthalmology and Visual Sciences, Medical College of Wisconsin, Milwaukee, WI; [3]University of Minnesota Medical School, Minneapolis, MN; [4]Cell Biology, Neurobiology, & Anatomy, Medical College of Wisconsin, Milwaukee, WI.

Purpose: Metrics quantifying the Foveal Avascular Zone (FAZ) in Optical Coherence Tomography Angiography (OCTA) images may be useful biomarkers for retinal vascular diseases. However, robust estimation of FAZ metrics is challenged by image noise and blur. This study investigated an automated frame averaging and segmentation technique for FAZ metric estimation.
Methods: Ten OCTA image frames were acquired for each of 19 subjects using the Optovue's AngioVue (Fremont, CA). For each subject, the five frames with highest image quality, as quantified by mean gradient magnitude, were sorted by image quality and spatially registered (StackReg: Rigid Body, ImageJ). Average images were calculated as the mean of one to five registered frames. The averaged images were input to an automated FAZ segmentation algorithm based on vessel edge detection. For each subject, three masked, expert readers manually segmented the FAZ on the averaged image of five frames. The expert segmentations were statistically combined to form a ground truth FAZ region. The agreement of the algorithm FAZ segmentation to the ground truth was quantified by Dice coefficient. Metrics of FAZ area, perimeter, and centroid were calculated for algorithm FAZ segmentations and compared to ground truth values.
Results: The automated algorithm identified the correct FAZ region in 18 of 19 subjects. One subject presented an ambiguous FAZ with small avascular regions in the central fovea. The mean Dice coefficients of agreement between the algorithm and expert segmentations were 0.94±0.04 when using the best frame and 0.96±0.04 when averaging three or more frames. Averaging three or more frames reduced the error in the FAZ metrics (see Table). For example, the error in the estimated FAZ area was 6.2% when using one frame compared to 3.2% for three frames and 2.6% error when averaging five frames.
Conclusions: Averaging three to five OCTA frames improved the accuracy of FAZ metrics estimated by the automated FAZ segmentation algorithm. The proposed technique may facilitate robust estimation of FAZ biomarkers for evaluating retinal vascular diseases and monitoring therapeutic interventions.

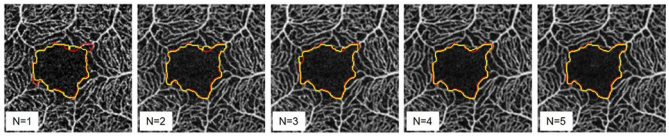

Averaged image of N frames for one example subject with expert (yellow) and algorithm (red) segmentations.

Number of averaged frames	1	2	3	4	5
Area	6.2±6.0	8.2±17.2	3.2±4.4	3.1±4.0	2.6±4.0
Perimeter	8.5±6.8	10.5±14.3	6.5±7.1	6.2±6.4	6.1±6.9
Centroid	1.4±1.0	1.8±2.6	1.1±0.7	1.0±0.6	1.0±0.6

The absolute percent error (mean±std) of FAZ metrics estimated for different numbers of averaged frames.

Commercial Relationships: Taly G. Schmidt, None; **Rachel E. Linderman**, None; **Margaret R. Strampe**, None; **Joseph Carroll**, Optovue, Inc. (F)
Support: NIH Grant P30EY001931, NIH Grant R01EY024969, Fight for Sight, Way Klingler Sabbatical Fellowship

Program Number: 648 **Poster Board Number:** B0395
Presentation Time: 3:15 PM–5:00 PM
Curvelet-based Vessel Enhancement for 3D OCT Angiography

Yonggang Shi[1], Jin Gahm[1], Amir H. Kashani[2]. [1]Stevens Neuroimaging and Informatics Institute, University of Southern California, Los Angeles, CA; [2]USC Roski Eye Institute and Department of Ophthalmology, University of Southern California, Los Angeles, CA.

Purpose: Recent studies have successfully used OCT Angiography (OCTA) to extract *2D* metrics for the quantitative assessment of capillary morphology and density. While highly valuable, these 2D OCTA metrics were derived from the *en face* projection of the 3D OCTA data, and therefore inevitably obscure the geometric and topological information in the original 3D vasculature networks. To robustly compute truly 3D metrics for the automated analysis of OCTA data in large scale eye studies, it is important to first develop robust 3D vessel enhancement methods from OCTA data.

Methods: Conventional filtering methods tend to obscure small vessels when they try to suppress the noise in 3D OCTA data. In this work, we propose the use of a model-based filtering approach based on the curvelet transform (Candes E et al., 2010). The key idea is that the curvelet basis functions provide a multiscale representation of edges and singularities along curve-like structures in 3D images, which matches very well with the geometry of retinal vasculature in OCTA images. Before we process the OCTA image, the IOWA Reference Algorithm (Abramoff MD et al., 2010) is first applied to segment the retinal layers. For each 3D OCTA volume, we then apply the 3D wrapping-based curvelet transform at 5 scales with 8 orientations. Denoising is then achieved by adaptively thresholding the curvelet coefficients at multiple scales in proportion to the noise level, which is automatically computed from the outer nuclear layer (ONL).

Results: To demonstrate our curvelet-based method for 3D OCTA analysis, we show the results from a normal control and a patient with diabetic retinopathy. The input data is the raw 3D image volume from the OCT scanner. Using the denoised 3D OCTA image, we generated *en face* Maximum Intensity Projection (MIP) images and color-coded the images with the depth of the projected vasculature. To achieve invariance with respect to retinal anatomy, we calculate the depth as the distance to the boundary of ONL. From the results shown in Figure 1, we can clearly see that our method is able to reconstruct the fine-grained retinal vasculature while removing noise in the OCTA data.

Conclusions: With our novel methods based on curvelet transforms, we can achieve high quality 3D donoising while preserving detailed retinal vasculature. This provides a foundation for further development of 3D OCTA analysis algorithms.

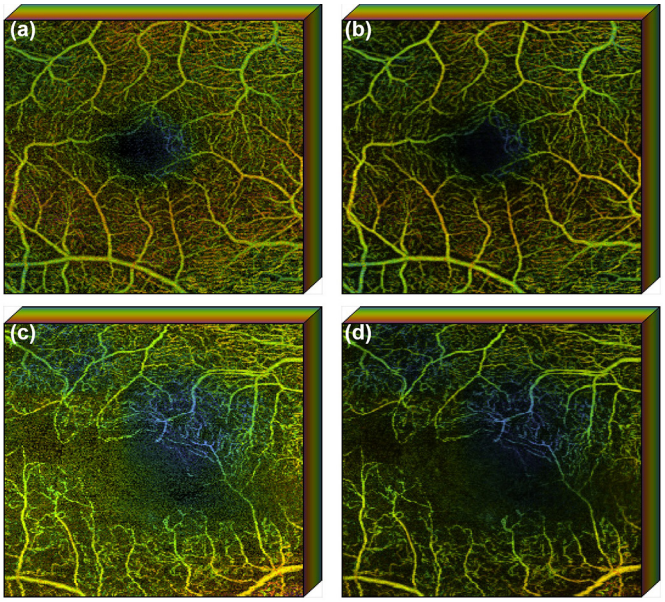

Figure 1. With curvelet-based denoising, we can effectively remove noise in 3D OCTA image while preserving detailed vasculature. The color-coded *en face* MIP of OCTA images are shown to demonstrate the 3D depth of the retinal vasculature. The MIP of OCTA data from a normal control before and after curvelet analysis are shown in (a) and (b), respectively. The MIP of OCTA data from a patient with diabetic retinopathy before and after curvelet analysis are shown in (c) and (d), respectively.

Commercial Relationships: Yonggang Shi, None; **Jin Gahm**, None; **Amir H. Kashani**, Carl Zeiss Meditec (F), Carl Zeiss Meditec (R), Carl Zeiss Meditec (C)
Support: NIH Grant P41EB015922, NIH Grant UH2NS100614, NIH Grant U01EY025864, NIH Grant K08EY027006, Carl Zeiss Meditec Research to Prevent Blindness

Program Number: 649 **Poster Board Number:** B0396
Presentation Time: 3:15 PM–5:00 PM
Convolutional neural networks for artifact free OCT retinal angiography

Maciej Szkulmowski[1], Pawel Liskowski[2], Bartosz Wieloch[2], Krzysztof Krawiec[2], Bartosz Sikorski[3, 4]. [1]Institute of Physics, Nicolaus Copernicus Univ, Torun, Poland; [2]Laboratory of Intelligent Decision Support Systems, Poznan University of Technology, Poznan, Poland; [3]Collegium Medicum, Nicolaus Copernicus University, Bydgoszcz, Poland; [4]Department of Ophthalmology, Nicolaus Copernicus University, Bydgoszcz, Poland.

Purpose: To demonstrate ability of deep convolutional neural network (CNN) to provide noninvasive visualization of retinal microcapillary network (RMN) in retinal diseases in with the use of data from a device combining Scanning Laser Ophthalmoscope (SLO) and Spectral Optical Coherence Tomography (SOCT). SLO system provides fast eye tracking system while SOCT delivers 3D data for knowledge-free vessel segmentation technique. The approach allows RMN to be presented in form of 3D visualization as well as in forms of angiographic maps of different retinal layers free of shadow artifacts blurring standard RMS visualizations.

Methods: The study was performed with SOCT laboratory setup (100,000 Ascans/sec, 4.5 um axial resolution, 91 dB detection sensitivity). Constant 30 Hz retinal preview is provided by the SLO device and is used to guide the SOCT scanning beam to the region of interest. RMS maps are created from 3D SOCT data using supervised

machine learning algorithm exploiting deep convolutional neural network trained on exemplary data acquired from a set of 15 eyes (from both healthy volunteers and patients with retinal diseases) with vessels labeled by three independent skilled specialists. Training is performed using random-split and biased-split approaches to divide labeled data to training and test sets. Architecture of the CNN consists of 7 layers. Training is carried out by stochastic gradient descent with batch updates and momentum, which is equivalent to optimizing the multinomial logistic regression objective.
Results: Trained CNNs provide sensitivity and specificity for RMN detection in training sets between 0.95 and 0.98 depending on training algorithm. We will show RMN maps obtained using CNNs with both proposed approach for 5 healthy volunteers and 12 patients with diabetic retinopathy, branch retinal vein occlusion and central retinal vein occlusion. We will compare the angiographic maps obtained for different retinal layers using CNN with maps obtained using standard phase-variance and complex difference angiographic algorithms.
Conclusions: Our results shows that CNN approach to RMN visualization provides accurate vessel detection incorporating a priori knowledge of skilled specialists and allows for increased sensitivity and specificity of SOCT based angiography. It also allows for generation of angiographic maps free of artifacts linked to vessel shadows in deeper layers.
Commercial Relationships: Maciej Szkulmowski, None; **Pawel Liskowski**, None; **Bartosz Wieloch**, None; **Krzysztof Krawiec**, None; **Bartosz Sikorski**, None

Program Number: 650 **Poster Board Number:** B0397
Presentation Time: 3:15 PM–5:00 PM
Compensation for reflectance variation in flow index quantification by optical coherence tomography angiography
Simon S. Gao, Yali Jia, Liang Liu, Hana L. Takusagawa, John C. Morrison, David Huang. Ophthalmology, Oregon Health & Science University, Portland, OR.
Purpose: To compensate for reflectance variation when quantifying flow index by optical coherence tomography angiography (OCTA).
Methods: Macular scans of healthy participants were taken using a spectral OCT system (Avanti). Participants received 2 or 3 OCTA scans covering a 3×3 mm area centered on the macula. The data was exported and analyzed with custom software. The SSADA algorithm was used to detect flow. Maximum flow projection of the inner retinal slab produced the *en face* angiogram. The reflectance of the maximum flow voxel was used to construct an *en face* vascular reflectance map. Larger vessels were identified by an automated algorithm that identified their high ratio of flow signal to outer retinal reflectance and separated from capillaries on the *en face* angiograms. Flow index was calculated by averaging the flow signal in the *en face* angiogram.
Results: Macular scans of healthy participants were taken using a spectral OCT system (Avanti). Participants received 2 or 3 OCTA scans covering a 3×3 mm area centered on the macula. The data was exported and analyzed with custom software. The SSADA algorithm was used to detect flow. Maximum flow projection of the inner retinal slab produced the *en face* angiogram. The reflectance of the maximum flow voxel was used to construct an *en face* vascular reflectance map. Larger vessels were identified by an automated algorithm that identified their high ratio of flow signal to outer retinal reflectance and separated from capillaries on the *en face* angiograms. Flow index was calculated by averaging the flow signal in the *en face* angiogram.
Conclusions: Compensating for reflectance variation improved the reliability of flow index quantification.

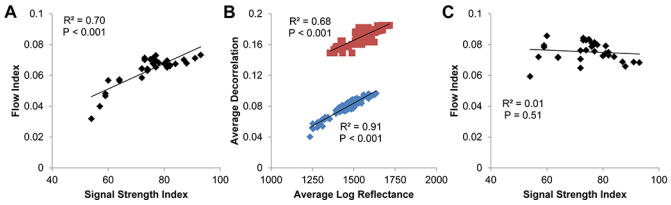

Figure 1. (A) In a group of 13 healthy eyes which received 2 or 3 scans each, the flow index of the superficial retina, excluding the FAZ, was correlated to the signal strength index (SSI) of the scan. (B) The average decorrelation (flow signal) and average log reflectance of larger retinal vessels (red) and capillaries (blue) were correlated. Data were from *en face* images of the inner retina (ILM to OPL). (C) By scaling the decorrelation values based on reflectance according to the fits in panel B, the positive relationship between SSI and flow index was removed.
Commercial Relationships: Simon S. Gao, None; **Yali Jia**, Optovue (F), Optovue (P); **Liang Liu**, None; **Hana L. Takusagawa**, None; **John C. Morrison**, None; **David Huang**, Optovue (I), Carl Zeiss Meditec (P), Optovue (F), Optovue (R), Optovue (P)
Support: This work was supported by NIH grants R01 EY023285, R01 EY024544, DP3 DK104397, P30 EY010572, and unrestricted departmental funding from Research to Prevent Blindness.

Program Number: 651 **Poster Board Number:** B0398
Presentation Time: 3:15 PM–5:00 PM
A Method for Quantitative Assessment of Retinal Vessel Tortuosity Imaged by Optical Coherence Tomography Angiography
Maziyar M Khansari[1, 2], Jennifer I. Lim[2], Mahnaz Shahidi[2].
[1]BioEngineering, University of Illinois at Chicago, Chicago, IL; [2]Ophthalmology and Visual Sciences, University of Illinois at Chicago, Chicago, IL.
Purpose: Optical coherence tomography angiography (OCTA) provides non-invasive imaging of retinal capillary network and may be useful for detection of vascular morphological alterations due to diseases. The purpose of the current study is to report an image analysis method for quantification of retinal vessel tortuosity in healthy and sickle cell retinopathy (SCR) subjects based on OCTA images.
Methods: OCTA was performed in one eye of 5 healthy control (NC) and 5 SCR subjects. Images of the superficial retinal capillary network were generated in a 3 mm × 3 mm region centered on the fovea. A dedicated customized software algorithm was developed for assessment of tortuosity in retinal vessels. K-means clustering algorithm and morphological image processing were used for vessel segmentation. Vessel centerlines between bifurcation points were extracted using distance transformations. A vessel tortuosity index (VTI) was derived using variation of in-plane curvature of points along the vessel centerline, number of inflection points (twists) and the magnitude of curvature. The method was validated using images of sinusoidal waves with variable amplitude and frequency. VTI measurements were compared in the 2 groups of subjects using unpaired t- test. Significant was accepted at $P < 0.05$.
Results: As expected, for the sinusoidal waves at a constant frequency, VTI increased with increasing the magnitude. Similarly, for the sinusoidal waves at a constant magnitude, VTI increased with increasing the frequency. There was no statistically significant age difference between the NC (38±12 years) and SCR subjects (48±12 years) ($P=0.2$). Compiled data yielded a total of VTI measurements in 181 and 154 vessels in NC and SCR subjects, respectively. VTI in

SCR (0.5±0.3) was significantly higher than NC (0.3±0.2) subjects ($P < 0.001$).
Conclusions: A novel method for assessment of tortuosity of retinal vessels in OCTA was demonstrated. This method can be useful for detection of retinal vascular tortuosity alterations due to systemic and ocular diseases.
Commercial Relationships: Maziyar M Khansari; **Jennifer I. Lim**, None; **Mahnaz Shahidi**, None
Support: NIH Grant KD 104393, NIH Grant EY 001792, research to prevent blindness

Program Number: 652 **Poster Board Number:** B0399
Presentation Time: 3:15 PM–5:00 PM
Measuring asymmetry of the foveal avascular zone in subjects with Type 1 Diabetes Mellitus using OCTA
Radhika Ragam[1], Bernard Szirth[1], Albert S. Khouri[1], Kelly A. Soules[2]. [1]Rutgers New Jersey Medical School, Flemington, NJ; [2]OptoVue, Freemont, CA.
Purpose: Foveal avascular zone (FAZ) varies among healthy subjects (0.02 to 0.63mm^2), and enlarges in subjects with Type 1 Diabetes Mellitus (T1DM). Optical coherence tomography angiography (OCTA) can measure XY values, asymmetry, and shape of the FAZ in subjects with T1DM. The aim was to study FAZ asymmetry in relation to age, gender, duration of T1DM, and most recent HbA1c level.
Methods: We analyzed 111 subjects (37 males and 74 females) with T1DM ranging from 6 to 54 years old, and a mean HbA1c of 7.61. Eyes were imaged and post capture analysis was performed using proprietary software in the AngioVue OCTA system. Only high quality FAZ images were included. Subjects with acceptable bilateral FAZ images underwent asymmetry grading based on clearness of contour and direction of largest diameter of the FAZ. The grading scale was: 0 for no asymmetry, 1 for mild asymmetry, 2 for moderate asymmetry, and 3 for severe asymmetry. One-way ANOVA and Tukey post-hoc tests were used to determine if subjects from each group (0-3) had significant differences in their duration of T1DM, age, and last HbA1c. An independent-sample T-test was used to determine if males or females showed more FAZ asymmetry.
Results: More asymmetric FAZ was associated with longer duration of T1DM. Statistically significant differences were found in the duration of T1DM between score group 0 and 2 ($p<0.001$), 0 and 3 ($p<0.001$), 1 and 2 ($p<0.001$), and 1 and 3 ($p<0.001$). No significant difference in the duration of T1DM was found between score groups 0 and 1, and 2 and 3. There was a significantly higher average age in score group 2 than 0 ($p<0.001$), 3 than 0 ($p<0.001$), 2 than 1 ($p=0.002$), and 3 than 1 ($p=0.001$). Overall the average ages for score groups 0-3 were 15.0, 19.2, 24.1, and 33.6, respectively. No significant difference between gender or most recent HbA1c level was found with increasing asymmetry of the FAZ.
Conclusions:
Duration of T1DM correlated with increasing asymmetry of the FAZ. In subjects with T1DM, enlargement and increasing asymmetry of the FAZ may reflect microinfarction of the vascular arcades due to longer duration of T1DM. FAZ Asymmetry due to interruptions in the retinal vasculature capillary network may be observed by OCTA, and used as a valuable screening tool for tracking eyes over time of subjects affected by T1DM. Future studies will concentrate on gender and shape of the FAZ.
Commercial Relationships: Radhika Ragam; **Bernard Szirth**, None; **Albert S. Khouri**, None; **Kelly A. Soules**, OptoVue (E)

Program Number: 653 **Poster Board Number:** B0400
Presentation Time: 3:15 PM–5:00 PM
Smoothed and Resolved Thresholding (SmaRT-) Display: A New OCTA Display Technique to Resolve the Low Flow Ambiguity
Patrick Yiu[1], Eric M. Moult[1], Stefan B. Ploner[2], ByungKun Lee[1], Lennart Husvogt[2], Andreas K. Maier[2], Richard Spaide[3], Jay S. Duker[4], Nadia Waheed[4], James G. Fujimoto[1]. [1]Department of Electrical Engineering and Computer Science, Massachusetts Institute of Technology, Cambridge, MA; [2]Pattern Recognition Lab, Friedrich-Alexander-Universität Erlangen-Nürnberg, Erlangen, Germany; [3]Vitreous, Retina, Macula Consultants of New York, New York, NY; [4]New England Eye Center at Tufts Medical Center, Boston, MA.
Purpose: OCT angiography (OCTA) provides clinicians with a new perspective on ocular vasculature. However, OCTA is fundamentally different from OCT, and its complex processing steps generate new artifacts that are not present in OCT. The "thresholding" step in OCTA, which removes (makes black) regions of low OCT signal, results in an ambiguity between areas of low OCT signal and areas of low blood flow. In this study we present a new OCTA display technique, SmaRT-Display OCTA, which obviates this ambiguity.
Methods: We propose a mapping scheme based on the hue-saturation-value (HSV) colorspace wherein the OCT signal is mapped to a sigmoidal curve in the value coordinate, the unthresholded OCTA signal is mapped to the saturation coordinate, and the hue coordinate is fixed at red.
Results: SmaRT-Display removes low flow ambiguities in both cross-sectional and en face views.
Conclusions: SmaRT-Display has the potential to reduce misinterpretation of OCTA images and is a first step in expanding the standards of how OCTA data can be presented.

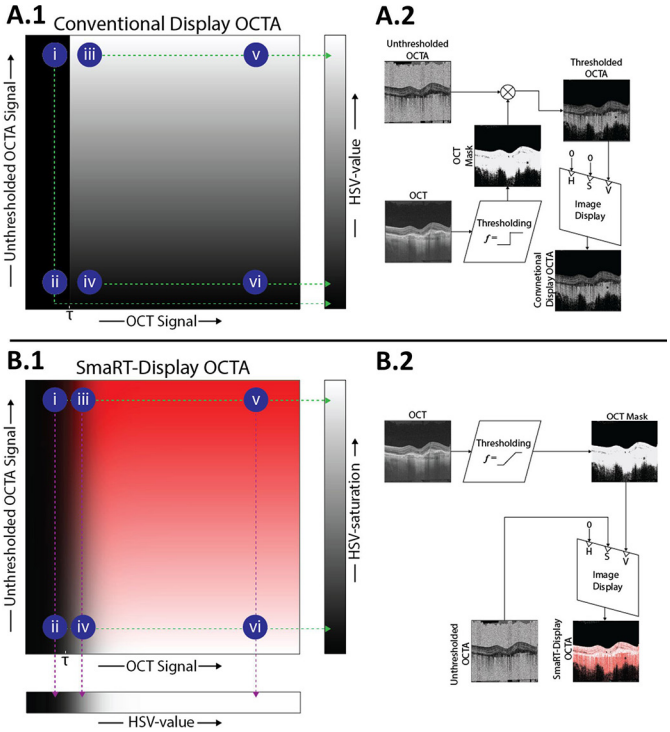

Figure 1: Conventional display vs. SmaRT-Display OCTA. (A.1) In the conventional display OCTA, i and ii, which are below the threshold tau, are mapped to same value; this value is essentially indistinguishable from the value to which iv and vi are mapped; finally, iii and v are mapped to the same value. These non-invertible mappings induce ambiguities. (B.1) Using SmaRT-Display, the mappings to the display color space are invertible. (A.2, B.2) Signal flow graphs for the conventional display and SmaRT-Display schemes, respectively.

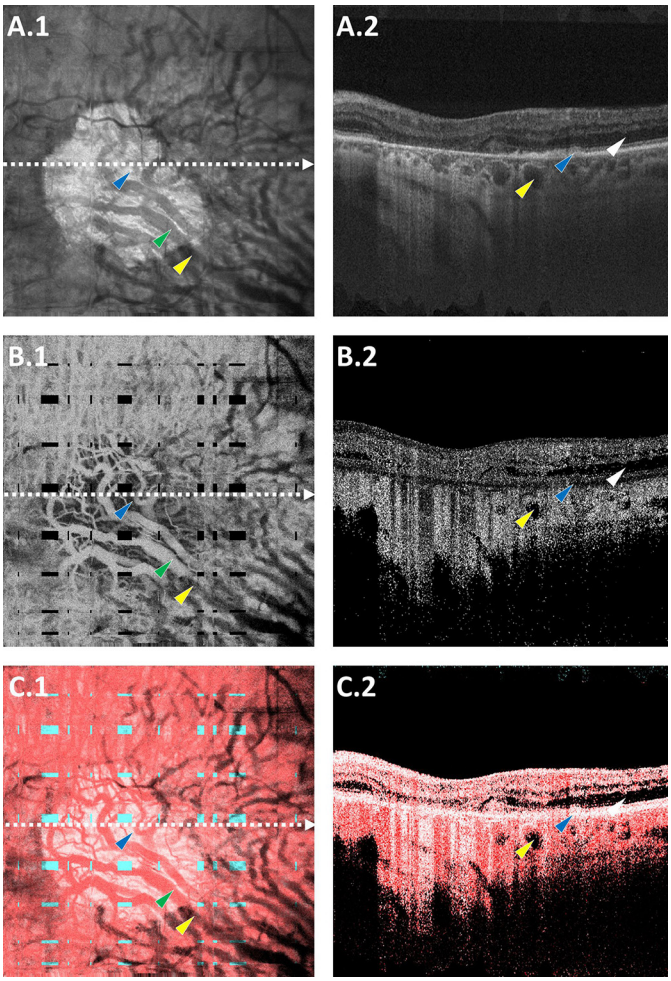

Figure 2: (A) OCT, (B) conventional display OCTA, and (C) SmaRT-Display OCTA from an eye with geographic atrophy. First column: en face projections of 110um slab; the black (teal) rectangles in B.1 (C.1) are motion artifacts. Second column: B-scans from dashed white lines in first column. Blue arrows point to areas of low flow with OCT signal above the threshold (en face: intervascular stroma; B-scan: retinal pigment epithelium). Green arrows point to area of high flow with OCT signal above the threshold (en face: choroidal vessel in region of atrophy). Yellow arrows point to areas of high flow with OCT signal below the threshold (en face and B-scan: choroidal vessels outside region of atrophy). White arrows point to area of low flow with OCT signal below the threshold (B-scan: outer nuclear layer).

Commercial Relationships: Patrick Yiu, None; **Eric M. Moult**, None; **Stefan B. Ploner**, None; **ByungKun Lee**, None; **Lennart Husvogt**, None; **Andreas K. Maier**, None; **Richard Spaide**, Topcon Medical Systems, Inc. (R), Topcon Medical Systems, Inc. (C); **Jay S. Duker**, Optovue, Inc. (F), Topcon Medical Systems, Inc. (F), Carl Zeiss Meditec, Inc. (F), Topcon Medical Systems, Inc. (C), Optovue, Inc. (C), Carl Zeiss Meditec, Inc. (C); **Nadia Waheed**, Carl Zeiss Meditec, Inc. (R), MVRF (F), Genentech (C), Janssen (C), Ocudyne (C), Optovue, Inc. (R), Regeneron (C), Nidek (R); **James G. Fujimoto**, Royalties from intellectual property owned by MIT and licensed to Optovue, Inc. (P), Optovue, Inc. (I), Royalties from intellectual property owned by MIT and licensed to Carl Zeiss Meditec, Inc. (P)

Support: NIH: 5-R01-EY011289-28; AFOSR: FA9550-15-1-0473, FA9550-10-1-0551; MVRF

Program Number: 654 **Poster Board Number:** B0401
Presentation Time: 3:15 PM–5:00 PM
Detection of plus disease in retinopathy of prematurity using automatic vessel tortuosity measurements
Jeffrey C. Wigdahl[1], Carla Agurto[1], Sheila C. Nemeth[1], Vinayak S. Joshi[1], Wendall Bauman[2], Peter Soliz[1], E Simon Barriga[1]. [1]VisionQuest Biomedical, Albuquerque, NM; [2]Retina Institute of South Texas, San Antonio, TX.
Purpose: Retinopathy of prematurity (ROP) is the leading cause of avoidable blindness in children. Plus disease is defined by increased venous dilation and arteriolar tortuosity of the posterior retinal vessels, and is a sign that ROP is active and can progress. We present an automatic method combining image enhancement, vessel segmentation and tortuosity measurement to detect the presence of plus disease in retinal images.
Methods: Image Enhancement: To reduce the noise, we first apply a median filter, then we apply a shade correction method to remove non-uniform illumination, followed by anisotropic diffusion. Finally, we apply contrast limit adaptive histogram equalization (CLAHE) using uniform distribution correction.
Vessel Segmentation: We use a multiscale enhancement technique and then perform CLAHE using the exponential distribution.
The threshold is found by calculating the vessel density at a fixed threshold value (0.5), and adjusting based on that density. Finally, the vasculature is skeletonized and crossing/branching points are removed.
Tortuosity: Four measurements are calculated for 30-pixel vessel segments: 1) arc/chord ratio, 2) total curvature using numerical differentiation, 3) combination of method 1, magnitude of curvature and curvature sign changes, and 4) method 1 without dividing the vessel in segments. Tortuosity is measured for each image in an imaging sequence. The top 3 tortuous segments found in each case are then averaged.
Results: Our dataset consists of 86 imaging sessions of preterm babies <31 weeks gestational age and <1kg birth weight. Clinical ground truth was the dilated examination by a retina specialist that showed 25 sessions had plus disease and 61 did not. We tested each tortuosity method for the classification of plus disease. Best results were achieved by method 2 with an AUC of .86, maximum accuracy of 72% and sensitivity/specificity of 0.92/0.61. Example in Fig. 1. Agreement was calculated (Cohen's kappa) between: clinical ground truth and the gradings from a reader (.20), and clinical ground truth and the algorithm output (.57).
Conclusions: We demonstrated that our automatic approach can detect cases with plus disease with high sensitivity and better agreement with the clinical ground truth than the reader, making the system ideal as a screening tool.

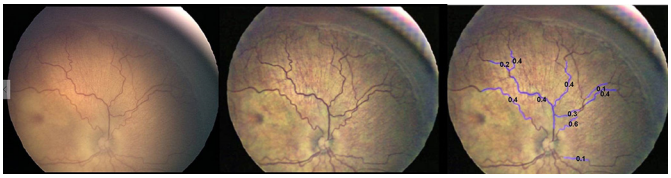

Fig. 1: Plus disease case. a) Original image, b) enhanced image, c) tortuosity measurements (method 2).
Commercial Relationships: Jeffrey C. Wigdahl, VisionQuest Biomedical (E); **Carla Agurto**, VisionQuest Biomedical (E); **Sheila C. Nemeth**, VisionQuest Biomedical (E); **Vinayak S. Joshi**, VisionQuest Biomedical (E); **Wendall Bauman**, Retina Institute of South Texas (C); **Peter Soliz**, VisionQuest Biomedical (E); **E Simon Barriga**, VisionQuest Biomedical (E)
Support: R44 EY023474

Program Number: 655 **Poster Board Number:** B0402
Presentation Time: 3:15 PM–5:00 PM
Web-based Smart Retinal Vessel Analysis System (VASP)
Maryam Mehdizadeh[1], Shuang Yu[1], Shaun Frost[1], Di Xiao[1], Mei-Ling Tay-Kearney[2], Yogesan Kanagasingam[1]. [1]The Commonwealth Scientific and Industrial Research Organisation (CSIRO), Floreat, WA, Australia; [2]Lions Eye Institute, Perth, WA, Australia.
Purpose: We have developed and tested a fast web-based retinal vascular analysis program called VASP. This web-based database driven tool allows multiple users to access the service simultaneously to process retinal images and calculate vascular parameters. The parameters get stored in a central secure database for data analysis and identification of potential retinal biomarkers using machine learning techniques.
Methods: Retinal images from various fundus cameras are imported, pre-processed and undergo automated detection of optic disc and vessel network. Vessels are automatically labelled as arteries and veins and bifurcations and cross-overs are classified. User input is obtained at multiple stages to correct errors in the automated algorithms. The generated parameters, intermediate results, and data relations including graph structures are stored in a centralized database for future data analysis of potential identification of retinal biomarkers or automatic testing of newly implemented techniques. Label propagation through the vessel network and graph structure is encoded in the data visualization techniques so that minimal user interaction is required to correct and adjust the vessel networks. The Dynamic data visualizations allow the user to adjust the vessel widths, and the largest six arteries and veins. A set of 22 color fundus images are used to test the system. Images are 1500x1152 pixels covering 45 field of view.
Results: The average time to process images including user interaction is 4 minutes. Most of the diagnosis is done automatically. As displayed on the Fig.1, the system allows users to correct vessel network graph (Fig. 1(A)), adjust vessel width measurement (Fig. 1(B)) and edit largest artery vein vessels (Fig. 1(C)).
Conclusions: The preliminary results demonstrate that the system is effective and intelligent to generate vessel parameters. Processing time, ease of use, and clinical effectiveness were our main focus to develop VASP. We are using VASP to analyze images from patients with hypertension and stroke.

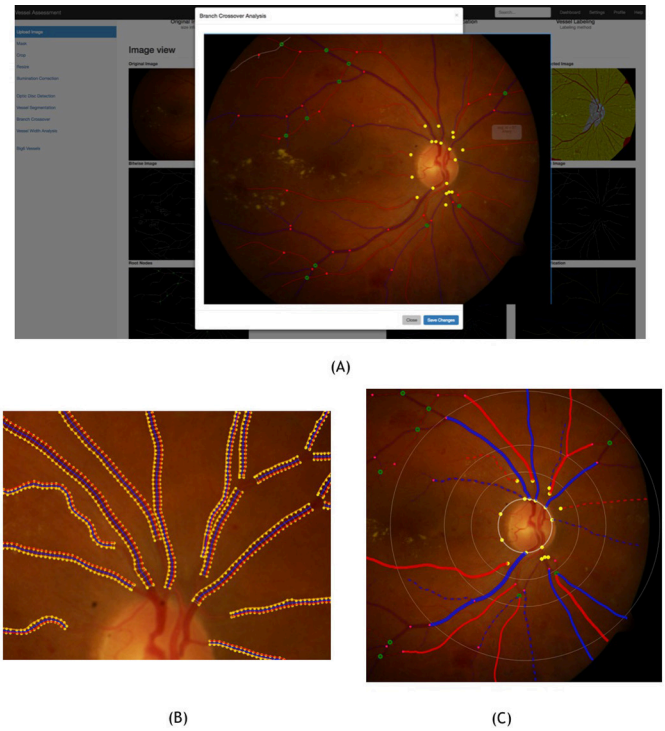

(A) Vessel tree and Artery/Vein classification, (B) Vessel width measurement and adjustment, (C) Largest 6 artery and vein vessels in Zones B and C

Commercial Relationships: Maryam Mehdizadeh, None; **Shuang Yu**, None; **Shaun Frost**, None; **Di Xiao**, None; **Mei-Ling Tay-Kearney**, None; **Yogesan Kanagasingam**, None

Program Number: 656 **Poster Board Number:** B0403
Presentation Time: 3:15 PM–5:00 PM

Graph Theory Based Intelligent Retinal Vessel Analysis

Shuang Yu, Maryam Mehdizadeh, Shaun Frost, Di Xiao, Yogesan Kanagasingam. Commonwealth Scientific and Industrial Research Organisation (CSIRO), Perth, WA, Australia.

Purpose: An intelligent retinal vessel analysis program is developed in this research. The program is based on graph theory and requires minimal user interactions for retinal vessel network analysis.

Methods: Automatic image processing algorithms have been developed to extract the vessel graph structure with procedures of optic disc detection, vessel segmentation, branch/crossover identification, root node detection and graph tree extraction. Afterward, arterioles/venuoles (A/V) are classified using Kmeans clustering and fine-tuned with the graph structure among vessel segments. User interaction is enabled at every step to rectify the automatic result.

In order to make the system more intelligent and minimize user effort, a set of self-consistency checking rules are designed to automatically detect errors in the extracted vessel graph structure. The checking rules are established based on 3 assumptions for the correct vessel tree: 1, it has and only has one root node; 2, it can only contain bifurcation points and contain no crossover points within itself; 3, it contains no closed loops. The incorrectly extracted trees are automatically detected and highlighted, so that users can allocate their attention wisely to rectify the incorrect ones. After proper user intervention, vessel parameters are automatically calculated, including but not limited to central retinal equivalent calibers, A/V width ratio, fractal dimension, lacunarity, tortuosity, central reflex and branching parameters etc.

The system was preliminarily tested on 14 disc centered color fundus images captured with a Canon CR-1 non-mydriatic camera at field of view.

Results: Fig. 1B shows the automatically extracted tree graph for the image shown on 1A. The incorrect vessels are highlighted in white. 1C and 1D show the user rectified tree graph and A/V classification respectively. According to the preliminary test, the system is able to improve the A/V classification accuracy from 55.42% to 100% within 5 minutes of user interaction in average.

Conclusions: We have developed a graph theory based retinal vessel analysis system, which is able to provide intelligent hints on necessary user interventions. Therefore, users are enabled to correct the vessel structure with high efficiency and minimal interaction.

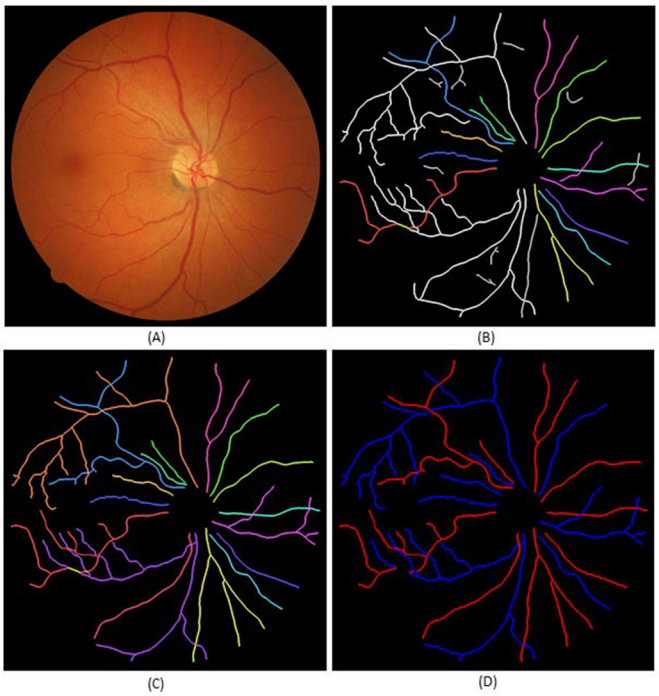

Fig.1 A, Color fundus image; B, Automatically extracted vessel graph and incorrect trees are colored in white; C, Rectified vessel graph; D, A/V classification.

Commercial Relationships: Shuang Yu, None; **Maryam Mehdizadeh**, None; **Shaun Frost**, None; **Di Xiao**, None; **Yogesan Kanagasingam**, None

Program Number: 657 **Poster Board Number:** B0404
Presentation Time: 3:15 PM–5:00 PM
Quantitative shadow compensated optical coherence tomography of choroidal vasculature

Kiran Vupparaboina[5, 2], Kunal K. Dansingani[3, 6], Abhilash G. Marupally[1], Muhammad Fayez Jawed[3], Soumya Jana[2], K Bailey Freund[7, 4], Jay Chhablani[8], Ashutosh Richhariya[5]. [1]Clinical Research, LV Prasad Eye Institute Hyderabad, Hyderabad, India; [2]Department of Electrical Engineering, Indian Institute of Technology Hyderabad, Hyderabad, India; [3]Truhlsen Eye Institute, University of Nebraska Medical Center, Omaha, NE; [4]LuEsther T Mertz Retinal Research Center, New York, NY; [5]Institute of Translational Research Engg and Advancement of Technology, LV Prasad Eye Institute Hyderabad, Hyderabad, India; [6]Vitreo-retinal Service, Moorfields Eye Hospital, London, United Kingdom; [7]Vitreous Retina Macula Consultants of New York, NY, NY; [8]Vitreo-retinal Service, LV Prasad Eye Institute Hyderabad, Hyderabad, India.

Purpose: Conventionally rendered optical coherence tomography (OCT) images of the posterior segment contain shadows which mask the visualization of deep structures such as the choroid. The choroidal vascularity index (CVI) is an OCT-derived estimated ratio of luminal to total choroidal volume (hyporeflective to total voxels). The purpose of this paper is to determine whether OCT shadow compensation alters the appearance of the choroid and the apparent CVI.

Methods: Twenty-seven subjects without any ocular disease underwent swept-source OCT imaging of the right eye, without averaging, and the resulting raw voxel maps were exported for further processing. The inner and outer choroidal boundaries were established using a structural similarity and tensor voting based algorithm. All scans were shadow compensated using a previously published algorithm, then binarized, using a novel algorithm recently described by our group, so that a CVI could be calculated from choroidal voxels. Images at each stage were inspected subjectively and the effect of shadow compensation on CVI was quantified objectively by Bland-Altman analysis.

Results: In shadow compensated OCT scans, the choroid was visualized with higher reflectivity than the neurosensory retina and the masking of deep tissues by retinal blood vessels was greatly reduced (figure). Mean CVI was 0.51 when calculated from non-shadow compensated scans, and 0.55 with shadow compensation. Bland-Altman analysis revealed a statistically significant CVI difference of 0.04 per eye (95% CI -0.05, -0.02).

Conclusions: Conventionally acquired OCT underestimates both choroidal reflectivity and calculated CVI. Shadow compensation corrects for masking which may improve accuracy of quantitative analysis. In healthy eyes, the darkest shadows are cast by retinal blood vessels. In eyes harboring pathology, OCT shadows cast by lesions such as hemorrhage or pigment epithelial detachment may predominate, particularly in regions of interest. Although the magnitude of the difference in CVI calculated from shadow compensated vs raw scans may be small in healthy eyes, this difference may become more pronounced in eyes with disease. Since shadow compensated OCT better represents actual tissue reflectivity, we believe it may improve accuracy for choroidal analysis in pathologic states. Further study is needed to test this hypothesis.

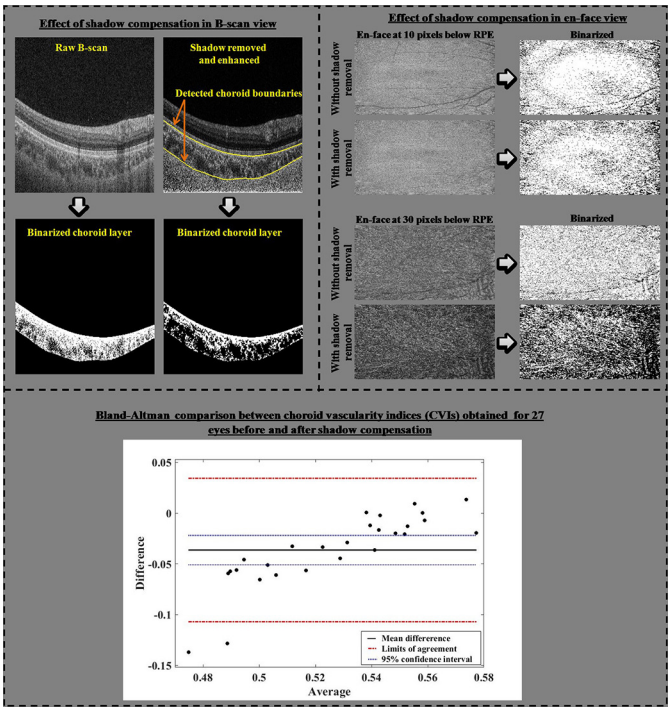

Choroid vasucularity: Raw OCT vs shadow compensated OCT.

Commercial Relationships: Kiran Vupparaboina; **Kunal K. Dansingani**, None; **Abhilash G. Marupally**, None; **Muhammad Fayez Jawed**, None; **Soumya Jana**, None; **K Bailey Freund**, Genentech (C), Optos (C), Optovue (C), Heidelberg Engineering (C), Bayer Healthcare (C); **Jay Chhablani**, None; **Ashutosh Richhariya**, None

Program Number: 658 **Poster Board Number:** B0405
Presentation Time: 3:15 PM–5:00 PM
Predicting Age-related Changes with High Accuracy using a Pattern Recognition Derived Retinal Ganglion Cell Regression Model

Nayuta Yoshioka[1, 2], Barbara Zangerl[1, 2], Lisa Nivison-Smith[1, 2], Sieu Khuu[2], Bryan W. Jones[3], Rebecca L. Pfeiffer[3], Robert E. Marc[3], Michael Kalloniatis[1, 2]. [1]Centre for Eye Health, University of New South Wales Australia, Kensington, NSW, Australia; [2]School of Optometry and Vision Science, University of New South Wales Australia, Sydney, NSW, Australia; [3]Department of Ophthalmology, Moran Eye Center, University of Utah, Salt Lake City, UT.

Purpose: We recently used pattern recognition analysis to show macula areas can be classified into statistically distinct clusters in accordance to their age-related retinal ganglion cell layer (RGCL) thickness change in a normal population. The aim of this study was to perform a retrospective cross-sectional analysis utilizing a large cohort of patients to establish accuracy of this model and to develop a normative dataset using a 50-year-old equivalent cohort.

Methods: Data was collected from patients seen at the Centre for Eye Health for optic nerve assessment without posterior pole disease. The grid-wise RGCL thickness was obtained from a single eye of each patient via Spectralis OCT macular scan over an 8×8 measurement grid. Measurements for patients outside the 45-54 age range (training cohort) were converted to 50-year-old equivalent value utilizing pattern recognition derived regression model which, in brief, consists of 8×8 grid clustered into 8 distinct classes according to the pattern of RGCL thickness change with age. Accuracy of the predictions was

assessed by comparing the training cohort's measurements to the 45-54 year reference cohort using t-test and one-way ANOVA.
Results: Data were collected from a total 248 patients aged 20 to 78.1 years. 80 patients within this group were aged 45 – 54 and formed the reference cohort (average±SD 49.6±2.83) and the remaining 168 eyes formed the training cohort (average age±SD 50.7±17.34). Converted values for the training set matched those of the reference cohort (average disparity±SD 0.10±0.42µm, range -0.74-1.34µm) and were not significantly different ($p > 0.9$). Most variability was observed with patients above 70 years of age (average disparity±SD -0.09±1.73µm, range -3.67 to 6.16µm) and central grids corresponding to the fovea (average disparity±SD 0.47±0.72µm, range -0.22 to 1.34µm).
Conclusions: Our regression model for normal age-related RGCL change can accurately convert and/or predict RGCL thickness for individuals in comparison to 50-year-equivalent reference cohort and could allow for more accurate assessment of RGCL thickness and earlier detection of significant loss in the future. Caution may be needed when applying the model in the foveal area or for patients older than 70 years.
Commercial Relationships: Nayuta Yoshioka, None; **Barbara Zangerl**, None; **Lisa Nivison-Smith**, None; **Sieu Khuu**, None; **Bryan W. Jones**, None; **Rebecca L. Pfeiffer**, None; **Robert E. Marc**, None; **Michael Kalloniatis**, None
Support: NHMRC 1033224; UNSW ECR Grant 2016 P535430; Australian Postgraduate Award; Guide Dogs NSW/ACT is a partner in the NHMRC grant and also provided a supplementary PhD scholarship for NY and support for LN-S; NIH EY02576, EY015128, EY014800, to Prevent Blindness Unrestricted Grant

Program Number: 659 **Poster Board Number:** B0406
Presentation Time: 3:15 PM–5:00 PM

Comparison of automated and expert human grading of diabetic retinopathy using smartphone-based retinal photography

Tyson Kim[1], Patrick Li[1], Leslie M. Niziol[1], Malavika Bhaskaranand[2], Sandeep Bhat[2], Chaithanya Ramachandra[2], Kaushal Solanki[2], Jose R. Davila[1], Frankie Myers[3], Clay Reber[3], David C. Musch[1], Todd P. Margolis[4], Daniel Fletcher[3], Maria A. Woodward[1], Yannis M. Paulus[1]. [1]Ophthalmology and Visual Sciences, University of Michigan Kellogg Eye Center, Ann Arbor, MI; [2]Eyenuk Inc, Woodland Hills, CA; [3]Bioengineering, University of California Berkeley, Berkeley, CA; [4]Ophthalmology and Visual Sciences, Washington University School of Medicine, St. Louis, MO.

Purpose: Diabetic retinopathy (DR) is the leading cause of vision loss and blindness in working-age adults. Retinal photography is a well-validated screening tool for DR but is expensive with limited portability. Smartphone-based photography addresses these limitations. We combine smartphone-based retinal photography with automated image analysis to detect referral-warranted DR (RWDR).
Methods: A mydriatic smartphone-based retinal camera (Cellscope Retina) was used to image diabetic patients at the University of Michigan Kellogg Eye Center Retina Clinic. Images were analyzed with cloud-based EyeApp software to generate screening recommendations (refer/no refer) based on presence of moderate non-proliferative DR or higher and/or markers for clinically significant macular edema (CSME). Images were independently evaluated by two masked readers for severity of DR and/or presence of CSME, and similarly categorized as refer/no refer. Results from EyeApp and masked readers were compared against clinical diagnosis made with slit-lamp biomicroscopy to determine sensitivity and specificity, at both eye-level and patient-level (RWDR defined at the patient-level if present in at least 1 eye of a subject).
Results: 72 patients (144 eyes) were imaged. RWDR was present in 101 eyes (77.1%) and absent in 30 eyes (22.9%) by gold standard clinical diagnosis. For detecting RWDR at the eye-level, EyeApp had a sensitivity of 77.4% and specificity of 70.4%; grader 1 had a sensitivity of 93.9% and specificity of 51.9%; grader 2 had a sensitivity of 88.8% and specificity of 63.0%. At the patient-level, RWDR was present in 55 subjects (76.4%) and absent in 12 subjects (16.7%). For detecting RWDR at patient-level, EyeApp had a sensitivity of 93.9% and specificity of 75.0%; grader 1 had a sensitivity of 98.1% and specificity of 41.7%; and grader 2 had a sensitivity of 96.0% and specificity of 41.7% (Figure 1).
Conclusions: CellScope Retina combined with EyeApp software achieves reasonable sensitivity and specificity in detection of RWDR at the person-level, with lower sensitivity but higher specificity than human graders. As the patient population studied had high prevalence of DR, additional study of a more typical screening population of diabetics in the community is needed.

Eye-Level Analysis

	Gold Standard Clinical Dx			
Grader Dx	RWDR	No RWDR	Sensitivity (95% CI)	Specificity (95% CI)
Grader 1				
RWDR	77	13	93.9 (86.5, 97.4)	51.9 (34.0, 69.3)
No RWDR	5	14		
Grader 2				
RWDR	71	10	88.8 (80.0, 94.0)	63.0 (44.2, 78.5)
No RWDR	9	17		
EyeApp				
RWDR	65	8	77.4 (67.4, 85.0)	70.4 (51.5, 84.2)
No RWDR	19	19		

Patient-Level Analysis

	Gold Standard Clinical Dx			
Grader Dx	RWDR	No RWDR	Sensitivity (95% CI)	Specificity (95% CI)
Grader 1				
RWDR	51	7	98.1 (89.9, 99.7)	41.7 (19.3, 68.1)
No RWDR	1	5		
Grader 2				
RWDR	48	7	96.0 (86.5, 98.9)	41.7 (19.3, 68.1)
No RWDR	2	5		
EyeApp				
RWDR	46	3	93.9 (83.5, 97.9)	75.0 (46.8, 91.1)
No RWDR	3	9		

RWDR: Moderate/Severe NPDR/PDR and/or Macular Edma
No RWDR: None/Mild NPDR and No Macular Edema

Sensitivity & specificity for referral-warranted diabetic retinopathy from CellScope Retina images using EyeApp and expert human grading

Commercial Relationships: Tyson Kim, CellScope Retina (P); **Patrick Li**, None; **Leslie M. Niziol**, None; **Malavika Bhaskaranand**, Eyenuk Inc (P), Eyenuk Inc (E); **Sandeep Bhat**, Eyenuk Inc (P), Eyenuk Inc (E); **Chaithanya Ramachandra**, Eyenuk Inc (P), Eyenuk Inc (E); **Kaushal Solanki**, Eyenuk (E), Eyenuk (P); **Jose R. Davila**, None; **Frankie Myers**, CellScope Retina (P); **Clay Reber**, CellScope Retina (P); **David C. Musch**, None; **Todd P. Margolis**, CellScope (P); **Daniel Fletcher**, CellScope Retina (P); **Maria A. Woodward**, None; **Yannis M. Paulus**, None

Support: University of Michigan Center for Entrepreneurship Dean's Engineering Translational Prototype Research Fund; University of Michigan Translational Research and Commercialization for Life Sciences Grant # N021025, and University of Michigan Department of Ophthalmology and Visual Sciences department support

Program Number: 660 **Poster Board Number:** B0407
Presentation Time: 3:15 PM–5:00 PM
The Benefits of Real Time Pupil Tracking on the Quality of the B-Scan

Simon C. Stock[1, 2], Sophie Kubach[1], Patricia Sha[1], Jochen Straub[1], Wilhelm Stork[2]. [1]R&D, Carl Zeiss Meditec, Inc., Dublin, CA; [2]Institute for Information Processing Technologies (ITIV), Karlsruhe Institute of Technology, Karlsruhe, Germany.

Purpose: In retinal imaging eye instruments, such as Optical Coherence Tomography (OCT) imaging, the pupil entry point is crucial for the quality of the scan. This is of particular importance for subjects with small pupils (less than 2 mm) or those with cataracts. The purpose of this study is to demonstrate the accuracy of a pupil tracking algorithm that could be used to maintain a consistent pupil entry point in an OCT instrument.

Methods: A real-time pupil tracking algorithm was tested offline on a set of iris images previously acquired on a CIRRUS™ HD-OCT 5000 (ZEISS, Dublin, CA) instrument. The data set consists of n=295 images with various levels of image quality. In order to rate and validate the pupil tracking algorithm, we first defined the ground truth manually for the pupil centers and boundaries (see Figure 1). The pupil tracking algorithm follows a gradient approach and adds further filtering to better exclude artifacts such as those caused by the eye lid and reflections. The output of the algorithm is a least-squares and RANSAC fitted ellipse (see Figure 1).

Results: The pupil detection algorithm is able to determine the center of the pupil with a mean accuracy of 7.65 pixels or 230 µm (calculated over the 295 individual test cases), where the accuracy is defined by the ground truth.
The study was performed on 3 subjects known to have a small pupil which makes the quality of the B-Scan more sensitive to misalignments. In Figure 2 it can be seen that a misaligned B-Scan (B) has a reduced signal to noise ratio in comparison with the optimal alignment (A).

Conclusions: We demonstrated the benefit pupil detection has on the quality of the B-Scan. The proposed method has the potential to be implemented along with a closed loop control system for pupil alignment and tracking. A workflow based on pupil tracking may improve the measurement repeatability on OCT instruments and reduce the interaction between the operator and the instrument.

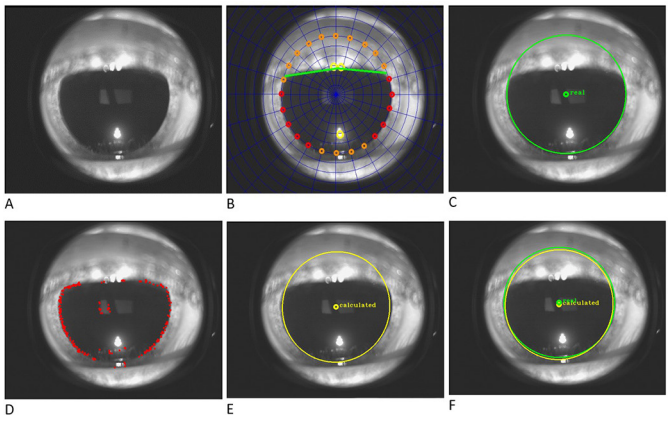

Figure 1: A: Original Iris Image. B: Ground Truth. C: Ground truth for pupil boundaries and pupil center. D: Output of the algorithm: Feature points on pupil. E: Fitted ellipse. F: Comparison of ground truth and algorithm.

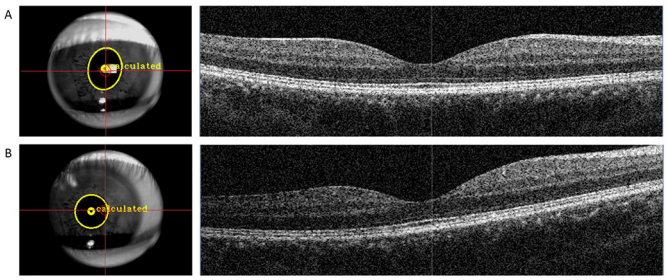

Figure 2: Difference in B-Scan quality between a correctly centered and misaligned pupil. The misaligned pupil causes a reduction of the signal to noise ratio as it can be seen on the left part of the B-Scan.

Commercial Relationships: Simon C. Stock, Carl Zeiss Meditec, Inc. (C); **Sophie Kubach**, Carl Zeiss Meditec, Inc. (E); **Patricia Sha**, Carl Zeiss Meditec, Inc. (C); **Jochen Straub**, Carl Zeiss Meditec, Inc. (E); **Wilhelm Stork**, None

Program Number: 661 **Poster Board Number:** B0408
Presentation Time: 3:15 PM–5:00 PM
Retinal Pigment Epithelium Layer Segmentation Accuracy on Widefield High Resolution Optical Coherence Tomography Cubes

Sophie Kubach[1], Warren Lewis[2], Giovanni Gregori[3], Philip J. Rosenfeld[3]. [1]R&D, Carl Zeiss Meditec, Inc, Dublin, CA; [2]Bayside Photonics, Inc., Yellow Springs, OH; [3]Bascom Palmer Eye Institute, Miami, FL.

Purpose: Swept source optical coherence tomography offers several advantages including faster scan rates and deeper imaging into the choroid. While these two parameters are used to expand the field of view and increase the density of the scan, the amount of data that needs to be processed increases rapidly. The purpose of this study is to determine an acceptable trade-off between segmentation processing time and the quality of segmentation for the retinal pigment epithelium (RPE).

Methods: METHODS:
Three eyes with dry age-related macular degeneration (AMD) were imaged on PLEX™ Elite 9000 (ZEISS, Dublin, CA). For each eye, a 12mm x 12 mm cube consisting of 1024 B-scans and 1024 A-scans per B-scan was acquired and processed for segmentation as acquired and after down-sampling the acquired cube by a factor of 2 and 4 (denoted as x2 and x4); which resulted in 22 um and 44 um resolutions respectively. The quality of segmentation was compared

by reviewing the RPE segmentation overlaid on the B-scans in the presence of drusen and by analyzing morphologic features present on a slab defined from the RPE to the Bruch's membrane.

Results: Image 1 shows the original RPE segmentation and segmentation produced by down-sampling the cube by factors of 2 and 4 and overlaid on a B-scan with evident irregularities in the RPE. The down-sampling factor of 2 method remains accurate in segmenting lesions affecting the RPE with only minor differences in some regions. The x4 down-sampling method produces gross segmentation errors that underestimates the size of the lesions. The elevated RPE profile produced from the original segmentation and from the two down-sampling methods are shown on images 2A, 2B, and 2C. If we ignore the artifacts from the difference in segmenting the optic disc and concentrate on the macular region where drusen are present, the root mean square value of the difference in RPE elevation from the original RPE elevation is 6 um and 12 um for the x2 and x4 down-sampling method respectively.

Conclusions: By comparing the segmentations overlaid on the B-scans, we found that the x2 down-sampling method remains accurate in segmenting the RPE. This method speeds up the algorithm by a factor of 4 and represents a good trade-off between quality of the RPE segmentation and processing time.

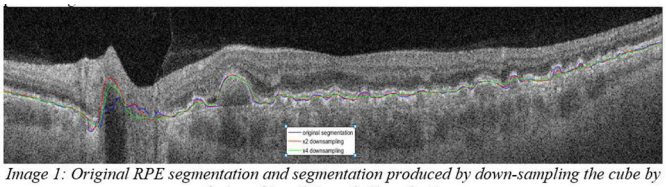

Image 1: Original RPE segmentation and segmentation produced by down-sampling the cube by a factor of 2 and 4 overlaid on the B-scan

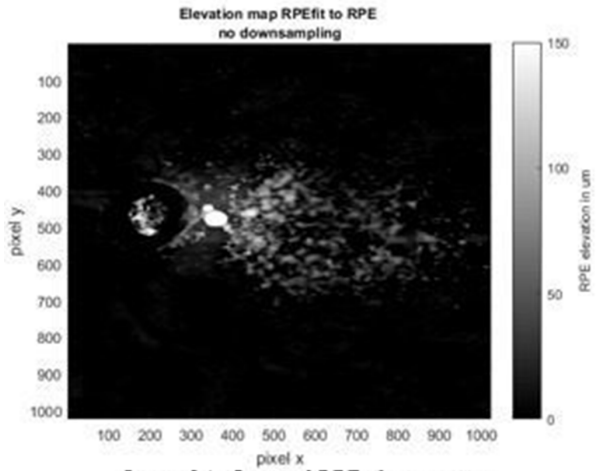

Image 2A: Original RPE elevation map

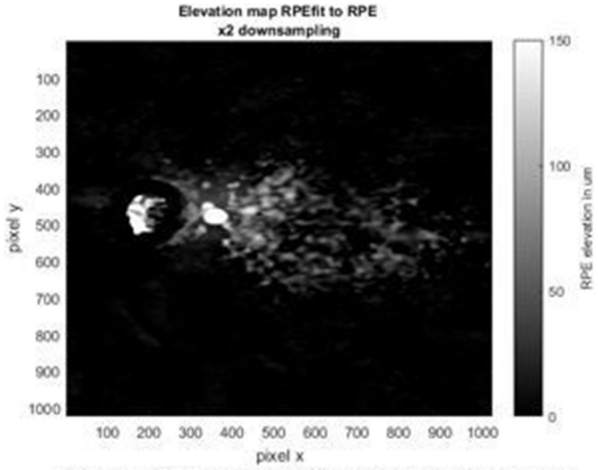

Image 2B: RPE elevation map from down-sampling x2

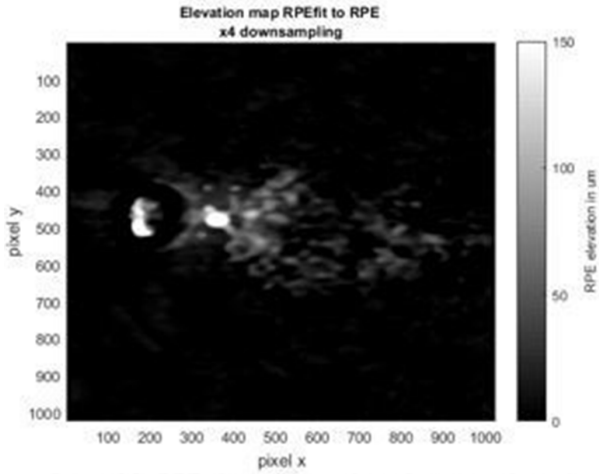

Image 2C: RPE elevation map from down-sampling x4

Commercial Relationships: Sophie Kubach; **Warren Lewis**, Bayside Photonics, Inc. (C); **Giovanni Gregori**, Bascom Palmer Eye Institute (F); **Philip J. Rosenfeld**, Bascom Palmer Eye Institute (F)

Program Number: 662 **Poster Board Number:** B0409
Presentation Time: 3:15 PM–5:00 PM

Repeatability of ellipsoid zone width measurements in retinitis pigmentosa using longitudinal reflectivity profiles

Margaret R. Strampe[1, 2], Alison L. Huckenpahler[3], Brian P. Higgins[1], Kimberly E. Stepien[4], Joseph Carroll[1, 3]. [1]Ophthalmology & Visual Sciences, Medical College of Wisconsin, Milwaukee, WI; [2]University of Minnesota Medical School, Minneapolis, MN; [3]Cell Biology, Neurobiology, and Anatomy, Medical College of Wisconsin, Milwaukee, WI; [4]Ophthalmology & Visual Sciences, University of Wisconsin-Madison, Madison, WI.

Purpose: Ellipsoid zone (EZ) width has been established as a structural marker for boundaries of the visual field in retinitis pigmentosa (RP).[1] Central to the use of EZ width as an objective measure of disease progression is establishing its repeatability. Here we examined the intra-observer repeatability of measurements of EZ width in patients with RP using longitudinal reflectivity profiles (LRPs).[2]

Methods: We retrospectively examined Bioptigen OCT scans from 15 subjects (1 simplex RP, 5 adRP, 3 arRP, 2 XLRP, 2 USH1, 2 USH2). Mean ± standard deviation (SD) age was 42.7 ± 22.4 years (range = 7-8 years; 8 male, 7 female). The eye with better image quality was analyzed. Nominal scan lengths were 6, 7, or 10 mm, and the lateral scale of each scan was calculated based on estimated lateral magnification from axial length measurements. LRPs were generated from OCT line scans, and peaks corresponding to the external limiting membrane, EZ, interdigitation zone, and retinal pigment epithelium were manually identified in ImageJ (NIH, Bethesda, MD) by a single observer. The nasal and temporal locations at which the EZ peak disappeared were considered the boundaries of the EZ band. This process was repeated with the same observer masked to previous measurements. Estimates of EZ width were obtained for both horizontal (HW) and vertical (VW) scans.

Results: Mean ± SD EZ width was not significantly different between HW (3179 ± 1399 μm) and VW (2459 ± 1279 μm) (p=0.1064), though HW was greater than VW for all subjects, ranging from 139-1453 μm difference. We observed excellent repeatability with ICCs of 0.994 (95% CI = 0.988-1.00) for HW and 0.998 (95% CI = 0.996-1.00) for VW. The mean test-retest difference was 76.4 ± 94.5 μm. Measurement error was 166.7 μm (~5.9%), calculated from the within-subject SD.

Conclusions: Our observation of greater HW than VW is consistent with previous observations in RP.[3-5] EZ width can be measured using LRPs with excellent repeatability. The test-retest differences observed here are comparable to other methods.[4,5] One advantage of using LRPs is that the method does not rely on layer segmentation and can facilitate measurement of band thickness and intensity.

[1]Hood PMID:21559123
[2]Huang PMID:9804149
[3]Hariri PMID:27031504
[4]Cai PMID:25342618
[5]Ramachandran PMID:24349883

Commercial Relationships: **Margaret R. Strampe**, None; **Alison L. Huckenpahler**, None; **Brian P. Higgins**, None; **Kimberly E. Stepien**, None; **Joseph Carroll**, None
Support: T32GM080202, UL1TR001436, TL1TR001437, R01EY017607, P30EY001931

Program Number: 663 **Poster Board Number:** B0410
Presentation Time: 3:15 PM–5:00 PM

The utility of the opacity suppression (OS) filter tool with automated retinal analysis software and manual reading for detection of DR in DM Type 1

Sumana Kommana, Nicole Mendez, Lesley Wu, Pooja Padgaonkar, Bernard Szirth, Albert S. Khouri. Ophthalmology, Rutgers New Jersey Medical School, Newark, NJ.

Purpose: To assess the utility of the OS filter with automated software and manual reading for detection of DR in Type 1 DM.

Methods: We collected 20 images obtained over 10 visits from a 21 y/o Hispanic male with type 1 DM for 17 years. Color fundus images of both eyes were captured in non-mydriatic mode at a 45° angle and a flash setting of 100 watt second using a Canon CR-DGi (12 Mp) and CR2 Plus AF retinal camera with an 18 Mp CMOS censor. The images were subsequently enhanced with the OS filter, a novel technique by Canon USA which entails of color correction by emphasizing blue color and contrast adjustment by increasing edge sharpness. The 2 sets of images were digitally analyzed using EyeArt™ (Eyenuk, Inc., Los Angeles, CA) automated DR screening software, which recommends "refer" when it detects moderate NPDR or higher on the ICDR scale or "no refer" otherwise. It also reports DR severity and offers a score from 0-5, with higher scores signifying higher DR severity levels. Both sets of images were also manually analyzed for total number of lesions, further differentiated by type: dot, flame, and intraretinal microvascular abnormalities (IrMAs). A board certified ophthalmologist reviewed each set of images. An analysis comparing the impact of the OS on the detection of DR in automated and manual screening is reported.

Results: Software analysis of the original and enhanced images is detailed in Table 1. DR severity score did show variation between the two sets of images, however OS did not change management as referral was recommended in 10/10 encounters with both sets of images. Manual analysis of both sets of images is detailed in Table 2. OS increased visibility of dot hemorrhages but had limited effect on visibility of flame hemorrhages and IRMAs.

Conclusions: The OS filter tool significantly improved image quality, having the most notable effect on manual reading as dot hemorrhages had increased visibility. The filter showed limited benefit with automated analysis as there was some variation in DR severity scores but overall management (refer vs no refer) did not change. A limitation is the presence of a retinal reflex, found in young eyes, that could lessen the filter's utility. Future studies will assess the OS tool's use in assessing DR in type 2 DM in a greater age distribution.

Original Images

EyeArt input data			EyeArt output data		
EncounterID	OD image	OS image	ScreeningOutcome	DRSeverityOutcome	DRSeverityScore
e01	1-July11_2013OD.jpg	1-July11_2013OS.jpg	Recommended refer	Possibly Moderate NPDR	2.02845
e02	2-July8_2015OD.PNG	2-July8_2015OS.jpeg	Recommended refer	Possibly Proliferative DR	4.29338
e03	3-Sept3_2015OD.JPG	3-Sept3_2015OS.JPG	Recommended refer	Possibly Proliferative DR	4.22344
e04	4-Oct15_2015OD.JPG	4-Oct15_2015OS.JPG	Recommended refer	Possibly Severe NPDR	3.68233
e05	5-Nov12_2015OD.JPG	5-Nov12_2015OS.JPG	Recommended refer	Possibly Severe NPDR	3.82649
e06	6-Dec10_2015OD.JPG	6-Dec10_2015OS.JPG	Recommended refer	Possibly Severe NPDR	3.58475
e07	7-Dec22_2015OD.JPG	7-Dec22_2015OS.JPG	Recommended refer	Possibly Severe NPDR	3.62848
e08	8-Jan12_2016OD.JPG	8-Jan12_2016OS.JPG	Recommended refer	Possibly Severe NPDR	3.46515
e09	9-Feb22_2016OD.JPG	9-Feb22_2016OS.JPG	Recommended refer	Possibly Severe NPDR	3.22128
e10	10-July7_2016OD.JPG	10-July7_2016OS.JPG	Recommended refer	Possibly Moderate NPDR	2.09185

Opacity Suppression Images

EyeArt input data			EyeArt output data		
EncounterID	OD image	OS image	ScreeningOutcome	DRSeverityOutcome	DRSeverityScore
e01	1-OPS July11_2013OD.jpg	1-OPS July11_2013OS.jpg	Recommended refer	Possibly Moderate NPDR	2.0099
e02	2-OPS July8_2015OD.jpg	2-OPS July8_2015OS.jpg	Recommended refer	Possibly Severe NPDR	3.43533
e03	3-OPS Sept3_2015 OD.jpg	3-OPS Sept3_2015 OS.jpg	Recommended refer	Possibly Proliferative DR	4.00085
e04	4-OPS Oct15_2015 OD.jpg	4-OPS Oct15_2015 OS.jpg	Recommended refer	Possibly Moderate NPDR	2.85559
e05	5-OPS Nov12_2015 OD.jpg	5-OPS Nov12_2015 OS.jpg	Recommended refer	Possibly Severe NPDR	3.2908
e06	6-OPS Dec10_2015OD.jpg	6-OPS Dec10_2015OS.jpg	Recommended refer	Possibly Severe NPDR	3.22485
e07	7-OPS Dec21_2015 OD.jpg	7-OPS Dec21_2015 OS.jpg	Recommended refer	Possibly Severe NPDR	3.46609
e08	8-OPS Jan12_2016 OD.jpg	8-OPS Jan12_ 2016 OS.jpg	Recommended refer	Possibly Severe NPDR	3.11737
e09	9-OPS Feb22_2016 OD.jpg	9-OPS Feb22_2106 OS.jpg	Recommended refer	Possibly Moderate NPDR	2.74719
e10	10-OPS July7_2016 OD.jpg	10-OPS July7_2016 OS.jpg	Recommended refer	Possibly Moderate NPDR	2.06275

Table 1: EyeArt Analysis

Left Eye	July 11, 2013		July 8, 2015		Sept 3, 2015		Oct 15, 2015		Nov 12, 2015		Dec 10, 2015		Dec 21, 2015		Jan 12, 2016		Feb 22, 2016		July 7, 2016	
		OS		OS		OS		OS		OS		OS		OS		OS		OS		OS
Dot Hemes	2	9	221	255	77	82	51	66	39	44	22	28	22	26	18	20	11	13	0	2
Flame Hemes	0	0	38	41	2	2	2	2	2	2	1	1	4	4	2	2	0	0	0	0
IrMAs	1	1	12	12	13	13	9	9	4	4	3	3	2	2	2	2	1	1	0	0
ICDR Severity Score	Moderate		Severe		Severe		Severe		Severe		Severe		Severe		Severe		Severe		None /Moderate	
Right Eye	July 11, 2013		July 8, 2015		Sept 3, 2015		Oct 15, 2015		Nov 12, 2015		Dec 10, 2015		Dec 21, 2015		Jan 12, 2016		Feb 22, 2016		July 7, 2016	
		OS		OS		OS		OS		OS		OS		OS		OS		OS		OS
Dot Hemes	0	2	26	52	33	37	17	27	27	27	28	32	14	19	10	14	7	9	8	12
Flame Hemes	0	0	75	85	21	22	1	1	0	0	1	1	1	1	1	1	1	1	0	0
IrMAs	0	0	7	7	12	12	12	10	11	10	8	8	8	8	4	4	4	3	0	0
ICDR Severity Score	None/ Moderate		Severe		Severe		Severe		Severe		Severe		Severe		Severe		Severe		Moderate/ Severe	

Table 2: Manual Analysis

Commercial Relationships: Sumana Kommana; **Nicole Mendez**, None; **Lesley Wu**, None; **Pooja Padgaonkar**, None; **Bernard Szirth**, None; **Albert S. Khouri**, None

Program Number: 664 **Poster Board Number:** B0411
Presentation Time: 3:15 PM–5:00 PM

Computed tomography imaging of periocular metallic foreign bodies can be improved by artifact reduction software

Keirnan Willett[1], Mike Sheng[2], John Woo[2], Thomasine Gorry[1]. [1]Ophthalmology, University of Pennsylvania, Philadelphia, PA; [2]Radiology, University of Pennsylvania, Philadelphia, PA.

Purpose: Computed tomography (CT) is the standard of care for assessment of ocular and orbital trauma. In cases of retained metallic foreign bodies, streak artifacts can significantly degrade CT image quality. Methods have been used to reduce metallic streak artifacts elsewhere in the body but their utility in the eye and orbit has not yet been reported.
Methods: Ten cases of retained periocular metallic foreign bodies (FB) evaluated by CT scan were identified retrospectively from a large urban trauma center. Post-acquisition images were processed with a metal streak artifact reduction software (MAR) called metal deletion technology. The change in the severity of the metal streak artifact was assessed objectively by 1) the size of the artifact and 2) the standard deviation of pixel intensities along a path surrounding the foreign body. For subjective assessment, radiologists (4), ophthalmologists (4) and oculoplastic specialists (3) used a Likert scale to grade images on 6 clinically relevant criteria.
Results: Average grading of "severity of metal streak artifact" and overall "confidence in prognosis" was improved after MAR in all ten cases ($p<0.001$). The standard deviation of pixel intensity for a path surrounding the FB was decreased in all cases ($p<0.001$) and area of streak artifact was reduced in all cases ($p<0.001$). The improvement in the confidence of assessment for specific criteria and structures was variable for individual cases, including – identification of all FB, assessment extra ocular muscles, assessment of optic nerve, assessment for globe rupture and assessment for orbital fracture.
Conclusions: Metal artifact reduction algorithms in computed tomography have potential benefits in improving diagnostic accuracy and confidence in emergent periocular trauma cases.

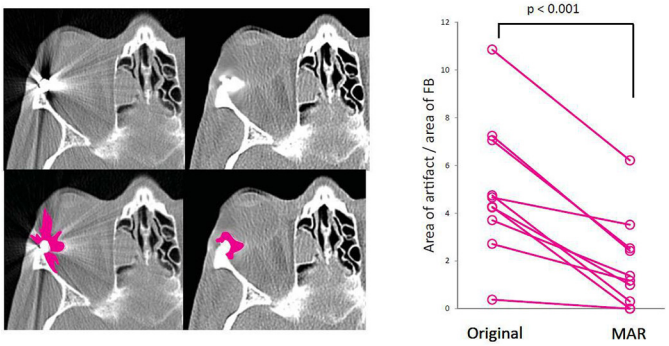

Example of CT streak artifact from metallic foreign body before (left) and after (right) metal artifact reduction (MAR). The area of the artifact was reduced after MAR in all ten cases studied (plot) ($p<0.001$).

Commercial Relationships: Keirnan Willett, None; **Mike Sheng**; **John Woo**, None; **Thomasine Gorry**, None

Program Number: 665 **Poster Board Number:** B0412
Presentation Time: 3:15 PM–5:00 PM

A New Scale (Penn Scale) for Measuring Bulbar Conjunctival Redness from Digital Photographs

Ilaria Macchi[3], Vatinee Y. Bunya[3], Mina Massaro-Giordano[3], Yuanjie Zheng[2], Min Chen[4], Maureen G. Maguire[1], Richard A. Stone[1], Eli Smith[1], Jim Gee[1], Ebenezer Daniel[1]. [1]University di Pennsylvania, Philadelphia, PA; [2]School of Information Science and Engineering at Shandong Normal University, Jinan, China; [3]Scheie Eye Institute, Philadelphia, PA; [4]Radiology, University of Pennsylvania, Philadelphia, PA.

Purpose: Current scales for measuring bulbar conjunctival redness have limitations when used with digital photographs. This study sought to develop a scale suited for digital images (Penn Scale) and compare the grading results from it to those using the VBR (Validated Bulbar Redness) scale.
Methods: A digital image database of 4889 color corrected nasal and temporal images of eyes with varying degrees of drug-induced bulbar conjunctival redness was reviewed to identify the least (score 1) and most severe redness (score 10), as well as 8 intermediate levels of redness. These 20 digital images, ten each of nasal and temporal, comprise the Penn scale, the linearity of which was assessed with an established image processing algorithm. 100 randomly selected images from the database were assessed by 3 professional non-physician graders using the Penn scale and the VBR scale. Agreement among graders was assessed with Kappa statistics using Cicchetti-Allison weights. The ease of use of the two scales was also documented.
Results: The Penn scale showed an almost perfect linearity of redness (Figure 1). The weighted Kappas for agreement between any two graders ranged from 0.57 to 0.73 for the Penn scale and from 0.38 to 0.66 for the VBR scale (Table 1). Among all three graders the weighted Kappa was 0.39 for the Penn scale and 0.14 for the VBR scale. In contrast to the VBR scale, the Penn scale allowed direct comparison of digital to digital images, could be used in a dimly lit environment conducive for evaluating digital images, had scaled bulbar conjunctival images for both temporal and nasal sides, and permitted reference scale images to be magnified to the same size as the images to be graded.
Conclusions: The Penn scale demonstrated several advantages over the VBR scale for the subjective measurement of bulbar redness from digital images.

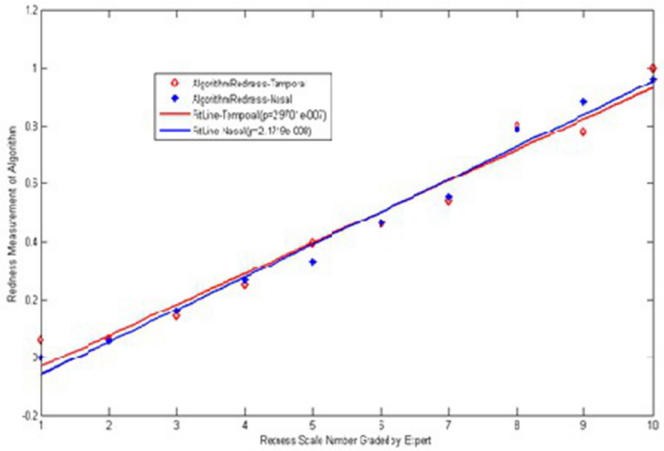

Scale	Exact % agreement (95% CI)	Weighted Kappa* (95% CI)
Penn		
Grader 1 vs Grader 3	68% (58%, 77%)	0.73 (0.65, 0.82)
Grader 1 vs Grader 2	52% (42%, 62%)	0.60 (0.48, 0.71)
Grader 3 vs Grader 2	48% (38%, 58%)	0.57 (0.46, 0.68)
Among 3 graders	38% (28%, 48%)	0.39 (0.27, 0.51)
VBR		
Grader 1 vs Grader 3	18% (11%, 27%)	0.38 (0.29, 0.47)
Grader 1 vs Grader 2	55% (45%, 65%)	0.66 (0.57, 0.75)
Grader 3 vs Grader 2	25% (17%, 35%)	0.46 (0.36, 0.56)
Among 3 graders	7% (3%, 14%)	0.14 (0.08, 0.20)
Difference (Penn vs VBR)		
Grader 1 vs Grader 3	50% (38%, 62%)	0.35
Grader 1 vs Grader 2	-3% (-17%, 11%)	0.06
Grader 3 vs Grader 2	23% (10%, 36%)	0.11
Among 3 graders	31% (20%, 42%)	0.25

Commercial Relationships: Ilaria Macchi, None; **Vatinee Y. Bunya**, NEI R01EY026972 (F), Shier (C), Bausch & Lomb (F); **Mina Massaro-Giordano**, The Eyelid Photography Protocol is copyright-protected by the University of Pennsylvania. (P); **Yuanjie Zheng**, Taishan Scholar Program of Shandong Province in China (TSHW201502038) (F), Natural Science Foundation of Shandong Province in China (ZR2014FM001) (F), Natural Science Foundation of China (NSFC) (61572300) (F); **Min Chen**, None; **Maureen G. Maguire**, The Eyelid Photography Protocol is copyright-protected by the University of Pennsylvania. (P); **Richard A. Stone**, The Eyelid Photography Protocol is copyright-protected by the University of Pennsylvania. (P); **Eli Smith**, None; **Jim Gee**, None; **Ebenezer Daniel**, The Eyelid Photography Protocol is copyright-protected by the University of Pennsylvania. (P)

Program Number: 666 **Poster Board Number:** B0413
Presentation Time: 3:15 PM–5:00 PM
Automatic segmentation of nine layer boundaries in OCT images using convolutional neural networks and graph search
Leyuan Fang[1, 2], Chong Wang[2], David Cunefare[1], Robyn H. Guymer[3], Sina Farsiu[1]. [1]Biomedical Engineering, Duke University, Durham, NC; [2]College of Electrical and Information Engineering, Hunan University, Changsha, China; [3]Centre for Eye Research, Australia University of Melbourne, Melbourne, VIC, Australia.
Purpose: To develop an automatic method for the segmentation of nine layer boundaries on optical coherence tomography (OCT) images of dry age-related macular degeneration (AMD).
Methods: We utilized convolutional neural networks (CNN) to extract features of specific retinal layer boundaries and trained a corresponding classifier to delineate eight layers on Spectralis OCT images. Specifically, in the training step, we extracted patches (of size 33×33 pixels) centered on manually segmented layer boundaries from 171 OCT B-scans from 57 volumes. Then, we trained a CNN on the extracted patches. In the testing step, we used 60 OCT volumes (each volume includes 48 to 49 B-scans) from 20 AMD eyes (imaged at three time points over a 12-month period at 6-month intervals), which were separate from the subjects used for training the CNN. We decomposed the test OCT B-scans into over-lapping patches (of size 33×33) and applied the trained CNN classifier to obtain layer boundary labels and probabilities in each patch. Finally, we created a graph using the learned boundary probabilities and applied a Dijsktra based graph-search algorithm to estimate the location of the layer boundaries. For validation, the average difference in layer thickness between the automatic segmentation and a manual segmentation by an expert grader was calculated for each layer of each B-scan. The absolute mean difference and standard deviation across all B-scans was then computed.
Results: We tested our CNN/graph layer method on 60 OCT volumes. The average (standard deviation) retinal layer thickness differences between our method and one expert manual grader are: NFL 0.57(0.58); GCL+IPL 0.46(0.67); INL 0.23(0.56); OPL 0.68(1.17); ONL 0.80(1.35); IS 0.16(0.29); OS 0.98(0.96); RPE 1.15(1.61); Total Retinal 1.26(1.25). Fig. 1 is an illustrative example of segmented layers using the proposed technique as compared to expert manual grading.
Conclusions: Our CNN/graph based layer method can automatically segment nine retinal layer boundaries in human AMD subjects with high accuracy. Since no disease specific assumptions are used in the design of the CNN algorithm, this technique can be adapted for other types of diseases.

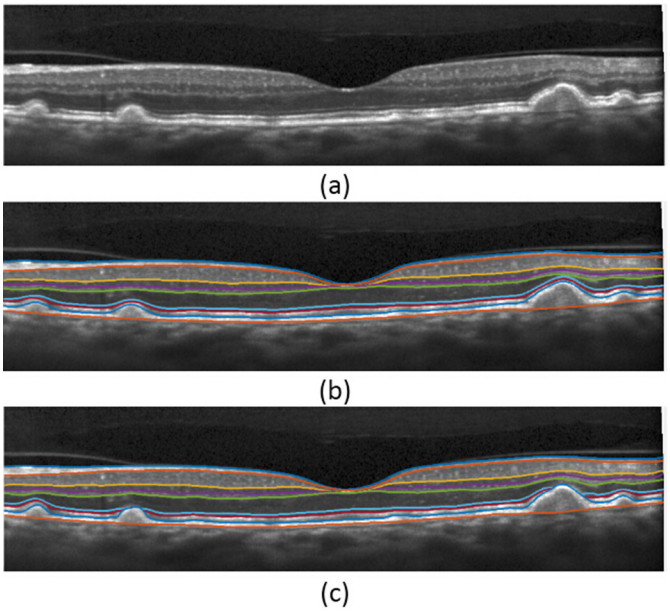

Fig. 1 Segmented retinal layer boundaries on a sample OCT image of an AMD eye with drusen. (a) Raw image; (b) proposed CNN/graph based segmentation; (c) manual segmentation.
Commercial Relationships: Leyuan Fang, Hunan University (E), Duke University (F); **Chong Wang**, None; **David Cunefare**, Novartis (C), Roche/Genentech (C), Bayer (C); **Robyn H. Guymer**, University of Melbourne (E); **Sina Farsiu**, Duke University (P), Duke University (E), Duke University (F)
Support: NIH Grant R01 EY022691

Program Number: 667 **Poster Board Number:** B0414
Presentation Time: 3:15 PM–5:00 PM
Novel ImageJ Analysis Technique for the Quantitation of Apoptotic Hotspots
Tyler N. Heisler-Taylor[1, 2], Anchshana Haridas[1], Bongsu Kim[1], Rania Kusibati[1], Colleen M. Cebulla[1]. [1]Havener Eye Institute, Ophthalmology and Visual Science, The Ohio State University, Columbus, OH; [2]Department of Biomedical Engineering, The Ohio State University, Columbus, OH.
Purpose: To present a novel, semi-automated method to quantitate TUNEL-positive cells in high intensity 'hotspot' regions within retinal cross sections. Previously established automated methods have not been able to sufficiently measure these high intensity or saturated regions.
Methods: Retinal detachments (RD) were induced in murine eyes with subretinal hyaluronic acid injection under an IACUC-approved protocol. Mice were sacrificed at day 3 and the eyes were harvested

and enucleated for IHC staining. For apoptosis quantification in retinal frozen sections, fluorescence images of TUNEL-positive retinal cells (568nm) and DAPI nuclear labeling (461nm) in detached or corresponding control areas were taken with a 20x objective lens with identical illumination and exposure times. Images were then analyzed and compared with two techniques: 1) the RETINA Analysis Toolkit macro for ImageJ and 2) a semi-automatic multichannel color thresholding technique. The multichannel thresholding utilizes the color threshold technique in ImageJ by thresholding the RGB channels allowing for the selection of both DAPI and TUNEL positive cell nuclei simultaneously. Student's t-test was used for statistical analysis.

Results: Analysis of the ratio of TUNEL-positive cells captured by the Toolkit macro over those captured through multichannel thresholding in TUNEL 'hotspot' regions resulted in a significant difference (0.678 ± 0.229 macro/multi ratio vs. 1.0 ± 0.0 multi/multi ratio, p = 0.0183) while 'normal' TUNEL regions were indistinguishable (1.048 ± 0.532 macro/multi vs. 1.0 ± 0.0 multi/multi, p = 0.8340).

Conclusions: The method presented above to analyze regions of intense apoptosis has significantly improved accuracy compared to previously established automated systems by also accounting for the nuclear stain when counting apoptotic cells. Incorporating this new technique as an option within the analysis macro would facilitate analysis of nuclear hotspot regions.

Commercial Relationships: Tyler N. Heisler-Taylor, None; **Anchshana Haridas**, None; **Bongsu Kim**, None; **Rania Kusibati**, None; **Colleen M. Cebulla**, None

Support: NIH K08EY022672, P30 CA016058 (OSU-CCC Nucleic Acids Shared Resource), NCATS KL2TR001068. The content is solely the responsibility of the authors and does not necessarily represent the official views of the funding institutions. Additional funds were provided by the Ohio Lions Eye Research Foundation, Ophthalmology Fund #313310, and the Patti Blow Fund

Program Number: 668 **Poster Board Number:** B0415
Presentation Time: 3:15 PM–5:00 PM

Deep convolutional neural networks for automated OCT pathology recognition

Daniel B. Russakoff[1], Jonathan D. Oakley[1], Robert Chang[2].
[1]Voxeleron LLC, San Francisco, CA; [2]Byers Eye Institute at Stanford University, Stanford, CA.

Purpose: To use deep learning algorithms with and without automated segmentation-based preprocessing to classify individual optical coherence tomography (OCT) tomograms as "pathology present" or "pathology absent" based on expert labelling. Increasingly, deep learning approaches have shown success in automating image analysis of such data. Limitations include access to large labelled data and compute power, yet deep learning is now capable of matching expert clinicians, as demonstrated with diabetic retinopathy fundus photos [Gulshan 2016]. One way to overcome the data limitation is through intelligent preprocessing to help reduce model complexity and better address the bias-variance trade-off inherent in machine learning problems.

Methods: Macular OCT B-scans (Cirrus, Carl Zeiss Meditec, Inc) were used from 100 unique patients with 20 of those patients exhibiting evident pathology, including age-related macular degeneration (AMD), epiretinal membrane (ERM), and high myopia. Each was manually classified and split into 15,081 negative examples (controls), and 7,284 positive examples (pathology). For preprocessing, automated layer segmentation software (Orion, Voxeleron LLC) was used to crop each B-scan from the ILM to a fixed offset below Bruch's. The cropped B-scans were then resampled to a uniform size (Fig 1). The patients were randomly split into training (60%), validation (10%), and test (30%) sets. A deep convolutional neural network (CNN) using 8 layers was trained [2 convolutional layers, 2 pooling layers, 1 dropout layer, 2 hidden layers, and a soft-max regression layer]. Another CNN was trained on the same data but without the automated segmentation-based preprocessing.

Results: The accuracy of the system, as measured on the test set, is 98.8% with a sensitivity of 96.9% and a specificity of 99.8%. Without the automated segmentation-based preprocessing, the accuracy drops to 85.3% with a sensitivity of 78.7% and specificity of 88.6%.(Fig 2).

Conclusions: A deep CNN is capable of accurately differentiating pathological and normal OCT macular B-scans. With automated segmentation-based preprocessing, algorithm accuracy increased by 15.8% with improved sensitivity and specificity.

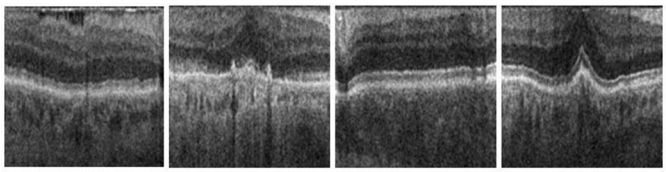

Fig 1. Example preprocessed input images (from l to r): ERM, AMD, and two "pathology absent" cases.

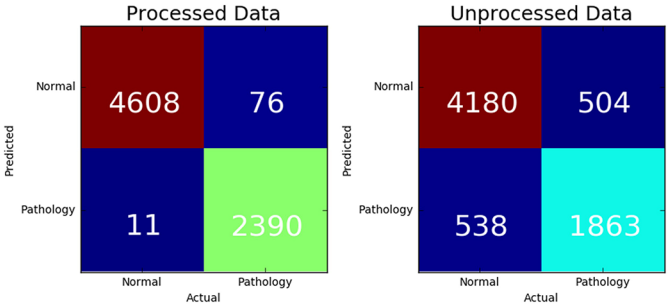

Fig 2. Confusion matrices with (left) and without (right) the automated segmentation-based preprocessing.

Commercial Relationships: Daniel B. Russakoff, Voxeleron (P), Voxeleron (E); **Jonathan D. Oakley**, Voxeleron (P), Voxeleron (E); **Robert Chang**, None

Program Number: 669 **Poster Board Number:** B0416
Presentation Time: 3:15 PM–5:00 PM

Automated Segmentation of Retinal Layers for Optic Nerve Head Centered OCT Images

Xinjian Chen[2], Enting Gao[2], Fei Shi[2], Weifang Zhu[2], Haoyu Chen[1].
[1]Joint Shantou International Eye Center, Shantou University and the Chinese University of Hong Kong, Shantou, China; [2]School of Electronics and Information Engineering, Soochow University, Suzhou, China.

Purpose: Optical coherence tomography(OCT), being a noninvasive imaging modality, has begun to find vast use in the diagnosis and management of ocular diseases. However, due to speckle noise and irregularly shaped morphological features such as optic never head(ONH), accurate segmentation of individual retinal layers is difficult.

Methods: 11 normal subjects (6 used as training set, 5 used as testing set) were included and underwent Optic Nerve Head centered SD-OCT (Topcon 3D-OCT 2000, 512×128×885 voxels, 6mm×6mm×2.3mm). The proposed framework consists of two main steps: preprocessing and layer segmentation. In the preprocessing step, a curvature anisotropic diffusion filter was used to reduce the OCT speckle noise. Then the B-scans were flattened based on

surface 5 (Fig.1). Subsequently, during layer segmentation, First, the Active Appearance Models(AAM)[3] was built, and the surface 1, 2, 3, 4, 5, 6, 7 and the optic disc was detected. Second, a multi-resolution graph-search algorithm[1], is applied for the further precise segmentation. Finally, the rim region of the optic disc was detected by shape prior model on the projection image from surface 6 to surface 7. The rim region is masked out because the layers are hard to define in this region.

Results: The algorithm was tested against the ground truth which manually traced by two retinal specialists independently. The results are accordance with the ground truth well(Fig.2).

Conclusions: In this paper, we proposed an automated method for retinal layers segmentation in ONH centered 3-D OCT images, which addresses the challenges posed by the presence of the large blood vessels and the optic disc. The preliminary results show the feasibility and efficiency of the proposed method.

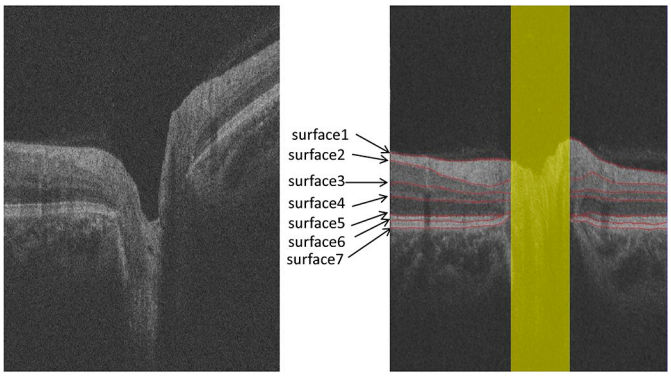

Fig.1 ONH centered OCT image of a normal eye and the 7 surfaces of the retinal layers. (a)original image (b) denoised and flattened image with segmentation result.

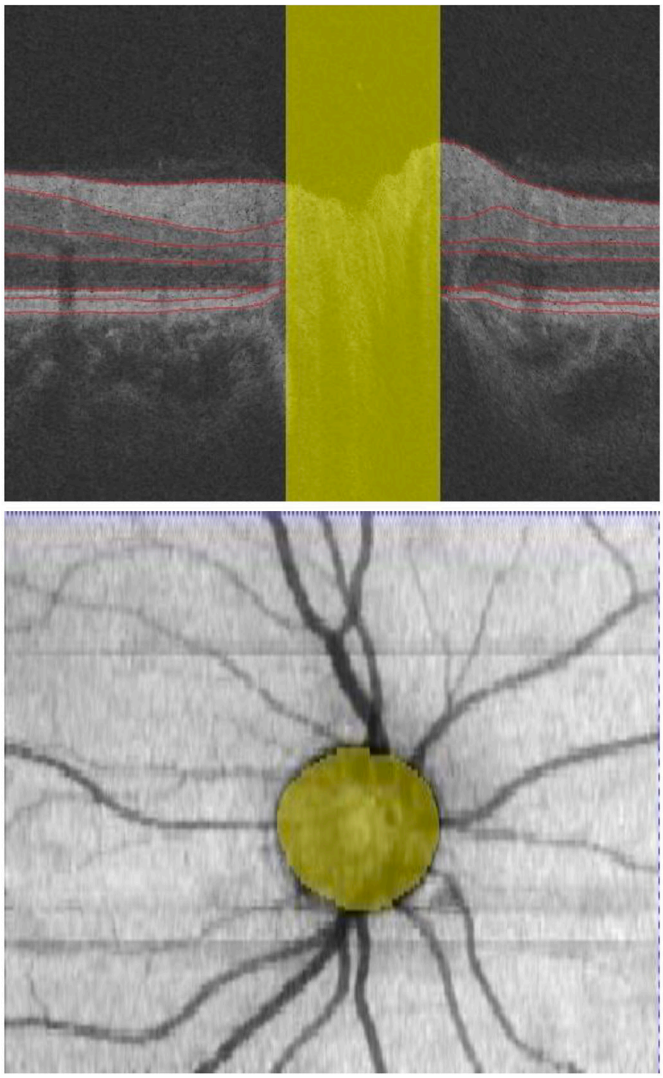

Fig.2 A central B-scan of a dataset with yellow indicating the rim region.

Commercial Relationships: Xinjian Chen; **Enting Gao**, None; **Fei Shi**, None; **Weifang Zhu**, None; **Haoyu Chen**, None
Support: This work was supported by the National Basic Research Program of China (973 Program) under Grant 2014CB748600, in part by the National Natural Science Foundation of China (NSFC) under Grant 81371629.

Program Number: 670 **Poster Board Number:** B0417
Presentation Time: 3:15 PM–5:00 PM

Automatic detection of the foveal center in optical coherence tomography

Bart Liefers[1], Freerk G. Venhuizen[1], Vivian Schreur[2], Bram van Ginneken[1], Carel C. Hoyng[2], Thomas Theelen[2], Clara I. Sanchez[1].
[1]Diagnostic Image Analysis Group, Radboudumc, Nijmegen, Netherlands; [2]Ophthalmology, Radboudumc, Nijmegen, Netherlands.

Purpose: To automatically detect the foveal center in optical coherence tomography (OCT) scans in order to obtain an accurate and reliable reference for the assessment of various structural biomarkers, even in the presence of large abnormalities and across different scanning protocols.

Methods: 1784 OCT scans were used for the development of the proposed automatic method: 1744 scans from the European Genetic Database (EUGENDA) acquired with a Heidelberg Spectralis HRA+OCT 1 scanner and 40 scans from a publicly available dataset [1] acquired with a Bioptigen scanner. Two independent sets, with different levels of age-related macular degeneration (AMD) were drawn from the same databases for evaluation: 100 scans from EUGENDA (Set A, 25 control patients and 25 for each of the AMD severity levels early, intermediate and advanced) and 100 scans from [1] (Set B, 50 control, 50 AMD).
A fully convolutional neural network based on stacked layers of dilated convolutions was trained to classify each pixel in a B-scan by assigning a probability of belonging to the fovea. The network was applied to every B-scan in the OCT volume, and the final foveal center was defined as the pixel with maximum assigned probability. An initial network was trained on the 1744 training scans from EUGENDA and optimized with the 40 training scans acquired with the Bioptigen scanner, to specialize for different levels of noise and contrast.
For all scans manual annotations were available as reference for evaluation. The foveal center was considered correctly identified if the distance between the prediction and the reference was less than the foveal radius, i.e. 750 µm.
Results: The foveal center was correctly detected in 95 OCT scans in Set A (24 control, 24 early, 25 intermediate, 22 advanced). The mean distance error was 63.7 µm with 81 detections inside a radius of 175 µm (the foveola) and 70 inside a radius of 75 µm (the umbo). In Set B, the foveal center was correctly identified in 96 OCT scans (49 control, 47 AMD). The mean distance error was 88.6 µm with 82 detections inside the foveola and 61 inside the umbo.
Conclusions: The proposed automatic method performed accurately for both healthy retinas and retinas affected by AMD. The method can be applied successfully to scans from different vendors, thus providing a reliable reference location for the assessment of structural biomarkers in OCT.
[1] http://people.duke.edu/~sf59/RPEDC_Ophth_2013_dataset.htm

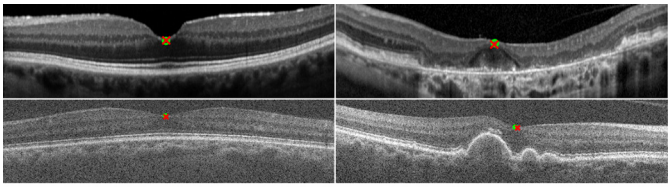

Figure 1. Example of predicted fovea position (red cross) and reference location (green circle). Top: control and advanced AMD case in Set A (distance 4 µm and 11 µm), bottom: control and AMD case in Set B (distance 11 µm and 47 µm).

Commercial Relationships: Bart Liefers, None; **Freerk G. Venhuizen**, None; **Vivian Schreur**, None; **Bram van Ginneken**, None; **Carel C. Hoyng**, None; **Thomas Theelen**, None; **Clara I. Sanchez**, None

Program Number: 671 **Poster Board Number:** B0418
Presentation Time: 3:15 PM–5:00 PM

Fully automated detection of hyperreflective foci in optical coherence tomography

Freerk G. Venhuizen[1, 3], Samuel Schaffhauser[1, 2], Vivian Schreur[3], Lebriz Altay[4], Bart Liefers[1, 3], Bram van Ginneken[1], Carel C. Hoyng[3], Thomas Theelen[3, 1], Eiko de Jong[3], Clara I. Sanchez[1, 3]. [1]Diagnostic Image Analysis Group, Radboudumc, Nijmegen, Netherlands; [2]Department of statistics, ETH Zürich, Zürich, Switzerland; [3]Department of ophthalmology, Radboudumc, Nijmegen, Netherlands; [4]Department of ophthalmology, Uniklinik Köln, Cologne, Germany.

Purpose: Diabetic macular edema (DME) is a retinal disorder characterized by a buildup of cystoidal fluid in the retina. The typical treatment consists of monthly intravitreal anti vascular endothelial growth factor (anti-VEGF) injections. However, the efficacy of this treatment varies strongly. Recent studies have indicated that the presence and number of hyperreflective foci can possibly be considered a prognostic biomarker for treatment response in DME. As the detection of foci is difficult and time-consuming manual foci quantification seems infeasible. We therefore developed a fully automated system capable of detecting and quantifying foci in optical coherence tomography (OCT) images.
Methods: 119 fovea centered B-scans obtained from 49 patients with DME were selected from a clinical database. The data was divided in a training set of 96 B-scans from 40 patients, and a test set containing 23 B-scans from 9 patients. A convolutional neural network (CNN) was developed to predict if an image pixel belongs to a hyperreflective focus by considering a small neighborhood around the pixel of interest. The CNN consists of 7 convolutional layers and 2 max pooling layers. After providing the system with enough training samples, the network automatically detects pixels with a high probability of being part of a hyperreflective focus. Connected detections are considered as a single detection. The obtained results were compared to manual annotations made by two experienced human graders in consensus for the central 3 mm surrounding the fovea. Hyperreflective foci were only annotated in the layers ranging from the inner plexiform layer (IPL) to the outer nuclear layer (ONL) as manual detection is challenging in the other layers. When a detection is overlapping with an annotated focus it is considered a true positive, otherwise it is counted as a false positive.
Results: In the independent test set a sensitivity of 0.83 was obtained. At this level of sensitivity, an average of 8.3 false positives per B-scan were detected. False positives were mainly caused by detections outside the selected range (IPL to ONL) and misdetections by the graders.
Conclusions: An image analysis algorithm for the automatic detection and quantification of hyperreflective foci in OCT B-scans was developed. The experiments show promising results to obtain quantitative foci based biomarkers that can be used for the prediction of treatment response in DME.

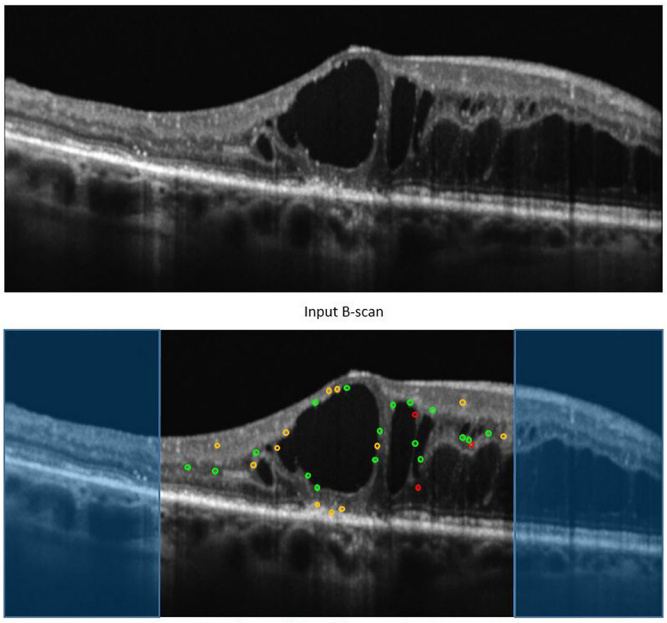

Commercial Relationships: Freerk G. Venhuizen; **Samuel Schaffhauser**, None; **Vivian Schreur**, None; **Lebriz Altay**, None; **Bart Liefers**, None; **Bram van Ginneken**, None; **Carel C. Hoyng**, None; **Thomas Theelen**, None; **Eiko de Jong**, None; **Clara I. Sanchez**, None

Program Number: 672 **Poster Board Number:** B0419
Presentation Time: 3:15 PM–5:00 PM
Retinal layer segmentation results differ between two generations of OCT devices

Beerend Winkelman[1, 6], Johanna Maria Colijn[1], Pieter W. Bonnemaijer[1], Fernanda Fujihara[1], Michael D. Abramoff[5, 3], Kristine E. Lee[4], Anthony S. Fairbanks[4], Stacy M. Meuer[4], Barbara E. Klein[4], Ronald Klein[4], Caroline Klaver[1, 2].
[1]Ophthalmology and Epidemiology, Erasmus MC, Rotterdam, Netherlands; [2]Ophthalmology, Radmoud UMC, Nijmegen, Netherlands; [3]Electrical and Computer Engineering, University of Iowa, Iowa City, IA; [4]Ophthalmology & Visual Sciences, University of Wisconsin, Madison, WI; [5]Stephen A. Wynn Institute for Vision Research, University of Iowa, Iowa City, IA; [6]Netherlands Institute for Neuroscience, Amsterdam, Netherlands.

Purpose: As spectral domain optical coherence tomography (SD-OCT) has become routine in clinical practice and research, and newer OCT devices are replacing first generation OCTs, it is essential to verify their output. We studied retinal layer thickness in healthy eyes of two comparable populations obtained with a first and a second generation OCT device. Additionally, we quantified differences in image quality between the two systems.
Methods: OCT data were obtained in the population-based Rotterdam Study (RS) with the TOPCON 3D-OCT1000 in 2007 (N=2785, age range: 47-96 yrs, mean 67.8; mean axial length 23.6mm; 56% ♀), and the TOPCON 3D-OCT2000 from 2008 onwards (N=1047, age range: 52-99 yrs, mean 68.7; mean axial length 23.6mm; 54% ♀). Scans were segmented with the validated Iowa Reference Algorithms 3.6 from the University of Iowa. A dataset in which eyes from each subject were scanned using both OCT systems was collected in the Beaver Dam Eye Study (University of Wisconsin). We studied differences in image quality between the two systems by comparing pixel intensity histograms using the variational distance metric.
Results: Systematic differences in average retinal layer thickness were observed between the two OCT systems. Sign and magnitude of this bias was layer dependent. The ganglion cell layer measured 32.5 ± 5.8 µm (mean±SD) with the OCT1000 and 36.2 ± 5.3 µm with the OCT2000, outer nuclear layer 87.2 ± 8.8 µm vs. 90.5 ± 8.2 µm, and the RPE measured 19.5 ± 1.6 µm vs. 16.9 ± 0.9 µm (all P<<0.001). Biases of similar magnitude were found in the BDES dataset, although layer thickness correlated relatively well between the two OCT systems. One explanation for the observed biases could be a difference in image quality between OCT devices. Comparing pixel intensity distributions indeed showed qualitative differences, with the second generation OCT system having less variance in dark region intensities and fatter high intensity tails. The retinal layer segmentation algorithm was robust to histogram rescaling and white noise image degrading procedures, applied to make image quality more uniform.
Conclusions: Replacing OCT devices with newer versions could introduce unexpected differences in the estimated thickness of retinal layers, even when segmentation is performed with the same robust algorithm. Automated thickness parameters should therefore be interpreted with caution when comparing data from different devices.
Commercial Relationships: Beerend Winkelman, None; **Johanna Maria Colijn**, None; **Pieter W. Bonnemaijer**, None; **Fernanda Fujihara**, None; **Michael D. Abramoff**, University of Iowa (P), IDx LLC (I), IDx LLC (C); **Kristine E. Lee**, None; **Anthony S. Fairbanks**, None; **Stacy M. Meuer**, None; **Barbara E. Klein**, None; **Ronald Klein**, None; **Caroline Klaver**, None
Support: NWO VICI 918.15.655, NIH Grants EY006594, EY019112, EY018853; the Department of Veterans Affairs; Alimera Inc, The Robert C. Watzke MD Professorship for Retina Research

Program Number: 673 **Poster Board Number:** B0420
Presentation Time: 3:15 PM–5:00 PM
Development of an Automated Segmentation Program to Assess Corneal Suturing Performance of Ophthalmology Residents Using 3D Printed Eye Models

Kelly L. Mote[1], Yu-Cherng Chang[1, 2], Florence Cabot[1, 3], Karam A. Alawa[1], Juan Silgado[1], Cornelis J. Rowaan[1], Madhura Joag[3], Sonia H. Yoo[3, 1], Carol Karp[3], Jean-Marie A. Parel[1, 4].
[1]Ophthalmic Biophysics Center, Bascom Palmer Eye Institute, University of Miami Miller School of Medicine, Miami, FL; [2]Department of Biomedical Engineering, University of Miami College of Engineering, Coral Gables, FL; [3]Anne Bates Leach Eye Hospital, Bascom Palmer Eye Institute, University of Miami Miller School of Medicine, Miami, FL; [4]Brien Holden Institute and Vision Cooperative Research Centre, Sydney, NSW, Australia.

Purpose: To develop an automated segmentation program to assess corneal suturing performance of ophthalmology residents using 3-D printed eye models and to compare the results with a semi-manual program.
Methods: After cornea suturing, on BIONIKO (Miami, FL) 3D printed eye models, by ophthalmology residents at Bascom Palmer Eye Institute, one eye model was randomly selected to be analyzed using our custom developed segmentation program. A digital camera (Canon EOS 40D DSLR & EF 100mm f/2.8 Macro Lens) was mounted on a microscope stand (AmScope TS130-LED, Irvine, CA) equipped with a centration adaptor holding the 3D printed eye model (Fig 1). Images were taken and imported into MATLAB (Mathworks, Natick, MA) to assess spacing and suture length. Images were

preprocessed using an averaging filter and edge detection methods were utilized to isolate sutures and points in the circle of trephination. Spacing was determined by finding the distance between intersection points of the circle of trephination and adjacent sutures. Suture length was determined by the distance between the endpoints of the suture (Fig 2). Results were compared to data obtained with the semi-manual segmentation program previously developed in the laboratory (Alawa K *et al*, IOVS 2016; 57(12):1224.).

Results: Segmentation of one image took 16.5 seconds with the automated segmentation program and 61.08 seconds with the semi-manual segmentation program. No significant difference was found between the automated and semi-manual programs regarding spacing and suture length. Mean spacing for the 8 sutures was 6.39±0.85 mm using the automated program and 6.33±1.04 mm using the semi-manual program (p=0.92). Mean suture length was 2.53±0.58 mm using the automated program and 2.77±0.47 mm using the semi-manual program (p=0.30).

Conclusions: The automated program was able to calculate the spacing and suture length and yielded results consistent with those obtained with the semi-manual program. Further refinements and calculation of radiality will be needed to optimize the objective assessment of corneal suturing performance provided by this novel automated program.

(A) Side view and (B) front view of the camera mount set up with a 3D printed eye model.

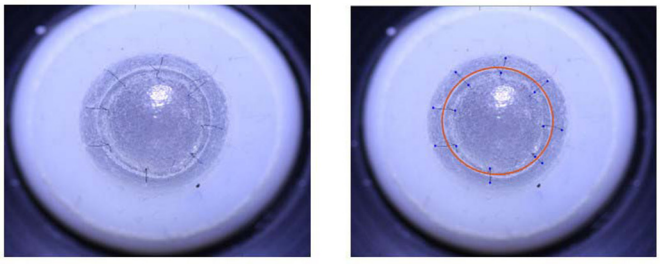

Original image (A) and a superimposed image (B) of 3D printed eye model with the endpoints and circle of trephination detected from the automated software.

Commercial Relationships: Kelly L. Mote, None; **Yu-Cherng Chang**, None; **Florence Cabot**, None; **Karam A. Alawa**, None; **Juan Silgado**, None; **Cornelis J. Rowaan**, None; **Madhura Joag**, None; **Sonia H. Yoo**, None; **Carol Karp**, None; **Jean-Marie A. Parel**, None

Support: The Ronald and Alicia Lepke Grant, The Lee and Claire Hager Grant, The Robert Baer Family Grant The Jimmy and Gaye Bryan Grant, The Richard Azar Family Grant (Institutional grants), The H. Scott Huizenga Grant (CLK), The Florida Lions Eye Bank Research Grant (MJ, CLK). The Florida Lions Eye Bank, Drs. KR Olsen and ME Hildebrandt, Drs. Raksha Urs and Aaron Furtado, The Henri and Flore Lesieur Foundation, Brien Holden Vision Institute (JMP), NIH Center Core Grant P30EY014801 and Research to Prevent Blindness unrestricted grant. Technical support and valuable input were provided by Heather Durkee, Mariela C. Aguilar, Priyanka Chhadva, Basil Williams, BPEI cornea fellows, Aida Grana, Madelin Serpa, Refractive Laser Center, managers and staff of the BPEI operating room.

Program Number: 674 **Poster Board Number:** B0421
Presentation Time: 3:15 PM–5:00 PM

Using a bot script to bulk export Spectralis OCT scan measurements into a clinical data warehouse

Karsten U. Kortuem[1, 2], Johannes Schiefelbein[1], Diana Jeliazkova[1], Pearse A. Keane[2], Christoph Kern[1], Michael Müller[1], Wolfgang J. Mayer[1], Siegfried Priglinger[1], Daniel Nasseh[3].
[1]Ophthalmology, Ludwig-Maximilians-University, Munich, Germany; [2]Moorfields Eye Hospital, London, United Kingdom; [3]Institute for Biometry and Epidemiology, Ludwig-Maximilians-University, Munich, Germany.

Purpose: As data warehouses with data from electronic health records (EHR) provide benefits for clinical research, adding information from imaging devices (e.g. retinal thickness from OCT) is useful. To overcome limitations in bulk exporting OCT measurements in device software, we implemented a bot script, which emulates mouse and keyboard strokes, to gather this data. To check accuracy of automatic OCT segmentation in our sample, we compared the measurements with manually segmented and exported OCT scans.

Methods: Since OCT devices often not come with a batch export function of aggregated information, a robotic script was implemented in Java utilizing the java.awt.Robot package running on 2 desktop PCs at the same time. The script used image recognition techniques (based on pixel colour values) to identify specific types of OCT data and consequently adapt its behavior and start a type-specific export process based on a sequence of mouse clicks and keyboard strokes. Exported XML files were added to our smart eye database using an individual developed Java based routine. Manual segmentation and export of 7077 OCT (Spectralis OCT, Heidelberg Engineering, Germany) volume scans of patients under active Anti-VEGF treatment was performed.

Results: 72.894 OCT scans were exported and stored in the data warehouse. The initial export process took about 60 full days. The ETDRS grid within the software was changed in 11% of cases from its default position by 7.5 pixel (SD +/-53.1pixel) in automatically segmented scans vs. in 82.9% of manually segmented cases by 32.5 pixel (63.9 pixel). The average Central retinal thickness (CRT) was 344.8 um (+/- 173.6) (manually segmented) vs. 341.2 um (+/- 138.4) (automatic segmented). Figure 1 shows a Bland-Altman plot of OCT scans of 600um or less in the uncorrected export.

Conclusions: Batch exporting OCT scans using a bot script is a possible way, if not provided in the device's software. We achieved export in a relatively short time compared to manually triggered export. In a certain range of uncorrected CRT (200-400 um), most automatic segmentation done was precise. New technologies like deep learning may overcome the issue of malsegmentation and provide better results in thickened retinas.

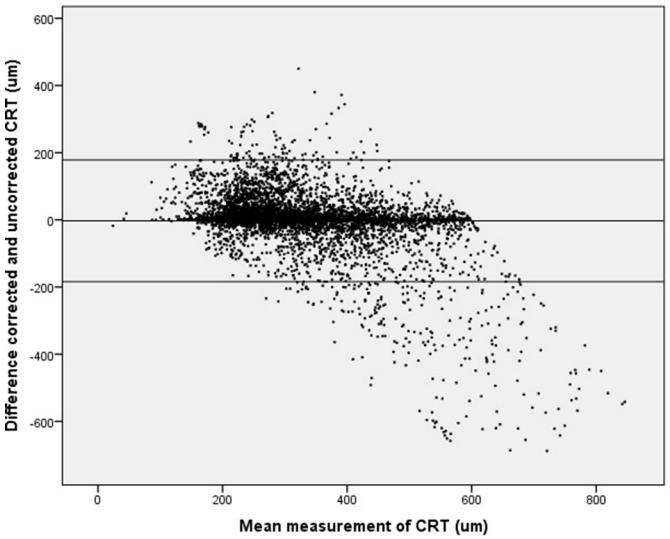

Bland-Altman plot of the two measurements for the corrected and uncorrected segmentation

Commercial Relationships: Karsten U. Kortuem, Novartis (C), Google (C), Zeiss (C), Bayer (C), Allergan (C), Novartis (F), Bayer (F); **Johannes Schiefelbein**, None; **Diana Jeliazkova**, None; **Pearse A. Keane**, Novartis (C), Google (C), Heidelberg (R), Haag-Streit (R), Novartis (R), Bayer (R), Allergan (R), Topcon (R); **Christoph Kern**, None; **Michael Müller**, None; **Wolfgang J. Mayer**, Novartis (C), Zeiss Meditec (C), Oculentis (C), Polytech/Domilens (R), Alcon (C), Zeiss Meditec (F), Alcon (F), Ziemer (F), Heidelberg Engineering (R), Ziemer (C); **Siegfried Priglinger**, None; **Daniel Nasseh**, None

Support: Partly funded by Bayer and Novartis

Program Number: 675 **Poster Board Number:** B0422
Presentation Time: 3:15 PM–5:00 PM

Aligning Automatically Sequential Spectral Slices from Multispectral Imaging (MSI) of Retina

Wanzhen Jiao[1], Yuanjie Zheng[2, 3], Jim Gee[4], Bojun Zhao[1]. [1]Ophthalmology, Shandong Provincial Hospital affiliated to Shandong University, Philadelphia, PA; [2]School of Information Science & Engineering, Shandong Normal University, Jinan, China; [3]Institute of Life Sciences, Shandong Normal University, Jinan, China; [4]University of Pennsilvania, Philadelphia, PA.

Purpose: Significant spatial misalignment may exist between discrete spectral slices captured by Multispectral Imaging (MSI) from retina because image acquisition time is often longer than natural timescale of eye's saccadic movement. Our goal is to develop a technique for aligning automatically MSI images from retina, which discovers spatial correspondence relationships between any spectral slices.

Methods: A digital image database comprising 26 MSI image sequences was acquired by using an Annidis RHA™ instrument each of which bears at least 8 slices from wavelengths of amber, green, infrared, red and yellow. These images are in a format of dicom, a bit depth of 16 and a size of 2048x2018. They are binocular images from 4 patients with hypertensive retinopathy and 8 healthy subjects. We developed a novel technique for a joint alignment of sequential MSI images by searching the lowest matching costs between automatically-detected salient feature points, which performs as solving a low-rank semidefinite matrix via a convex optimization. The proposed technique is unique for the global consistency of the generated spatial mappings between images. A trained rater manually picked 15 salient points for each MSI sequence and marked them in all MSI images, which were mixed with the algorithm-detected feature points and treated as the ground-truth in our experiments. The agreement of point-matches between the proposed computer algorithm and manual marks was assessed by computing the percentage of correct matches.

Results: The proposed automated MSI alignment technique showed an almost perfect match with human's manual works. The percentage of correct matches produced by the automated technique reached 99.3%. When the feature matching costs were added a Gaussian noise with zero mean and variances of 0.001, 0.05, 0.1, 0.15 and 0.2, respectively, percentages of correct matches became 98.5%, 97.8%, 96.3% and 95.9%, respectively, showing the robustness of the proposed technique to image noise. An exampling MSI sequence and the point-matches generated by our algorithm are shown in Figure 1.

Conclusions: The proposed automatic joint alignment technique demonstrated not only a good agreement with manually-specified matches between MSI spectral slices but also a good robustness to image noise. It also holds promise in helping to fuse retinal features measured by MSI in different spectral bands.

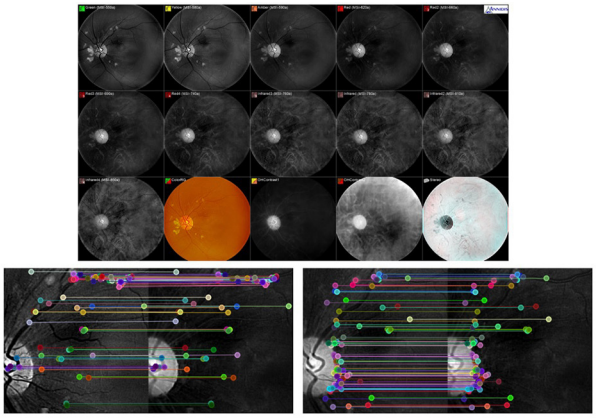

Figure 1. **Top:** A sequence of MSI images acquired by Annidis RHA from a patient diagnosed with hypertensive retinopathy, in which from left to right and from top to bottom, the first 11 images are captured with short wavelengths of ``Green'' (MSI-550), ``Yellow'' (MSI-580) and ``Amber'' (MSI-590), respectively, followed by 4 wavelengths of ``Red'' (MSI-620, MSI-660, MSI-690 and MSI-740) and 4 wavelengths of ``Infrared'' (MSI-760, MSI-780, MSI-810 and MSI-850), respectively. **Bottom:** Feature point matches (in a local area of the MSI images) generated by our algorithm between a pair of images of ``Green''-``Red'' and ``Amber-``Red'', respectively, from left to right.

Commercial Relationships: Wanzhen Jiao; **Yuanjie Zheng**, None; **Jim Gee**, None; **Bojun Zhao**, None

Support: Natural Science Foundation of China (NSFC) (61572300); Natural Science Foundation of Shandong Province in China (ZR2014FM001); Taishan Scholar Program of Shandong Province in China (TSHW201502038); Shandong Nature Science Foundation (ZR2015HM026)

Program Number: 676 **Poster Board Number:** B0423
Presentation Time: 3:15 PM–5:00 PM

Automatic Segmentation and Quantification of Subretinal Fluid on Acute Central Serous Chorioretinopathy

Manuel Falcao[1, 2], Carlos Figueiredo[1], Fernando Carvalho[3], Carlos Silva[4], Jorge Oliveira[4], Susana Penas[2], Amândio Sousa[1, 2], Fernando Falcao-Reis[1, 2]. [1]Surgery and Physiology, Faculty of Medicine of the University of Porto, Porto, Portugal; [2]Ophthalmology, Centro Hospitalar São João, Porto, Portugal; [3]Instituto Superior de Engenharia do Porto, Porto, Portugal; [4]CMEMS-UMINHO, Universidade do Minho, Guimarães, Portugal.

Purpose: Identifying and quantifying subretinal fluid (SRF) in patients with acute central serous chorioretinopathy (CSC) is of paramount importance for the management of these patients. We aimed to develop an automatic algorithm that would be able to detect and quantify subretinal fluid on spectral domain OCT (Heidelberg

Spectralis®) in patients with the acute form of the disease and to compare with manual segmentation.

Methods: Eighteen eyes of 18 patients with acute CSC were imaged on SD OCT using a macular cube centered on the fovea composed of 19 B-scans averaged 9 times. Each OCT B-Scan is composed by 509x19x432 voxels with resolution of 11.03x235x3.87. In each B-Scan subretinal fluid was identified pixel by pixel and quantified manually using GIMP image analysis software (Fig 1). An algorithm was created to identify subretinal fluid in the scans. The proposed segmentation was *based* on multi-surface segmentation using graph models controlled by intensity gradient and hard and soft constraints. Additionally, on the last processing phase, sparse high order potentials and the detection of the horizontal extremities of pathology were used to improve the subretinal fluid pockets upper limit segmentation (Fig 2). A comparison between the two segmentation methods was performed. The algorithm performance was evaluated using true positive (sensitivity) and false positive rates for each OCT volume.

Results: The mean number of pixels identified as subretinal fluid in SD-OCT volumes was 54039±70210 for the manual measurements and 69219±76539 for the automatic measurements ($p<0.001$). In all cases, the pixels identified by the algorithm were more than in the manual selection. The sensitivity of the algorithm was 0.96±0.04 and the false positive rate was 0.04±0.02.

Conclusions: Even though the automatic algorithm detected larger areas of subretinal fluid than the manual identification process, the proposed segmentation method developed has a high sensitivity for detecting subretinal fluid automatically and can be used clinically to detect the areas. Corrections in the algorithm can be made to improve the results. However, compared to manual segmentation this is a useful tool for the automatic quantification, management and follow-up of patients with acute CSC. Further improvement of the algorithm may lead to its widespread use in clinical practice.

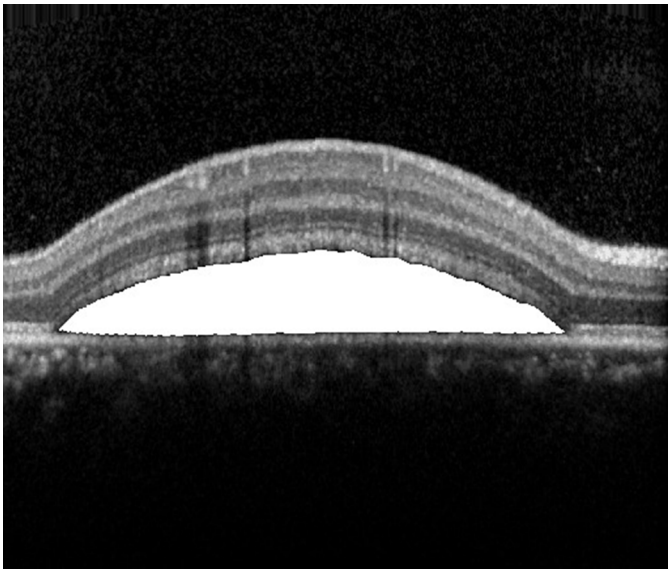

Manual Segmentation of SRF

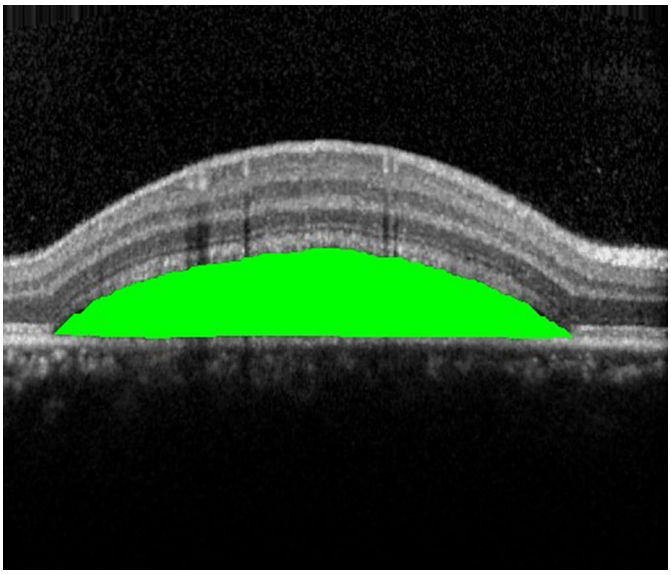

Automatic Segmentation of SRF

Commercial Relationships: Manuel Falcao, None; **Carlos Figueiredo**, None; **Fernando Carvalho**, None; **Carlos Silva**, None; **Jorge Oliveira**, None; **Susana Penas**, None; **Amândio Sousa**, None; **Fernando Falcao-Reis**, None

Program Number: 677 **Poster Board Number:** B0424
Presentation Time: 3:15 PM–5:00 PM

Evaluation of a Segmentation Method to Estimate Corneal Endothelium Parameters

Juan P. Vigueras-Guillén[1, 3], Jeroen van Rooij[2], Hans G. Lemij[2], Angela Engel[1], Lucas J. van Vliet[3], Koenraad A. Vermeer[1].
[1]Rotterdam Ophthalmic Institute, Rotterdam Eye Hospital, Rotterdam, Netherlands; [2]Rotterdam Eye Hospital, Rotterdam, Netherlands; [3]Quantitative Imaging Group, Delft University of Technology, Delft, Netherlands.

Purpose: Parameters (or biomarkers) to assess the health status of the corneal endothelium, such as cell density (ECD), polymegethism (variation in cell size, CV) and pleomorphism (% of hexagonal cells, HEX), are derived from a segmentation of the endothelial cells. The accuracy of state-of-the-art methods to estimate these parameters is limited. We evaluate a new framework to automatically estimate such biomarkers in images obtained with a Topcon SP-1P specular microscope.

Methods: Thirty central cornea images from thirty eyes with advanced glaucoma (POAG, mean age 65.5) were captured. All images and Topcon data analyses were exported. An expert annotated the cells to create the ground truth. In the proposed method, segmentation was first done by a stochastic watershed method (Selig et al., BMC Medical Imaging 15:13, 2015), such that each cell was comprised of one or more fragments. A support vector machine inferred the likelihood for all combinations of two and three adjacent fragments to form a cell, based on fourteen features regarding shape, size, and intensity of the fragments. The fragments were merged iteratively, starting with the most likely combination, until no cases with a likelihood above 0.5 remained. Based on the resulting segmentation, the biomarkers were calculated.

Results: An illustrative example of both our and the built-in Topcon method is shown in Fig. 1. Both methods show some inaccuracy in following the exact cell edges. In contrast to the Topcon method, ours segments the whole image. In Fig. 2 we display the error of the estimated biomarkers with respect to the ground truth. To compare

the two methods, a paired t-test was performed on each biomarker's error, showing significantly better accuracy for our method for ECD ($p=2.2x10^{-5}$), and comparable accuracy for CV ($p=0.07$) and HEX ($p=0.28$).

Conclusions: Inaccuracies in the segmentation of the cell boundaries have little direct impact on the biomarkers' accuracy. However, they do cause errors while merging cell fragments, resulting in over- and undersegmentation, which adversely affect the accuracy. A better initial segmentation would therefore result in more accurate biomarkers. The proposed method significantly improves the estimation of ECD, which is the clinically most important parameter.

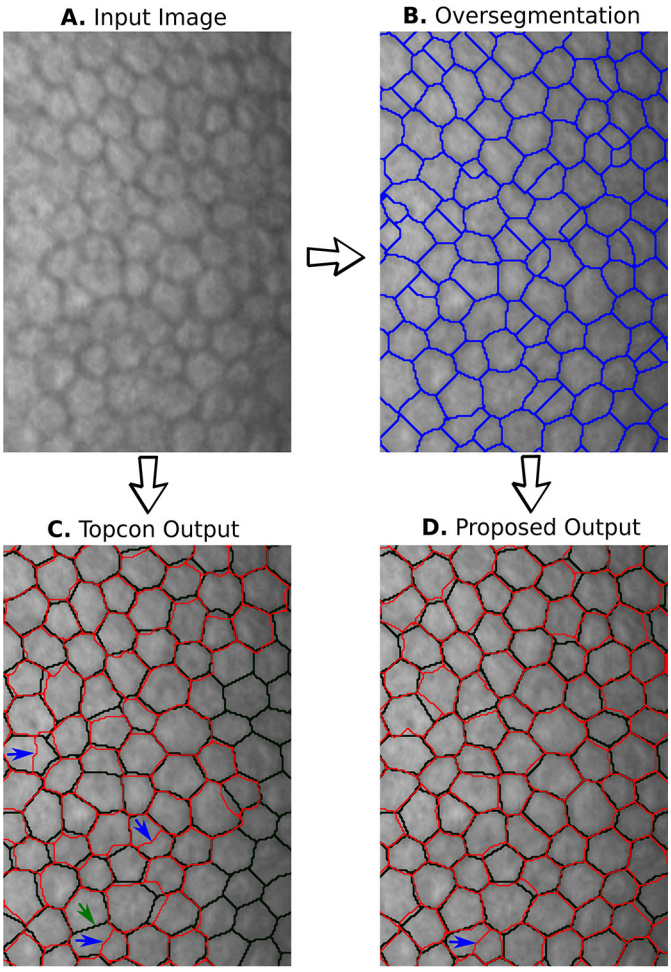

For C & D:
- Black: Ground truth.
- Red: Segmentation made by the method.
- Blue arrow: Oversegmented cell.
- Green arrow: Undersegmented cell.

Example of a segmentation result by Topcon's (C) and our method (D).

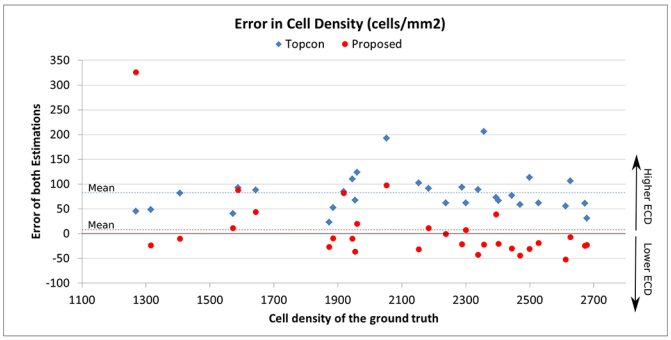

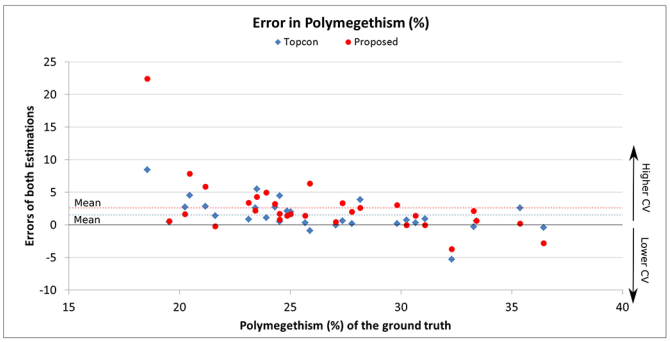

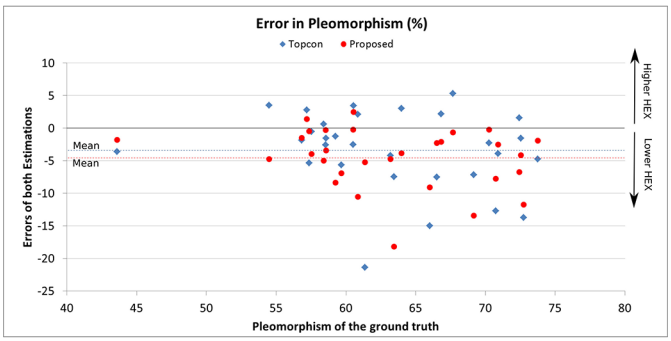

Error in ECD (top), CV (middle), and HEX (bottom) for Topcon's (blue) and our method (red).

Commercial Relationships: Juan P. Vigueras-Guillén, None; **Jeroen van Rooij**, None; **Hans G. Lemij**, None; **Angela Engel**, None; **Lucas J. van Vliet**; **Koenraad A. Vermeer**, None
Support: The Netherlands Organisation for Health Research and Development, TopZorg grants 842005002, 842005004 and 842005007

Program Number: 678 **Poster Board Number:** B0425
Presentation Time: 3:15 PM–5:00 PM

Reliability of ellipsoid zone (EZ) area and shape measurements

Travis B. Smith[1], Maria A. Parker[1], Peter Steinkamp[1], Albert Romo[1], Laura R. Erker[1], Brandon J. Lujan[1], Ning Smith[2]. [1]Casey Eye Institute, Oregon Health & Science University, Portland, OR; [2]Center for Health Research, Kaiser Permanente, Portland, OR.

Purpose: Recent studies have promoted EZ area as an effective, reliable surrogate biomarker for visual function in retinal degenerations. Reliability studies may be too optimistic if area alone is considered because dissimilar shapes can have similar areas. Here, we analyze the utility of two EZ area measurement methods and the influence of EZ shape.

Methods: EZ boundaries in volumetric SDOCT scans were marked in 88 eyes from 50 patients in the Trial of Oral VPA for Retinitis

Pigmentosa (NCT01233609) by three trained graders (2 expert, 1 novice) using two methods: transverse and enface. For transverse, EZ endpoints were marked on each b-scan (similar to Ramachandran et al, TVST, 2013 and 2016). For enface, EZ boundaries were traced on enface maximum intensity projection images (similar to Hariri et al, JAMA Ophthalmol, 2016). Each method produced an EZ boundary polygon and associated EZ area (Fig 1a,b). EZ area differences (between graders, over time, etc) were compared by simple subtraction of areas, and by a shape-sensitive approach using the area of symmetric difference (ASD). The ASD of two polygons is the area of their union minus their intersection, and detects differences in differently shaped EZ regions even if they have similar areas (Fig 1c).

Results: Table 1 reports grading times and reliability metrics. The transverse method was the most reliable but only among expert graders, while the enface method was about twice as fast with better agreement among all graders. After accounting for shape differences with ASD, grader agreement for both methods was still good to excellent, but significantly reduced ($p<0.001$ for all comparisons) and, for the enface method, much lower than published studies based on area alone. Fig 1d shows the percent change in EZ boundary over one year plotted by retinal direction, an example result made possible by shape analysis.

Conclusions: EZ boundary shape should be considered when quantifying differences and longitudinal changes in EZ area. Doing so will resolve the geometric ambiguity of the area, improve change detection sensitivity, and provide new opportunities for EZ change analysis.

		Transverse		Enface	
		Area	ASD	Area	ASD
All graders	Mean grading time (min)	9.6		5.0	
	RC (mm^2)	3.0	3.7	1.6	1.8
	ICC [95% CI]	0.824 [0.483, 0.921]	0.458 [0.329, 0.579]	0.943 [0.903, 0.965]	0.830 [0.769, 0.879]
Expert graders	Mean grading time (min)	8.3		4.5	
	RC (mm^2)	0.52	0.99	1.3	2.0
	ICC [95% CI]	0.993 [0.989, 0.995]	0.957 [0.935, 0.972]	0.959 [0.935, 0.973]	0.820 [0.738, 0.878]

RC: repeatability coefficient
ICC: intraclass correlation coefficient of inter-grader agreement
CI: confidence interval

Table 1: EZ area measurement comparison.

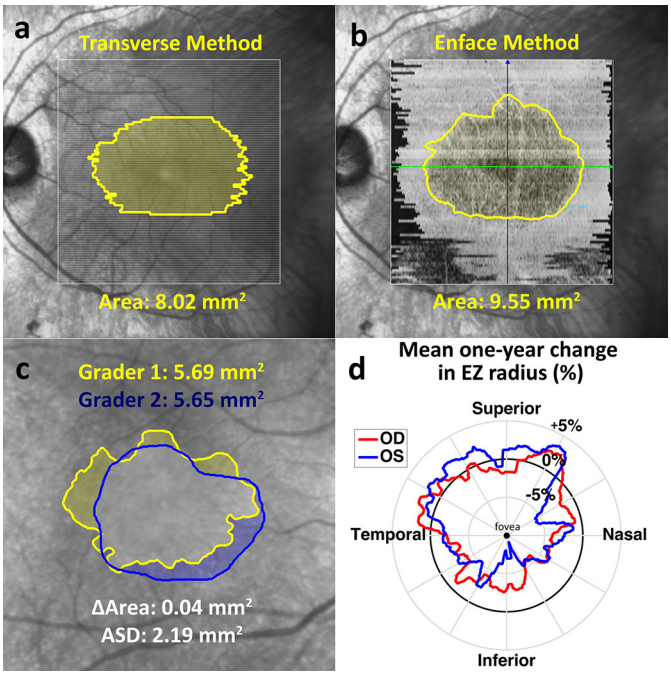

Figure 1: Example exam after (a) transverse and (b) enface EZ measurement. (c) Geometric ambiguity: ASD detects the difference between two dissimilar EZ regions; area does not. (d) One-year change localized by retinal direction show EZ loss in most directions except superior.

Commercial Relationships: Travis B. Smith, None; **Maria A. Parker**, None; **Peter Steinkamp**, None; **Albert Romo**, None; **Laura R. Erker**, None; **Brandon J. Lujan**, Genentech (C), UC Berkeley (P), Genentech (F), Genentech (R); **Ning Smith**, None
Support: The VPA Clinical Trial for RP is sponsored by the Foundation Fighting Blindness Clinical Research Institute.
Clinical Trial: NCT01233609

Program Number: 679 **Poster Board Number:** B0426
Presentation Time: 3:15 PM–5:00 PM

Normative dataset for retinal layers' thickness maps automatically generated by spectral domain optical coherence tomography in a Caucasian population

Alessandra Acquistapace[1], Alessandro Invernizzi[1, 2], Marco Pellegrini[1], Eleonora Benatti[3], Stefano Erba[1], Mariano Cozzi[1], Mario V. Cigada[1], Francesco Viola[3], Giovanni Staurenghi[1].
[1]Department of Clinical Science, Sacco Hospital Eye Clinic, Milano, Italy; [2]University of Sydney, Save Sight Institute, Sidney, NSW, Australia; [3]University of Milan, Ophthalmological Unit, IRCCS-Cà Granda Foundation – Ospedale Maggiore Policlinico, Department of Clinical Sciences and Community Health, Milan, Italy.

Purpose: To collect a dataset of normative ETDRS thickness maps values for each of the 7 retinal layers automatically generated by the Spectralis SD-OCT software (Heidelberg Engineering, Germany) in a healthy Caucasian population and to test the effect of age, sex and axial length (AXL) on such values.

Methods: 30x25 degrees volume scans centred on the fovea (61 b-scans, 120 mm inter-scan distance, 16 ART frames) were collected on healthy Caucasian subjects. Automatic segmentation of retinal layers was performed using the inbuilt software function. In one eye from each subject mean thickness values in the central subfield (C), inner ring (IR) and outer ring (OR) of the ETDRS grid were than

calculated for each layer. A multivariate regression analysis was used to test the effect of age, sex and AXL on these values.
Results: 200 subjects (110 females) were enrolled. Mean age was 39.9±13.9 years (range 20-74). Mean AXL was 24.30±1.07 mm (range 22.23-27.14). Thickness values in the 3 main ETDRS subfield are reported for each retinal layer in Table 1. Nerve fiber layer thickness increased with age in the IR (p=0.006). Ganglion cells thickness was higher in males (p=0.009) in the IR and OR, it was also negatively correlated with AXL in the OR (p<0.0001) but positively correlated with the AXL in the C (p=0.001). Inner plexyform layer was thicker in males (p=0.0007) in the IR and thinner in longer eyes in the OR (p=0.0001). Inner Nuclear Layer was thicker in males in the C and IR (p<0.0001) and negatively correlated with age in the OR (p=0.008). Outer plexyform layer thickness didn't change with age and gender but was positively correlated with AXL in the C (p=0.0004). Outer nuclear layer thickness was higher in males in all subfields (all p<0.0009) and decreased in with age in the OR (p=0.003). Retinal pigment epithelium increased in thickness with age (p=0.008) in the IR but wasn't affected by sex or AXL in any of the subfields.
Conclusions: The thickness of each retinal layer in a large Caucasian population are provided. Age, sex and AXL have an influence on retinal layers thickness. The effect of these factors may vary according to the layer and the ETDRS subfield. Large datasets are needed to provide normative referring values.

Layer	Subfield	Thickness (mean ± SD)	Intercept	Age		Gender (m)*		Axial Length	
				Coeff.	p	Coeff.	p	Coeff.	p
Full Retina	Center	280.1±17.5	173.5	0.49	0.001	11.25	0.001	3.54	0.02
	Middle Ring	343.4±13.9	386.1	0.11	0.32	12.59	**<0.0001**	-2.09	0.07
	Outer Ring	298.2±12.8	393.7	-0.20	0.05	8.33	**0.0004**	-3.74	**0.0004**
RNFL	Center	12.8±1.8	8.2	0.01	0.35	0.70	0.06	0.15	0.36
	Middle Ring	23.2±1.7	20.5	0.04	0.006	0.04	0.89	0.04	0.77
	Outer Ring	38.8±4.4	32.1	0.09	0.01	-2.35	0.004	0.17	0.63
GCL	Center	17.2±3.9	-14.7	0.03	0.43	1.37	0.10	1.27	0.001
	Middle Ring	52.7±4.0	55.9	0.00	0.81	1.96	0.009	-0.15	0.65
	Outer Ring	35.4±3.1	64.5	-0.05	0.02	1.39	0.009	-1.14	**<0.0001**
IPL	Center	22.5±3.2	2.6	0.05	0.08	1.58	0.02	0.73	0.01
	Middle Ring	42.4±2.8	48.5	-0.00	0.95	1.78	**0.0007**	-0.26	0.25
	Outer Ring	28.9±2.3	48.6	-0.03	0.04	1.04	0.01	-0.76	**0.0001**
INL	Center	19.4±4.5	-4.2	0.09	0.02	3.33	**0.0001**	0.80	0.04
	Middle Ring	39.7±3.0	47.4	0.00	0.89	2.61	**<0.0001**	-0.35	0.20
	Outer Ring	32.6±2.2	46.3	-0.05	0.008	0.93	0.02	-0.49	0.01
OPL	Center	26.0±6.0	-22.2	0.06	0.24	-1.53	0.18	1.91	**0.0004**
	Middle Ring	33.1±4.5	20.0	0.02	0.51	-1.17	0.16	0.50	0.18
	Outer Ring	26.9±2.2	33.4	0.01	0.55	0.03	0.92	-0.30	0.09
ONL	Center	92.2±9.3	102.8	0.18	0.01	5.77	**0.0009**	-0.76	0.32
	Middle Ring	71.0±7.6	101.2	-0.00	0.91	6.18	**<0.0001**	-1.30	0.04
	Outer Ring	57.7±6.0	87.9	-0.15	0.003	5.39	**<0.0001**	-1.07	0.03
RPE	Center	17.4±1.9	20.5	-0.01	0.30	-0.31	0.43	-0.10	0.58
	Middle Ring	15.1±1.4	17.4	0.03	0.008	0.32	0.21	-0.15	0.19
	Outer Ring	13.3±1.3	13.1	0.01	0.35	0.53	0.04	-0.02	0.86

Coeff.=Coefficient; RNFL=Retinal Nerve Fiber Layer; GCL=Ganglion Cells Layer; IPL=Inner Plexyform Layer; INL=Inner Nuclear Layer; OPL=Outer Plexyform Layer; ONL=Outer Nuclear Layer; RPE=Retinal Pigment Epithelium

*= The values for coefficient refers to the male gender

Thickness values in the 3 main ETDRS subfields and the effect of age, sex, axial length are reported for each retinal layer.

Commercial Relationships: Alessandra Acquistapace, None; **Alessandro Invernizzi**, Allergan (R); **Marco Pellegrini**, Optovue (R); **Eleonora Benatti**, None; **Stefano Erba**, None; **Mariano Cozzi**, Bayer AG (F), Alcon (F), Heidelberg Engeneering (F); **Mario V. Cigada**, None; **Francesco Viola**, Novartis (C), Bayer (C); **Giovanni Staurenghi**, Alcon (R), Alcon (C), Optovue (F), Zeiss (F), Ocular Instruments (P), Boehringer Ingelheim (C), Novartis (C), Optos (C), Roche (C), Novartis (R), Bayer (C), Heidelberg Engineering (C), Bayer (R), Novartis (F), Genentech (C), Heidelberg Engineering (R), Zeiss (C), Allergan (C)

Program Number: 680 **Poster Board Number:** B0427
Presentation Time: 3:15 PM–5:00 PM

Retinal Surface Detection in intraoperative Optical Coherence Tomography (iOCT)

Moritz Pettenkofer, M. Ali Nasseri, Mingchuan Zhou, Chris Lohmann. Ophthalmology, Munich Tech University, Munich, Germany.

Purpose: Goal of the present study is to investigate retinal surface detection and precision using intraoperative OCT imaging. The precise tracking of the individual retinal layers may help to achieve a higher reliability and safety in macular micro-surgery due to a higher control level of intraoperative actions such as sub-retinal injections, epiretinal membrane peel and macular hole surgery.
Methods: 20 eyes of 20 patients with various retinal diseases such as full-thickness macular hole, macular pucker, diabetic retinopathy or vitreous hemorrhage were randomly included in this study. All images were obtained from Zeiss Lumera 700 Rescan Microscope. Surface pixels were detected by image processing methods, using a tracking algorithm. For each eye 20 detections were performed to evaluate the repeatability of the method.
Results: The mean detected surface precision was shown as 12.1104 pixels. The minimum tracking error was investigated to be 6.00 pixels and the maximum 32.00 pixels.
Conclusions: In the present study we introduced a tracking algorithm for retinal surface detection using intraoperative OCT images. Our method could be applicable for current clinical routines as well as future vitreoretinal diagnosis and treatments. It is the first step towards future technologies in retinal tracking unsable for sub-retinal injection, intraoperative retinal vein detection and tracking such as intraoperative macular hole analysis.

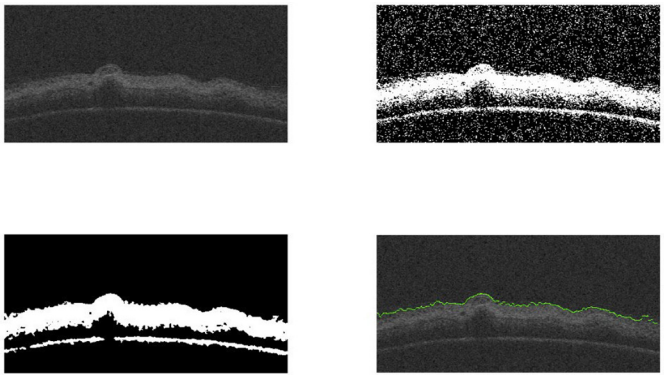

Commercial Relationships: Moritz Pettenkofer, None; **M. Ali Nasseri**, None; **Mingchuan Zhou**, None; **Chris Lohmann**, None

Program Number: 681 **Poster Board Number:** B0428
Presentation Time: 3:15 PM–5:00 PM
Automatic analysis of retinal oximetry images
Sveinn H. Hardarson[2], Robert A. Karlsson[3], Olof B. Olafsdottir[1], Thorunn S. Eliasdottir[1], Toke Bek[4], Einar Stefansson[1].
[1]Ophthalmology, University of Iceland, Reykjavik, Iceland; [2]Institute of Physiology, University of Iceland, Reykjavik, Iceland; [3]Oxymap ehf., Reykjavik, Iceland; [4]Aarhus University Hospital, Aarhus, Denmark.
Purpose: Oxygen saturation in retinal blood vessels can be measured from fundus images, taken at two different wavelengths. The purpose of the study was to develop and test software to automate and improve analysis of oximetry images.
Methods: The Oxymap T1 oximeter takes two images at the same time, one with light at a wavelength that is sensitive to changes in oxygen saturation (600nm) and one at an insensitive wavelength (570nm). Oximetry images were analysed with manual and automatic approaches. The manual analysis requires that the user selects vessel segments for analysis according to a detailed protocol. The automatic analysis software selects measurement points and automatically calculates median saturation values for each eye.
For testing of repeatability and sensitivity, images were taken of 22 healthy individuals. These images were also used to calibrate the automatic method. Additional testing was performed on oximetry images of 54 diabetic patients.
Results: Standard devation of repeated manual measurements of the same healthy eye was 0.96 percentage points for arterioles and 1.95 percentage points for venules. The corresponding values for automatic measurements were 1.17 (arterioles) and 1.61 percentage points (venules). According to the automatic method, oxygen saturation in retinal arterioles was 92.6±3.1% during breathing of room air and 94.8±2.7% during pure oxygen breathing ($p<0.0001$). Corresponding values for venules were 58.8±5.2% (normoxia) and 78.2±7.6% (hyperoxia, $p<0.0001$). The table shows results for 54 diabetic patients, analyzed with the automatic software.
Arteriolar saturation in the PDR group was significantly higher than saturation in the other two groups ($p<0.05$). For venules, differences between all pairs of groups were statistically significant.
Conclusions: Automatic analysis of retinal oximetry images is faster and less subjective than manual analysis. Repeatability and sensitivity of the automatic method have been established. The automatic analysis can be used for oximetry on diabetic patients, where it yields similar results as have previously been found with the manual approach.

	DM, no DR (n=16)	NPDR (n=24)	PDR (n=14)
Arterioles	(90.9±2.5)%	(93.2±3.9)%	(99.5±4.8)%
Venules	(61.3±5.2)%	(66.0±5.5)%	(71.2±6.3)%

Table. Oxygen saturation (mean±SD) measured with automatic software. DM=Diabetes mellitus. NPDR=Non-proliferative diabetic retinopathy. PDR= Proliferative diabetic retinopathy.

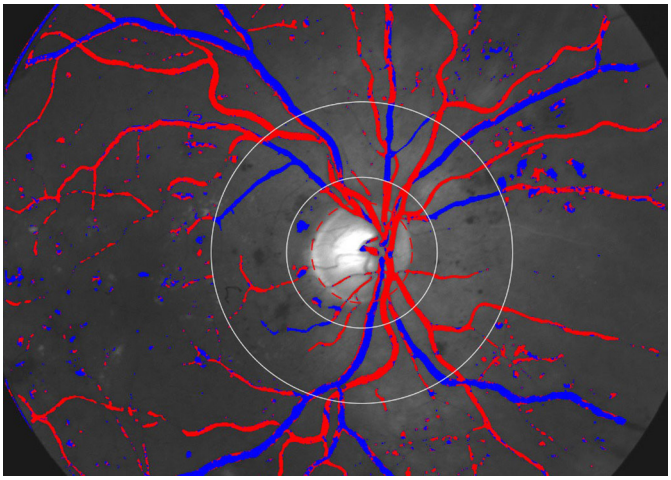

Figure. Automatic classification into arterioles and venules. Current software requires minor manual correction of classification.
Commercial Relationships: Sveinn H. Hardarson, Oxymap ehf. (P), Oxymap ehf. (C), Oxymap ehf. (I); **Robert A. Karlsson**, Oxymap ehf. (P), Oxymap ehf. (E), Oxymap ehf. (I); **Olof B. Olafsdottir**, None; **Thorunn S. Eliasdottir**, None; **Toke Bek**, None; **Einar Stefansson**, Oxymap ehf. (S), Oxymap ehf. (P), Oxymap ehf. (I)
Support: Icelandic Research Council

Program Number: 682 **Poster Board Number:** B0429
Presentation Time: 3:15 PM–5:00 PM
Quantitative volumetric analysis of retinal tissue oxygen tension
Anthony Felder, Justin Wanek, Norman P. Blair, Mahnaz Shahidi.
Ophthalmology & Visual Sciences, University of Illinois at Chicago, Chicago, IL.
Purpose: Retinal function is sustained by oxygen delivered from dual circulatory systems, the contributions of which create complex oxygen gradients through the retinal depth. Localized regions of inadequate oxygenation occur in several retinal diseases, including diabetic retinopathy and vascular occlusions. Previous studies assessed retinal oxygenation in limited spatial dimensions, which precluded the detection of disseminated pathologies. Therefore, techniques that volumetrically assess retinal oxygenation are necessary to understand retinal physiology in health and disease. We report a method for the 3D imaging of retinal tissue oxygen tension (tPO_2) and the 2D mapping of outer retinal oxygen consumption (QO_2) in rats.
Methods: Phosphorescence lifetime imaging was performed in male Long Evans pigmented rats under systemic normoxia (N=6) and hypoxia (N=3), one day after intravitreal injection of an oxyphor. A vertical laser line was horizontally scanned across the retina and a series of depth-resolved phosphorescence optical section images were acquired. An automated customized software algorithm constructed phase-delayed phosphorescence volumes, determined the phosphorescence lifetime at each voxel, and generated a 3D retinal tPO_2 volume. The volumetric data was fitted using an oxygen diffusion model to map QO_2 in 2D. The effects of systemic condition (normoxia, hypoxia) and retinal depth on mean tPO_2 (M_{tPO2}) and the spatial variation of tPO_2 (SV_{tPO2}), measured as SD, were determined by mixed linear model. Mean QO_2 (M_{QO2}) and spatial variation of QO_2 (SV_{QO2}) were compared between normoxia and hypoxia by unpaired t-tests.
Results: 3D retinal tPO_2 volumes were approximately 500x500x200µm (horizontal x vertical x depth). M_{tPO2} measured at

the chorioretinal interface was significantly correlated with systemic arterial PO_2 (P=0.007; N=9). There were significant effects of both systemic condition and retinal depth on M_{tPO2} and SV_{tPO2}, such that both were lower under hypoxia than normoxia and higher in the outer retina than inner retina (P<0.001). No statistically significant difference was found in M_{QO2} or SV_{QO2} between normoxia and hypoxia (P≥0.16).
Conclusions: For the first time, 3D imaging of retinal tPO_2 and 2D mapping of outer retinal QO_2 were demonstrated, with potential for the assessment of disseminated physiological alterations in animal models of retinal diseases.
Commercial Relationships: Anthony Felder, None; **Justin Wanek**, None; **Norman P. Blair**, None; **Mahnaz Shahidi**, None (P)
Support: NIH grants EY017918 and EY001792, Research to Prevent Blindness

Program Number: 683 **Poster Board Number:** B0430
Presentation Time: 3:15 PM–5:00 PM
Deep Learning System for Screening of Diabetic Retinopathy, Glaucoma and Age-related Macular Degeneration Using Retinal Photographs: The DEEP EYE Study
Gilbert Lim[1], Daniel Shu Wei Ting[2, 3], Carol Y. Cheung[2, 4], Gavin S. Tan[2, 3], Rina Rudyanto[1], Alfred T. Gan[2], Ching-Yu Cheng[2, 3], Wynne Hsu[1], Mong Li Lee[1], Tien Yin Wong[2, 3]. [1]School of Computing, National University of Singapore, Singapore, Singapore; [2]Singapore Eye Research Institute, Singapore National Eye Centre, Singapore, Singapore; [3]Duke-NUS Graduate Medical School, National University of Singapore, Singapore, Singapore; [4]Department of Ophthalmology and Visual Sciences, Chinese University of Hong Kong, Hong Kong, Hong Kong.
Purpose: Deep learning is a breakthrough machine learning technique that has exhibited substantial promise in image classification. The purpose of this study is to evaluate the diagnostic performance of a deep learning system (DLS) in detecting diabetic retinopathy (DR), age-related macular degeneration (AMD) and glaucoma suspect, using a large-scale national screening population of patients with diabetes in Singapore.
Methods: The DLS was trained for referable DR, AMD and glaucoma on retinal images captured under the Singapore Integrated Diabetic Retinopathy Program (SiDRP; total images=148,266) between 2010-13, followed by validation on images from 2014-15. Referable DR was defined as moderate non-proliferative DR (NPDR) and above, while vision-threatening DR (VTDR) was defined as severe NDPR and above. AMD was defined using the Wisconsin AMD grading system, based on the presence of drusen, retinal pigmentary abnormalities, geographic atrophic atrophy and neovascular changes. Glaucoma suspect was based on a vertical cup-disc ratio of 0.7 and above, or the presence of any glaucomatous disc changes (e.g. disc hemorrhage, focal notching). We calculated the sensitivity and specificity of the DLS with reference to the grading done by professional graders. All retinal images were analyzed twice to evaluate the repeatability of DLS.
Results: Of the 148,266 images, 76,370 were used for training, and 71,896 were used for clinical validation. For DR, the sensitivity and specificity were 0.904 (95% CI=0.872-0.930) and 0.919 (95% CI=0.916-0.922) respectively for referable DR, and 1.000 (95% CI=0.940-1.000) and 0.911 (95% CI=0.908-0.914) respectively for VTDR. For AMD, the sensitivity and specificity were 0.816 (95% CI=0.710-0.896) and 0.817 (95% CI=0.813-0.821) respectively. For glaucoma suspect, the sensitivity and specificity were lower at 0.782 (95% CI=0.716-0.839) and 0.784 (95% CI=0.780-0.788) respectively.
Conclusions: DLS demonstrated promising results in detecting DR, AMD and possibly glaucoma suspects, using retinal photographs from patients with diabetes. Further large-scale testing and validation with additional cohorts from different sources will help in confirming the potential of the DLS for use for screening.
Commercial Relationships: Gilbert Lim; **Daniel Shu Wei Ting**, None; **Carol Y. Cheung**, None; **Gavin S. Tan**, None; **Rina Rudyanto**, None; **Alfred T. Gan**, None; **Ching-Yu Cheng**, None; **Wynne Hsu**, None; **Mong Li Lee**, None; **Tien Yin Wong**, None
Support: National Health Innovation Centre (NHIC) Innovation to Develop (I2D) Grant, National Medical Research Council (NMRC), Singapore. (NHIC-I2D-1409022)

Program Number: 684 **Poster Board Number:** B0431
Presentation Time: 3:15 PM–5:00 PM
A Machine Learning Based Automated Image Quality Assessment Tool for Color Fundus Images Taken with VISUSCOUT 100 Handheld Camera
Abhishek Rawat[1], Chandan Chakraborty[2], Suman Tewary[2], Keyur Ranipa[1], KRUNALKUMAR RAMANBHAI PATEL[1]. [1]CARIn, Carl Zeiss India Pvt Ltd, Bangalore, India; [2]SMST, IIT Kharagpur, Kharagpur, India.
Purpose: Fundus images obtained using handheld cameras have been observed to have a wide variation in their image quality. Since the images are obtained by operators having different levels of experience and under vastly different operating conditions, the image quality generated by the same hardware can be vastly different. Therefore it was desired to develop an automated and objective image quality metric which can grade the input images in real time, allowing the operator to rescan the patient in case image quality was bad. Here we present such a tool by training a set of classifiers in grading a fundus image using relevant features from the image. The trained classifier then automatically classifies an input fundus image as clinically gradable or not.
Methods: We used 1888 color fundus images taken with VISUSCOUT® 100 (ZEISS, Jena, Germany) handheld fundus camera as the training set. These images were manually classified by experts as gradable/non-gradable.Standard data augmentation techniques such as rotation & mirroring were used to increase the sample size. We used a separate dataset with 2407 gradable & 130 non-gradable images as the test set.
Some of the relevant criteria which define image quality are image sharpness/focus, signal-to-noise, optic disc localizability & having other non-fundus input. Using the training dataset, six features were extracted from each fundus image: optic disc present/absent, extent of upper vessel coverage, extent of lower vessel coverage, light leakage present/absent, brightness & illumination variance.
This set of six image features determined for the training images were then used for training four classifiers:Random Forest, Decision Tree, K Nearest Neighbors & SVM.The testing was then done on the test dataset with known image quality classification and the sensitivity/specificity numbers were calculated for the four classifiers mentioned above.
Results: The sensitivity/specificity results for the four classifiers are given in Table1.
Conclusions: The presented classifiers trained on the relevant fundus image features showed good accuracy in classifying VISUSCOUT 100 images as gradable/non-gradable in an automated manner. They could be used as a pre-filter for a fundus image based remote screening program allowing for better clinical outcomes.

	Accept (Specificity)	Discard (Sensitivity)
Random Forest	2263 / 2407 = 94.02%	114 / 130 = 87.69%
KNN	2076 / 2407 = 86.25%	118 / 130 = 90.77%
Decision Tree	2304 / 2407 = 95.73%	114 / 130 = 87.69%
SVM	2193 / 2407 = 91.11%	121 / 130 = 93.08%

Table 1: Sensitivity/specificity for the four classifiers

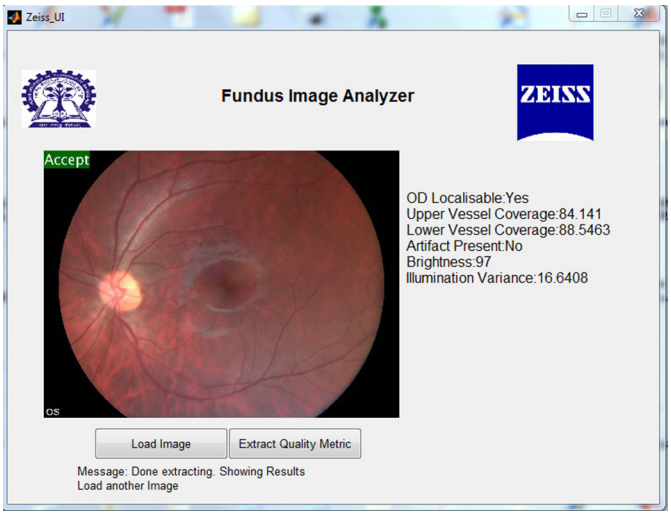

Fig 1: Screenshot of the automated image quality tool

Commercial Relationships: Abhishek Rawat, Carl Zeiss India (Bangalore) Pvt Ltd (E); **Chandan Chakraborty**, IIT Kharagpur (F); **Suman Tewary**, IIT Kharagpur (F); **Keyur Ranipa**, Carl Zeiss India (Bangalore) Pvt Ltd (E); **KRUNALKUMAR RAMANBHAI PATEL**, Carl Zeiss India (Bangalore) Pvt Ltd (E)

Program Number: 685 **Poster Board Number:** B0432
Presentation Time: 3:15 PM–5:00 PM
Deep-learning estimation of choroidal thickness from color fundus photographs

Hironobu Tampo[1], Hidenori Takahashi[1], Yasuo Yanagi[2], Shin-ichi Sakamoto[1], Satoru Inoda[1], Hidetoshi Kawashima[1], Yuji Inoue[1], Yusuke Arai[1], Ryota Takahashi[1], Megumi Soeta[1]. [1]Ophthalmology, Jichi Medical University, Shimotsuke City, Japan; [2]Singapore Eye Research Institute, Singapore, Singapore.

Purpose: The accuracy of general image classification has drastically improved since the advent of automatic extraction by deep learning to identify characteristic points in images. In 2015, artificial intelligence by deep learning was reported to be more accurate than human beings for the first time. Few reports have considered the application of deep-learning analysis to fundus photographs. Here, we applied deep learning to automate estimation of choroidal thickness from color fundus photographs.

Methods: We used images from 597 subjects who underwent same-day optical coherence tomography examination (swept-source OCT) [DRI-OCT (TOPCON, TOKYO)] and color fundus photography using a fundus camera [VX-10 (KOWA, AICHI)] at the outpatient clinic of Jichi Medical University hospital. From these images, those showing any of age-related macular degeneration, central serous chorioretinopathy, and proliferative diabetes retinopathy were excluded. Central choroidal thickness (CCT) was measured manually with OCT. When more than 6 images were available of a single eye, 5 of those images were used for classifier training. Forty eyes had only 1 associated fundus photograph. Images of the 3 eyes with the highest variance in CCT (due to diurnal variance) were excluded. Of the fundus photographs, 546. were used for deep learning. The deep learning system was run on a workstation (graphical processing units: 4) for 51 h. The 51 excluded photographs were used for validation.

Results: The correlation coefficient for the 40 single-photograph eyes was 0.69. The same-eye correlation coefficients for the 3 eyes with highest CCT variance were 0.98, -0.96, and 0.45, in order of decreasing variance.

Conclusions: Artificial intelligence by deep learning estimated CCT from the color fundus photographs with good accuracy. However, single-eye diurnal CCT variation was not estimated well.

Commercial Relationships: Hironobu Tampo, Senju (R), Santen (R), Bayer (R); **Hidenori Takahashi**, DeepEyeVision LLC (I), Santen (R), Jichi Medical University (P), Kowa (R), Bayer (R), Novartis (F); **Yasuo Yanagi**, Novartis (C), Bayer (C), Santen (C); **Shin-ichi Sakamoto**, None; **Satoru Inoda**, Novartis (R), Bayer (R); **Hidetoshi Kawashima**, Senju (R), Santen (R), Kowa (R), Novartis (R), Bayer (R); **Yuji Inoue**, Novertis (R), Santen (R), Bayer (R); **Yusuke Arai**, Novartis (R), Bayer (R); **Ryota Takahashi**, None; **Megumi Soeta**, None

Support: Novartis Grant

Program Number: 686 **Poster Board Number:** B0433
Presentation Time: 3:15 PM–5:00 PM
Use of Opacity Suppression enhancement software improves quality of color fundus, fundus autofluorescence, and anterior segment images obtained during teleglaucoma screenings

Alice Wang, Bernard Szirth, Albert S. Khouri. Rutgers - New Jersey Medical School, Nutley, NJ.

Purpose: Compare ocular imaging quality pre and post capture enhancement using an Opacity Suppression (OS) software for color fundus (CF), monochromatic fundus autofluorescence (FAF) and anterior segment (AS) imaging.

Methods: Thirty glaucoma subjects were selected from our teleglaucoma community screenings. All the images were digitally enhanced using an OS proprietary software (Canon, Inc), which filters blue wavelengths and increases edge sharpness. Each image was graded independently by 2 expert readers. CF, FAF, and AS images were graded on a published 1-5 scale pre and post-OS. A paired T-test was used to compare the image grades pre and post- OS. Additional criteria were assessed post- OS on a 1-3 scale (1=similar, 2=improved, 3=significantly improved) for CF and AS, and a 1-2 scale (1=similar, 2=improved) for FAF. Criteria included peripapillary, drusen/RPE, NFL detail, media opacity, iris detail, conjunctival lesions, and retinal abnormalities. To determine any effect of OS on visualization of the optic nerve, we measured the reflected lumens values (adobe photoshop 7.0.1) of the optic nerve pre and post- OS for CF images. A paired T-test was used to compare lumens values pre and post-OS.

Results: One hundred sixty images (58 CF, 51 AS, 51 FAF) were assessed by both graders. Post-OS images scored significantly higher than pre-OS for CF, FAF, and AS. (Grader 1 p=0.000, 0.004, 0.000/ Grader 2 p=0.000, 0.000, 0.000, respectively). Additional criteria assessed showed greatest improvement in visualization of drusen/RPE, conjunctival lesions, and iris detail. 52 CF images were assessed for lumens. Post-OS lumens values were significantly higher (p= 0.000) indicating possible bleaching of rim color.

Conclusions: OS software significantly improved the quality of CF, FAF, and AS images. This may have important applications in teleglaucoma by improving the quality of images obtained during community screenings where pupillary dilation is often not administered. However, enhancements can lead to bleaching of the optic disc colors, which may negatively impact the ability to assess the rim and thus glaucoma diagnosis. Future software applications and adjustments will allow improvement in retina evaluation while avoiding optic nerve head color changes.

Pre/Post-OS, Grading scale 1-5		Grader 1 Avg	Grader 2 Avg
CF	Original	3.43	3.45
	Enhanced	3.86	4.03
AS	Original	3.84	3.88
	Enhanced	4.24	4.51
FAF	Original	3.25	3.49
	Enhanced	3.47	3.76
Additional Criteria Post-OS, Grading scale 1-3			
CF	Peripapillary	1.74	1.86
	Drusen/ RPE	1.95	2.29
	NFL detail	1.43	1.71
AS	Media opacity	1.29	1.98
	Iris Detail	1.91	1.86
	Conjunctival Lesions	1.83	2.02
Additional criteria Post-OS, Grading scale 1-2			
FAF	Peripapillary	1.80	1.53
	Retinal Abnormalities	1.90	1.65

Table 1: Averages of pre and post-OS grades

Commercial Relationships: Alice Wang, None; **Bernard Szirth**, None; **Albert S. Khouri**, None

Program Number: 687 **Poster Board Number:** B0434
Presentation Time: 3:15 PM–5:00 PM

Automated detection and quantification of retinal nerve fibre layer defects on fundus photography

Aparna Rao[1], Rashmi Panda[2], Niladri Puhan[3], Debananda Padhy[1]. [1]Glaucoma Services, LV Prasad Eye Institute, Odihsa, India, Bhubaneswar, India; [2]PhD scholar, School of Electrical sciences, IIT Bhubaneswar, Bhubaneswar, India; [3]Assisstant professor, School of electrical Sciences, IIT Bhubaneswar, Bhubaneswar, India.

Purpose: To evlaute performance of a computer-aided RNFLD detection alogirthm for efficient automated glaucomatous RNFL changes on fundus images.

Methods: A total of 68 fundus images with discernible RNFLD (cases) or glaucomatous changes adjudged by clincian with or without visual field defects were comapred with eyes without RNFLD (controls) and clear media acquired by the which are divided into training set (13 images) and testing set (55 images) Visupac version 4.4.4 camera (FF 450 plus IR Carl Zeiss Ltd. USA) with 5 *x* magnification and 20^0, 30^0, 50^0 field of views (FOV) were selected. After segmenting and inpainting of blood vessels, Contrast limited adaptive histogram equalization (CLAHE) was applied and candidate RNFLD boundary pixels found by wavelet based local minima analysis of the 1-D intensity profiles extracted from the concentric circles around the optic disc. Novel patch features such as Cumulative Zero Count Local Binary Pattern (CZC –LBP) and Directional Differential Energy (DDE) were applied for boundary pixel classification, Figure 1. For measuring RNFLD angular width, the detected boundary pixels are line fitted using Random Sample Consensus (RANSAC) algorithm. Diagnostic performance of the new algorithm was compared with clinician's judegement (gold standanrd), two blinded trained graders and Spectral domain OCT. To quantify the closeness of detected RNFLD boundary from the gold standard, mean Euclidean distance (*EDmean*) was computed.

Results: Agreement between graders for number of RNFD was excellent (ICC 0.86). We tested the proposed new algorithm on 78 RNFLD region boundaries present in 29 of 55 cases. We could detect 61 with 15 FPs using the proposed method which gave an area under the curve of 0.87 using the free response curve with a sensitivity and false positive per image of 78.2% and 0.27, respectively. The maximum value of mean and standard deviation of the detected RNFLD width from the gold standard and existing algorithm are around 10 pixels which implies that the fitted lines are close to the gold standard, Figure 2. The AUC for the algorithm, blinded graders and SD-OCT were 0.92, 0.89&0.78 and 0.83 respectivley. The algirthm picked up 11 small RNFLD missed by OCT and 16 defects missed by the graders.

Conclusions: The proposed method achieves good accuracy as compared to SD-OCT and gold standard which can be used for automated assessment of RNFL changes.

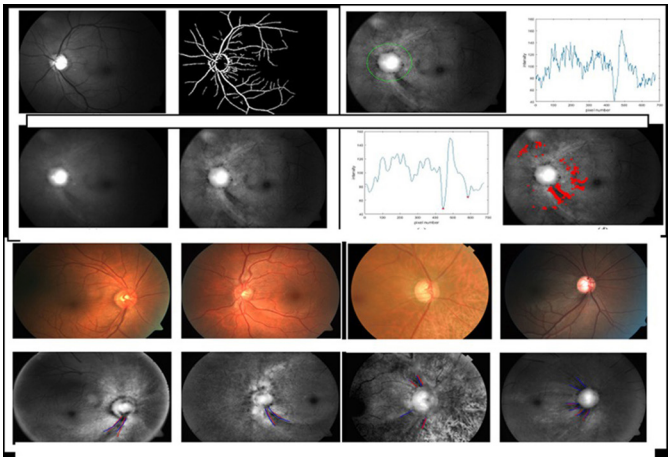

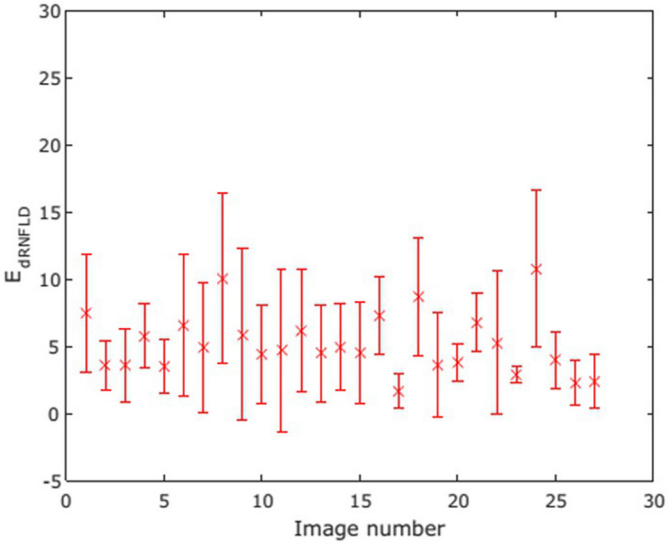

Commercial Relationships: Aparna Rao; **Rashmi Panda**, None; **Niladri Puhan**, None; **Debananda Padhy**, None

Program Number: 688 **Poster Board Number:** B0435
Presentation Time: 3:15 PM–5:00 PM

NEURAL NETWORK FOR DETECTION OF DIABETIC MACULAR EDEMA IN FUNDUS COLOR IMAGES

Francisco J J. Rodriguez[1], Oscar Perdomo[2], Flor E. Gomez[1], Shirley M. Rosenstiehl[1], Hernan A. Rios[1], Fabio Gonzalez[2]. [1]Retina and Vitreous, Fundacion Oftalmologica Nacional, Bogota, Colombia; [2]Faculty of Engineering, Universidad Nacional de Colombia, Bogota, Colombia.

Purpose: Diabetic Macular Edema is one of the main causes of legal blindness in work-age population. The Artificial Neural Networks are useful for early detection of Diabetic Macular Edema, with a great importance in developing countries, where specialized management is limited. The purpuse of the study was to determine the sensitivity and specificity in diagnostic test based on Artificial Neural Networks as a method for automatic detection of clinical features on Diabetic Macular Edema diagnosis

Methods: A cross-sectional diagnostic test study for an Artificial Neural Networks based learning system was performed. Sensitivity

and specificity for Diabetic Macular Edema diagnosis and classification of color fundus photographs were assessed
Results: The Network shown an accuracy rate of 73.5% in detecting Diabetic Macular Edema during the training stage. In the final stage, for Diabetic Macular Edema diagnosis the sensitivity was 61% and specificity 69% (positive predictive value 63% and negative predictive value 67%) when compared with Gold Standard. To classify the grade of Diabetic Macular Edema the Network has a sensitivity of 70% and specificity 61% (with a positive predictive value 64% and negative predictive value 68%)
Conclusions: Artificial Neural Networks show good performance in detection and classification of diabetic macular edema. This study is the first step to build a telemedicine tool to support physicians to detect Diabetic Macular Edema using color fundus photographs
Commercial Relationships: Francisco J J. Rodriguez, None; **Oscar Perdomo**, None; **Flor E. Gomez**, None; **Shirley M. Rosenstiehl**, None; **Hernan A. Rios**, None; **Fabio Gonzalez**, None

Program Number: 689 **Poster Board Number:** B0436
Presentation Time: 3:15 PM–5:00 PM
Image Quality Assessment of Fundus Images Using Deep Convolutional Neural Networks with Extremely Few Parameters
Christian Wojek[1], Keyur Ranipa[2], Abhishek Rawat[2], Thomas Milde[1], Alexander Freytag[1]. [1]Corporate Research, Carl Zeiss AG, Oberkochen, Germany; [2]CARIn, Carl Zeiss India, Bangalore, India.
Purpose: Current state-of-the-art remote screening solutions work by classifying fundus images into healthy/diseased either by human readers or algorithms. It is tacitly assumed that images are recorded in optimal image quality (IQ).This assumption is heavily violated in field-mode in particular for hand-held fundus cameras, causing unreliable clinical findings. Here we describe a deep convolutional neural network (CNN) that predicts the IQ of a fundus image at acquisition time. Thus, non-experts can obtain feedback on their IQ and iterate until IQ allows for reliable clinical findings.
Methods: We trained CNNs for the task of IQ prediction based on 4,262 good & 178 poor quality images taken with VISUSCOUT® 100 (ZEISS, Jena, Germany). The most common error-types caused by non-optimal usage of hand-held fundus cameras are light-leakage, motion blur, overexposure & underexposure. Given the unbalanced sample bins, we additionally simulated poor IQ using good data and randomly adding one of the four sources of error as shown in Fig. 1. For every good image, we simulated two random versions per error type, resulting in another 34,096 images of poor quality. We used 70% randomly chosen images for training,10% for model validation and 20% for testing. We trained both a large and an extremely small CNN with 875,040 and 3,104 parameters respectively for the task of IQ prediction.
Results: Our results are shown in Fig. 2. Both networks clearly learned to solve the task of automated IQ prediction by achieving AUC scores of >99.9%. Not surprisingly, a network trained on very little data (light red line) is not able to reach an acceptable accuracy level. In Fig. 2.b, we additionally show qualitative impressions. All shown images were rated as “good” by experts. The top row contains images with lowest score (i.e., reject) given by our network. As all of these images suffer from strong light leakage, this behavior is understandable. However, the scores are still larger than the majority of poor images.
Conclusions: We present a solution for automated IQ assessment of fundus images taken by a hand-held fundus camera VISUSCOUT 100. Our results surpass 99.8% AUC even with a tiny CNN that directly allows for in-field applications with limited hardware.

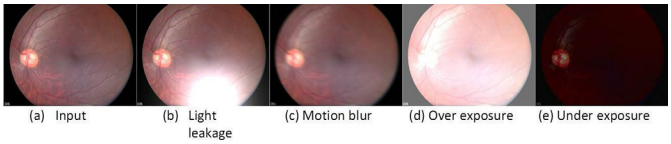

Fig1: A well captured fundus image and four simulated images with failure cases that result in poor IQ

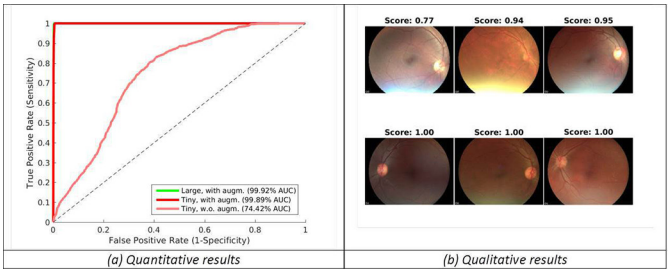

Fig2: Quantitative and qualitative results for automated IQ prediction
Commercial Relationships: Christian Wojek, Carl Zeiss AG (E); **Keyur Ranipa**, Carl Zeiss India (Bangalore) Pvt Ltd (E); **Abhishek Rawat**, Carl Zeiss India (Bangalore) Pvt Ltd (E); **Thomas Milde**, Carl Zeiss AG (E); **Alexander Freytag**, Carl Zeiss AG (E)

Program Number: 690 **Poster Board Number:** B0437
Presentation Time: 3:15 PM–5:00 PM
Fundus images spatial feature analysis for an improved single-pixel camera ophthalmoscope
Benjamin Lochocki[1], Esther Irles[2], Alberto De Castro[1], Adrian Gambin[1], Enrique Tajahuerce[2], Jesus Lancis[2], Pablo Artal[1]. [1]Laboratorio de Optica, Universidad de Murcia, Murcia, Spain; [2]Institute of New Imaging Technologies, Castellon, Spain.
Purpose: In single-pixel camera ophthalmoscope (SPCO) imaging, the reconstructed image resolution depends on the number of illumination patterns. This limits either the resolution or the duration of the image capture. Here, we examined a method to reduce the imaging time by pre-analyzing the spatial features of the retinal fundus, minimizing the impact of eye movements on the final image quality.
Methods: Images of the optical nerve head (ONH) area of six normal subjects were obtained taken with a commercially available retinal camera (EasyScan, iOptics, The Netherlands). Afterward, the images were analyzed and categorized regarding their spatial features. With the obtained information, we were able to select illumination patterns, which presumably give us spatial information to reconstruct an image of the ONH. At the same time, patterns with non-relevant or identical information were rejected and therefore not displayed during the retinal illumination. This method allowed us to limit the amount of patterns, which need to be displayed while maintaining similar final reconstruction image quality. Image quality can be improved when the overall imaging time is kept constant independent of the amount of patterns. The ONH is the preferred area of interest as its high contrast area makes it easy to compare with images taken in the experimental prototype of SPCO.
Results: Initial experimental results obtained using a model eye and a maximum reduction in the number of patterns of 80% confirmed the viability of this approach. Furthermore, images of the ONH in real eyes show good results in terms of image quality albeit a reduction no better than 50% could be achieved. Lowering the amount of patterns and hence decreasing illumination time lowers the severe impact of eye movement without losing significant object information. Final

image quality is similar to previous images reconstructed while displaying all structured patterns.
Conclusions: When using pre-selected spatial patterns, the illumination time for a SPCO could be decreased while obtaining constant image quality. Pre-analyzing spatial features of a retinal area of interest could lead to a generic fundus dictionary, which could benefit future single-pixel imaging and compressive sensing ophthalmic devices.
Commercial Relationships: Benjamin Lochocki; **Esther Irles**, None; **Alberto De Castro**, None; **Adrian Gambin**, Laboratorio de Optica (P); **Enrique Tajahuerce**, Laboratorio de Optica (P); **Jesus Lancis**, Laboratorio de Optica (P); **Pablo Artal**, Laboratorio de Optica (P)
Support: European Research Council Advanced Grant ERC-2013-AdG-339228 (SEECAT), SEIDI, Spain (grants FIS2013-41237-R, FIS2013-40666-P), "Fundación Séneca," Murcia, Spain (grant 19897/GERM/15)

Program Number: 691 **Poster Board Number:** B0438
Presentation Time: 3:15 PM–5:00 PM
Detection of Lesions and Severity Grading for Diabetic Retinopathy in Normalized Fundus Images
Kedir Adal[1, 2], Kenneth W. Rouwen[3], Tunde Peto[4, 5], Peter G. van Etten[3], Jose P. Martinez[3], Lucas J. van Vliet[2], Koenraad A. Vermeer[1].
[1]Rotterdam Ophthalmic Institute, Rotterdam, Netherlands; [2]Imaging Physics, Delft University of Technology, Delft, Netherlands; [3]Rotterdam Eye Hospital, Rotterdam, Netherlands; [4]NIHR Biomedical Research Centre at Moorfields Eye Hospital NHS Foundation Trust and UCL Institute of Ophthalmology, London, United Kingdom; [5]Centre for Public Health, Queen's University Belfast, Belfast, United Kingdom.
Purpose: The visibility of retinal structures on fundus images is a key factor for diabetic retinopathy (DR) screening. This study aims to evaluate if normalization of fundus images for illumination variations improve the detection of DR related lesions by professional fundus image graders (Moorfields Reading Centre).
Methods: Four-field fundus image sets obtained from one eye (randomized) of 150 patients with diabetes mellitus attending the Rotterdam Eye Hospital after 01/May/2014 were included. Each image set was normalized for local variations in illumination, yielding uniform luminance and increased contrast of retinal structures (Adal et. al. WBIR 2014). Each four-field image set was combined into a large mosaic of color, red-free and normalized images for comprehensive retinal examination (Fig. 1).
For each eye, mosaics of Color+Red-free (CR) and Normalized+Color (NC) were shown separately and independently to 5 expert graders for detection of DR lesions and to assign DR level (ICDR severity scale). The number of red DR lesions (microaneurysms and haemorrhages) and severity of DR were analysed for both the CR and the NC mosaics.
Results: Altogether 300 (150 CR/150 NC) mosaics were annotated; Table 1 summarizes the detected red lesions. Graders detected significantly more lesions (on average 122%) on NC mosaics compared to CR (Wilcoxon signed-rank test; p=0.03). In addition, graders were more likely to assign a higher DR severity level to NC mosaics compared to RCs (Table 1; proportional odds mixed model; odds ratio=3.4, p<10^-16); however there was only moderate agreement between the graders (ICC(2,1) =0.51).
Conclusions: Fundus image illumination normalization improves the visibility of retinal features and hence facilitates better detection of red DR lesions. Higher DR severity levels were assigned after normalization. This warrants further research as its validity and clinical consequences must be established before illumination normalization can be used in clinical practice.

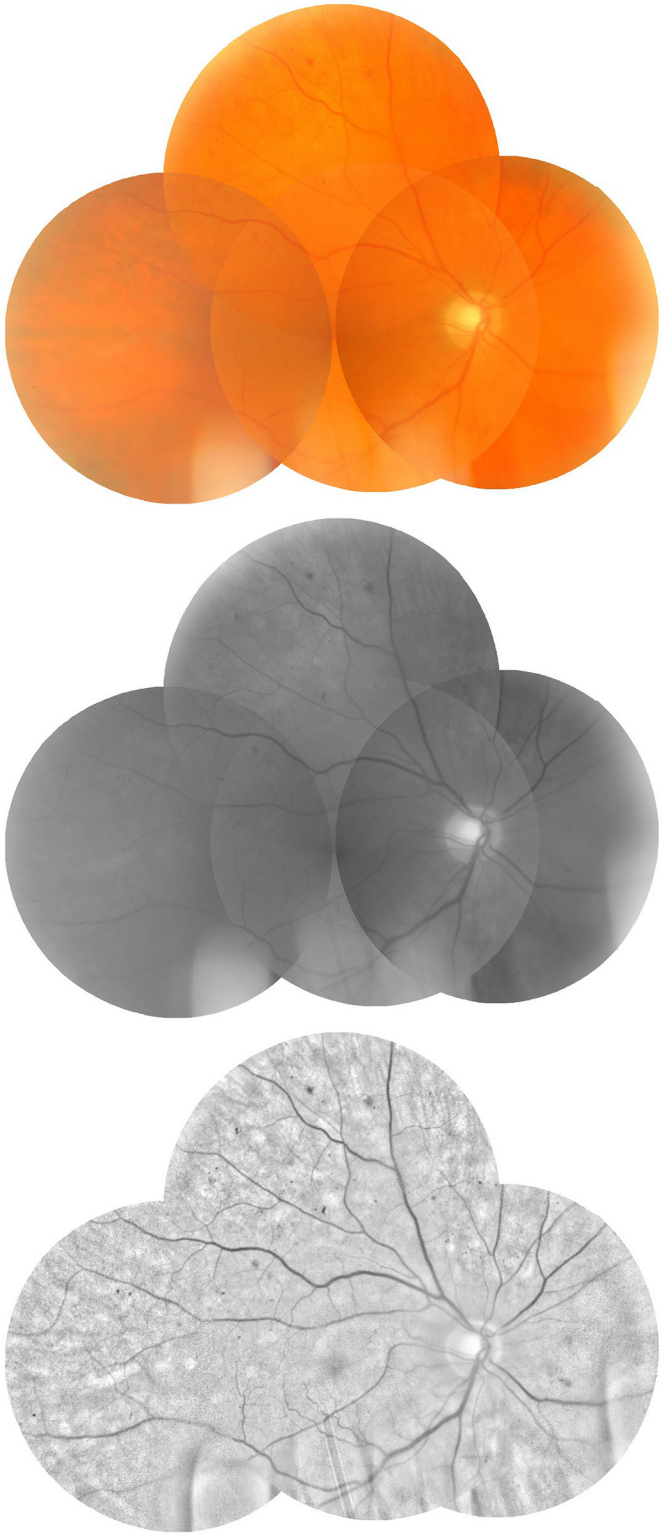

Fig. 1. An example of a color (top), a red-free (middle), and a normalized (bottom) fundus mosaic of a right eye.

	Red DR Lesions Count			DR Level		
	CR	NC	Increase (%)	CR higher	Equal	NC higher
Grader 1	179	275	54%	6	126	18
Grader 2	192	298	55%	9	115	26
Grader 3	76	207	172%	5	112	33
Grader 4	152	555	265%	10	87	53
Grader 5	246	541	120%	11	84	55

Table 1. The number of red lesions detected on each of the mosaics sets and the number of eyes in which using the CR or NC mosaics resulted in a higher DR level.

Commercial Relationships: Kedir Adal, None; **Kenneth W. Rouwen**, None; **Tunde Peto**, None; **Peter G. van Etten**, None; **Jose P. Martinez**, None; **Lucas J. van Vliet**, None; **Koenraad A. Vermeer**, None
Support: CZ Fonds (201400002), Stichting Blindenhulp, and Stichting Wetenschappelijk Onderzoek het Oogziekenhuis